FUNDAMENTALS AND APPLICATIONS OF SOLID STATE AND BIOLOGICAL NANOPORES

by

Rukshan Tharanga Perera

A dissertation submitted to the faculty of
The University of Utah
in partial fulfillment of the requirements for the degree of

Doctor of Philosophy

Department of Chemistry

The University of Utah

May 2016

The University of Utah Graduate School

STATEMENT OF DISSERTATION APPROVAL

The dissertation of **Rukshan Tharanga Perera**

has been approved by the following supervisory committee members:

Henry S. White	, Chair	**11/17/2015** Date Approved
Cynthia Burrows	, Member	**11/17/2015** Date Approved
Shelley D. Minteer	, Member	**11/17/2015** Date Approved
Michael David Morse	, Member	**11/17/2015** Date Approved
Rajesh Menon	, Member	**01/19/2016** Date Approved

and by **Cynthia Burrows**, Chair/Dean of

the Department/College/School of **Chemistry**

and by David B. Kieda, Dean of The Graduate School.

ABSTRACT

Both biological and solid state nanopores have been used to study fundamentals of ion transport phenomena and potential applications in single molecule analysis. This dissertation presents investigations of the effect of the electric double layer in the activation energy of ion transport in conical shaped glass nanopores. Further, it presents the use of the α-hemolysin nanopore to detect the DNA cancer biomarker benzo[a]pyrene, and to detect structural differences between the A- and B- form duplexes. Chapter 1 overviews the solid state and biological nanopores, common transport phenomena observed in sold state nanopores, and detection of ssDNA, dsDNA, and biomarkers using biological nanopores.

Chapter 2 describes the effect of the electric double layer on the activation energy of ion transport through conical shaped glass nanopores. The study shows that the activation energy values for transport within an electrically charged conical glass nanopore differ from the bulk values due to the voltage and temperature-dependent distribution of the ions within the double layer. Finite element simulations based on the Poisson-Nernst-Planck model semiquantitatively predict the measured temperature-dependent conductivity and dependence of activation energy (E_A) on applied voltage. The results highlight the relationships between the distribution of ions with the nanopore, ionic current, and E_A, and their dependence on pore size, temperature, ion concentration, and applied voltage.

Chapter 3 describes how the α-hemolysin (αHL) nanopore platform can be used to detect the benzo[a]pyrene diol epoxide (BPDE) adduct to guanine (G) in synthetic oligo deoxynucleotides. BPDE adducts are formed by exposure to the carcinogenic precursor benzo[a]pyrene (BP), a polycyclic aromatic hydrocarbon, and considered as a biomarker that can initiate cancers. Translocation of a 41-mer poly-2'-deoxycytidine strand with a centrally located BPDE adduct to G through αHL in 1 M KCl produces a unique multi-level current signature allowing the adduct to be detected from either the 5' or 3' directions. This result suggests that BPDE adducts and other large aromatic biomarkers can be detected with αHL, presenting opportunities for the monitoring, quantification, and sequencing of mutagenic compounds from cellular DNA samples.

Chapter 4 describes the unzipping of double-stranded nucleic acids by an electric field applied across the membrane, providing structural information about different duplex forms. Comparative studies on A-form DNA-RNA duplexes and B-form DNA-DNA duplexes with a single-stranded tail identified significant differences in the blockage current and in the unzipping duration between the two helical forms. The effect of varying the length of the single-stranded overhang was investigated, and A-form DNA-PNA duplexes were studied to provide additional support for the proposed model. This result identifies key differences between A- and B-form duplex unzipping that will be important in the design of future probe-based methods for detecting DNA or RNA.

TABLE OF CONTENTS

LIST OF TABLES

Tables

LIST OF FIGURES

Figures

LIST OF ABBREVIATIONS

2D : two-dimensional

αHL: alpha hemolysin

η : dynamic viscosity of the medium

Ag/AgCl : silver/silver chloride

BP : benzo[a]pyrene

BPDE : benzo[a]pyrene diol epoxide

°C : degree Celsius

cm : centimeters

DNA : deoxyribonucleic acid

DPhPC: 1,2-diphytanoyl-*sn*-glycero-3-phosphocholine

E : electric potential

E_A : activation energy

EDL: electric double layer

ELISA : enzyme-linked immunosorbent assay

FEM : finite-element method

GΩ : gigaohm

G-BPDE : guanine- benzo[a]pyrene diol epoxide adduct

GNM : glass nanopore membrane

HPLC: high performance liquid chromatography

i : current

ICR : ion current rectification

I-E: current versus electric potential

i_{lim} :limiting current

I_o :open pore current

i-t : current-time

K^+ : potassium ions

KCl : potassium chloride

kHz :kilohertz

kJ : kilo Joul

LC-MS : liquid chromatography coupled to mass spectrometry

ln : natural logarithm

M : moles per liter

MΩ : megaohm

mC : millicoulomb

mL : milliliter

mmHg : millimeter mercury

ms : millisecond

mV : millivolt

nA : nanoampere

NDR : negative differential resistance

nM : nanomolar

nt : nucleotide

PAH : polycyclic aromatic hydrocarbons

PNA : peptide nucleic acid

Pt : platinum

pA : picoampere

pm : picometer

RNA : ribonucleic acid

THF : tetrahydrofuran

Tm : melting temperature

V : voltage

ACKNOWLEDGEMENTS

I would like to express my gratitude to my advisor Dr. Henry White for his guidance during my PhD study at University of Utah. Frequent advice based on his extensive experience in research has helped me in designing, implementing, and finishing a research project in an effective manner. I would also like to extend my gratitude towards my committee and especially Dr. Cynthia Burrows for helpful suggestions and guidance throughout my study.

I would also thank Dr. Aaron Fleming, Dr. Robert Johnson and Dr. Martin Edwards for their useful contributions to my research work. I thank my past and present group members; Dr. John Watkins, Dr. Deric Holden, Dr. Qian Jin, Dr. Long Luo, Dr. Qianjin Chen, Dr. Kim McKelvey, Mr. Jewen Xiong, Ms. Cherry Tan, Mr. Sean German, Mr. Alan Zhang for being helpful and making a great working environment in the lab. I also must thank our collaborators, Dr. Na An, Dr. Yun Ding, Dr. Ania Wolna, Dr. Jan Riedl, and Mr. Lidong for useful discussions. Special thanks goes to Dr. Steven Feldberg for useful discussions during his visits to our lab.

Finally yet importantly, I would also like to sincerely thank my father, mother, and my family members for their immense love, support, and encouragement.

CHAPTER 1

INTRODUCTION

Miniaturizing the dimensions of a sensor comparable to the size of individual molecules is a key feature of single-molecule sensing.[1-3] This fundamental principle has led to the development of a new class of label-free sensors termed "nanopores". Nanopores have been investigated extensively for biosensing applications that play a significant role in medicine, analytical biochemistry, and biotechnology.[4-6] Incorporation of fabrication and designing technologies from the semiconductor industry has helped to develop miniaturized sensing devices that allow the production of highly portable, low footprint, scalable devices.[7]

Nanopores may be confined to the nanoscale in depth, width, or both.[8] Nanopores can be identified as either biological nanopores, extracted from bacteria, or solid-state, fabricated in thin membranes using modern nanotechnology.[5,9] In each case, chambers on both sides of the pore are filled with an electrolyte and a voltage is applied across the nanopore to measure the conductance. When a charged analyte that is comparable to the size of the pore is introduced into one of the chambers, the electrophoretic force will drive it through the pore, giving rise to a brief change in conductance as the analyte passes through the pore. The change in conductance can provide useful information about the analyte, such as its size and charge. The origin of this idea dates back to the 1950s, when

a similar method was used develop the Coulter counter technology that is today used to count red blood cells.[10,11] The main advantage of this method is the label free detection of the analyte. Resistive pulse techniques have been used to detect virus particles in the 1970s, but any detection of single macromolecules such as DNA, RNA, or protein remained unexplored until the 1990s.[12,13]

Apart from sensing applications, nanopores have also received considerable attention due to the unique mass transport phenomena that arise because of their high surface to volume ratios and surface charge. Ion-current rectification,[14-16] ion concentration polarization,[17] and negative differential resistance [18] are some of the unique phenomena that can influence transport in nanopores and in nanofluidic structures. Understanding the unique properties at the nanoscale is important in developing nanopore sensors and micro- and nano-fluidic devices.

Surprisingly, few studies have focused on the temperature dependence of the ion transport at confined geometries. We used the activation energy of ion transport (E_A) as a parameter to study the effect of temperature on ion transport in conical-shape glass nanopores. The E_A, measured as a function of pore size, electrolyte concentration, and applied voltage are presented in Chapter 2.

Additionally, Chapter 3 and 4 present practical applications where α-hemolysin protein nanopores were used to detect a DNA cancer biomarker and the structural differences between different types of nucleic acid duplexes.

1.1 Glass Nanopores to the Study Activation Energy of Ion Transport

The robustness and durability of solid-state pores compared to their biological counterparts, offer fine-tuning of the size and shape at subnanometer precision,[19] permitting detailed studies of fundamental ion transport in well-defined nanopore geometries. Silicon nitride, silicon oxide, and metal oxides are the most widely used materials to fabricate nanopores using ion beam sculpting, atomic layer deposition, and e-beam drilling techniques.[20-22] Our lab has developed a simple bench-top method to fabricate conical shape nanopores embedded in a thin glass membrane (Figure 1.1), referred to herein as glass nanopore membrane (GNM).[23] The method does not require any sophisticated micro/nano fabrication techniques and also allows modification of the surface (via well-characterized silane chemistries) to introduce hydrophobicity or change the surface charge.[24] Nanoscale conical-shaped glass nanopores prepared in our laboratory have been used to study ion transport phenomena and in particle translocation experiments. The fabrication of GNMs is reported elsewhere but briefly summarized here.[23]

As the first step, a 25 μm Pt wire is sharpened electrochemically and sealed into a glass capillary. Borosilicate or soda-lime glass is mainly used for this purpose. The sealed glass is then polished away until the tip of the Pt wire is exposed. In the last step, the sealed Pt is electrochemically etched out resulting in a conical-shaped nanopore embedded in the glass membrane. The radius of the pore mouth can be measured by the conductance across the nanopore when the electrolyte concentration, temperature, and the half cone angle of the nanopore are known. This simple but very effective method has been used to fabricate GNMs to investigate ion transport properties presented in Chapter 2. GNMs used as a platform to support lipid bilayers are presented in Chapter 3 and 4.

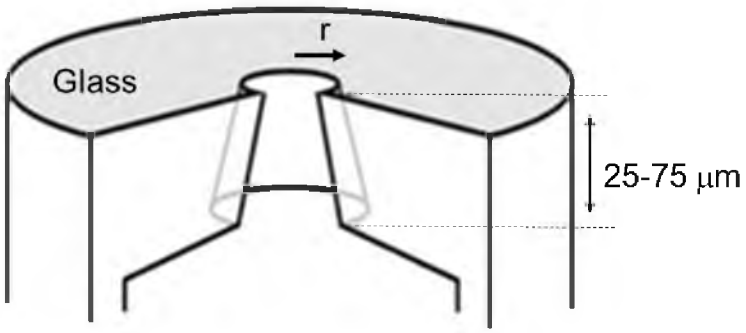

Figure 1.1. Schematic diagram of the conical shaped nanopore formed in a glass membrane. Values for r are typically between 10-1000 nm. Not drawn to the scale.

1.1.1 The Electric Double Layer

Many of the intriguing mass transport properties of glass nanopores arise from their charged surfaces at near-neutral pH. Glass surfaces can acquire surface charge due to ionized surface groups or adsorbed ions when brought into contact with an aqueous phase. At neutral pH, glass acquires negative charge due to the SiO^- groups. The charged surface influences the distribution of the ions and dipolar constituents in close proximity, which results in a net change in the positions of the ions to minimize their total free energy. As a result of the electrostatic interactions, ions of opposite charge to the surface charge (counter ions) will be attracted to the surface while ions of the same charge (co-ions) are repelled.[25] The electrostatic interactions create a thin layer of counter ions at the charged surface. The charged layer that forms at the charged surface and electrolyte interface is termed the "electric double layer" (EDL).[26,27] Helmholtz was the first to propose the idea of EDL in 1879. His model provided a good foundation to describe the ion distribution at the interface; however, it does not account for important factors including diffusion/mixing of ions in solution, adsorption, and the possibility of interaction between solvent dipole

moments and the charged surface. Later, Gouy[28] (1910) and Chapman[29] (1913) developed a model to introduce the "diffuse layer" where counter ions in the electrolyte are not rigidly held at the interface but mobile due to the influence of diffusion and electrostatic forces. In this model, the ions are considered as point charges. The electric potential exponentially decreases away from the charged surfaces and obeys the Poison-Boltzmann distribution as shown in Figure 1.2.[25,27]

$$\frac{\partial^2 \psi}{\partial x^2} = \left(\frac{F z_i c_o e^{\frac{-ze\psi}{kT}}}{\varepsilon \varepsilon_o} \right) \tag{1.1}$$

where c_o is the bulk concentration of ions, ψ is the electrostatic potential at point x, and z is the valency of the ions. F is the faraday constant and k is the Boltzmann constant. ε and ε_o represents the permittivity of the solvent and permittivity of vacuum, respectively.

The composition of the counter ions at the charged surface is significantly different from the bulk solution and the net charge built up at the surface generates an electrical potential difference at any two points between the surface and bulk solution. The Debye length (κ^{-1}) is the parameter used to characterize the thickness of the EDL. The Debye length is a function of electrolyte concentration and the temperature,

$$\kappa^{-1} = \left(\frac{\varepsilon_r \varepsilon_o RT}{2z^2 F^2 c} \right) \tag{1.2}$$

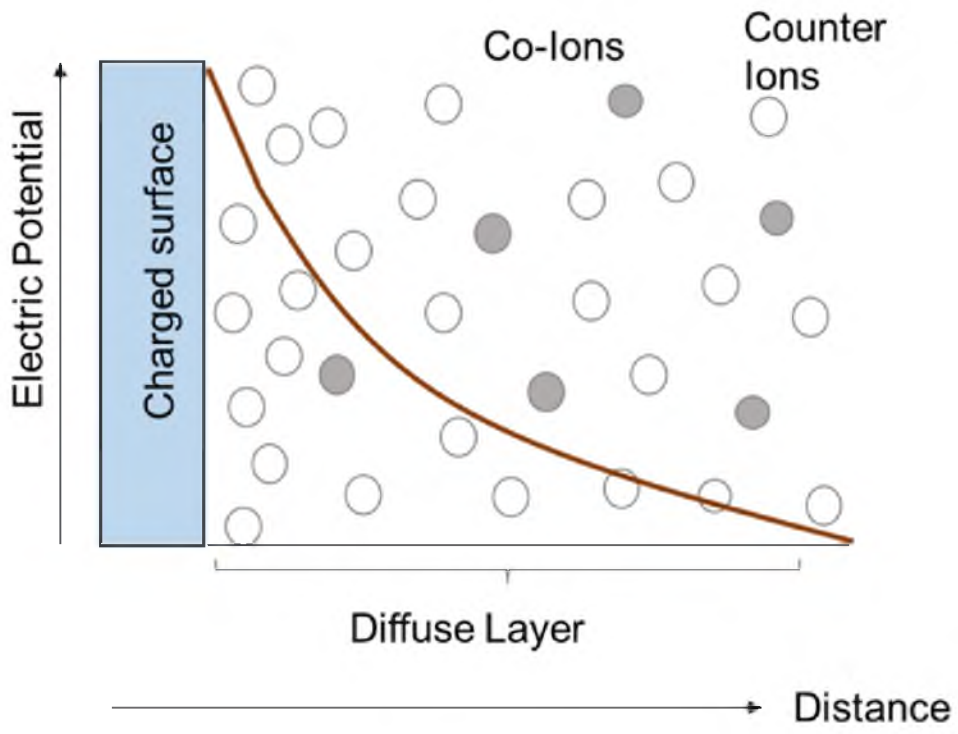

Figure 1.2. A schematic diagram of the electric double layer at the charged surface/ electrolyte interface, as proposed by Gouy-Chapman model. The brown solid line shows exponential decay of potential across the solution.

where ε_r is the relative permittivity, ε_o is the permittivity in a vacuum, R is the gas constant, T is the absolute temperature, z is the electrolyte valence, F is Faraday's constant, and c is the electrolyte concentration. For a 1:1 electrolyte at 25 ºC, the above simplifies to:

$$\kappa^{-1}(\text{nm}) = \left(\frac{0.304}{\sqrt{c}}\right) \tag{1.3}$$

where c is in units of mol dm^{-3}. For a 1:1 electrolyte at 25 ºC, the Debye length in 0.01 mM solution is approximately 100 nm and at 100 mM it is approximately 1 nm.

The existence of the EDL structure alters the fluid flow at charged surfaces. When two or more surfaces are close to each other, that is, separated by a distance comparable to the Debye length, an overlapped EDL can be expected (Figure 1.3).[30] The distance between the two charged surfaces facing each other and the Debye length can determine the degree of the overlap. The electro-neutrality of the system is also strongly effected due to counter ion enrichment between the surfaces and creates a nonuniform potential distribution. The difference in ion distribution at the pore mouth can result in different transport phenomena at the nanoscale compared to the bulk solution.

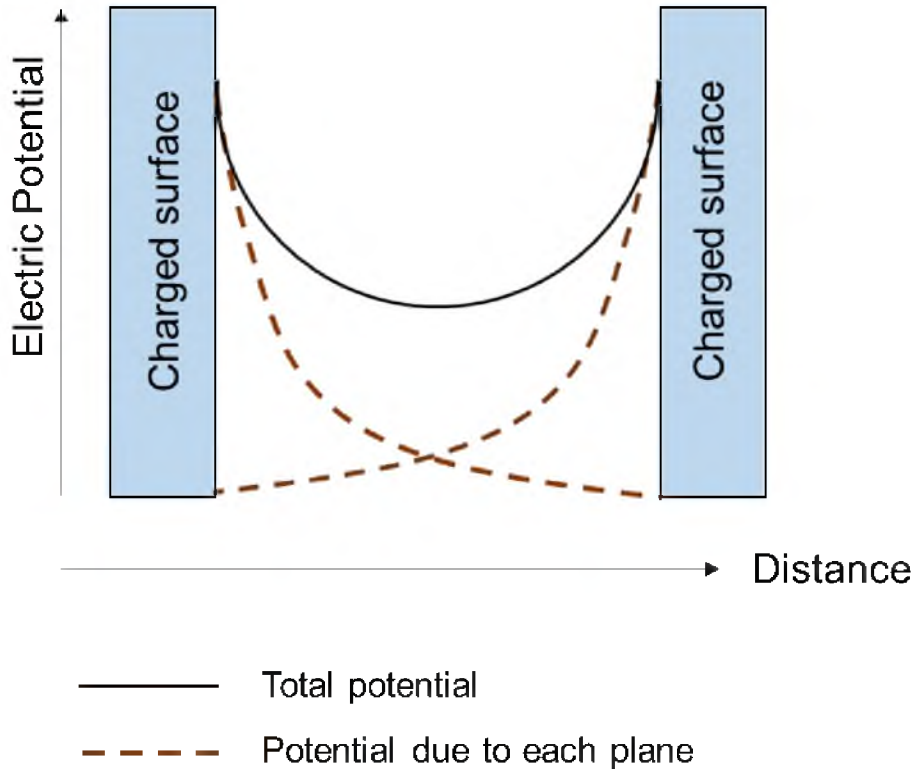

Figure 1.3. A schematic diagram of the overlapped electric double layer. The brown dashed lines show the electric potential due to each plane and the solid black line represents the overall potential between the two charged surfaces.

1.1.2 Ion Current Rectification

The formation of overlapping double layers in nanopores, as a consequence of charged surfaces separated by distances comparable to the Debye length, gives rise to unique ion transport phenomenon not observed in macroscopic pores. One such unique transport phenomena shown by nanopores is ion current rectification (ICR).[14-16] When the nanopore has an asymmetric charge distribution, the *i-V* curve shows a diode like behavior and does not obey Ohm's law (Figure 1.4). Wei et al. first reported ICR in 1997,[15] demonstrating that ICR is strongly dependent on the pore size and the electrolyte concentration. Since then many reports on ICR have been published, demonstrating the uses of ICR for sensing applications.[31-36]

ICR can be rationalized using the ion accumulation and depletion model.[16,37] The surface of the glass is negatively charged at neutral pH due to dissociation of protons from the silanol groups. The negatively charged walls will be screened by positive ions and form an EDL as described in the previous section. The length of the EDL is roughly $5\kappa^{-1}$ where κ^{-1} is the Debye length. At low electrolyte concentrations, the Debye length expands and the pore orifice is predominantly occupied by the counter ions (K^+). When a positive voltage is applied to the electrode inside the nanopore (the outside electrode is grounded), K^+ ions move outside and Cl^- ions move inside the pore. However, due to accumulation of K^+ ions at the pore orifice, Cl^- ions get rejected moving in to the pore resulting in an ion depletion zone inside the pore. This ion depletion inside the pore gives rise to a lower current than expected from linear Ohmic behavior. On the other hand, when a negative voltage is applied to the electrode inside the nanopore, Cl^- will be rejected moving outside, creating an ion accumulation zone inside the pore. Therefore, at negative applied potentials

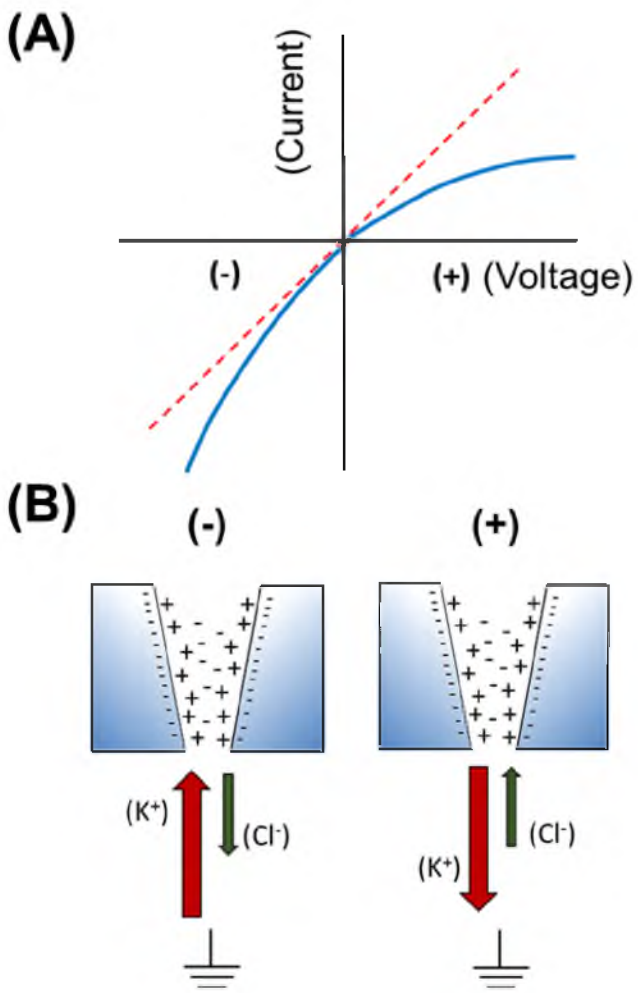

Figure 1.4. A schematic diagram representing the ion current rectification in negatively charged glass nanopores. (A) Diode like *i-V* behavior observed in pores that show ICR. (B) K^+ and Cl^- moving across the pore at different applied voltage.

the current observed is higher compared to the linear Ohmic behavior. In this thesis, Chapter 2 presents a study of ion transport at the nanoscale under ion current rectification conditions. Furthermore, our studies show the nanopore becomes less rectifying at higher temperatures, which intuitively agrees with the idea that at higher temperatures the thermal energy of ions can overcome the electrostatic barriers generated by the nanopore walls to a greater extent.

1.2 α– Hemolysin Nanopore to Detect DNA Cancer Biomarkers and Structural Differences between A- and B-form Duplexes

Protein-based biological nanopores harness the reproducibility of biological systems to furnish well-defined channels, some of which have high-resolution crystal structures to provide a better understanding of their properties.[9] Furthermore, biological nanopores can be modified to induce structural changes using site-directed mutagenesis. Examples of protein nanopores include alpha-hemolysin (αHL),[9,38] MspA,[39] aerolysin,[39,40] and ClyA.[41]

The most studied protein nanopore is the αHL, a toxin secreted as a 33.2-kD water-soluble monomer by *Staphylococcus aureus* (Figure 1.5).[9] This protein can self-assemble into a heptamer and spontaneously inserts into a lipid bilayer, producing a *trans* membrane channel. Due to the size and the comparatively higher stability of the αHL nanopore, it has been heavily explored as a biosensor platform for DNA, RNA, proteins, and small molecules.[13,42-48] To study these molecules, a voltage is applied across the protein, which itself is supported in a lipid bilayer, to electrophoretically drive analytes into the nanopore. Interactions between the channel and molecule of interest yield characteristic deflections in the current and residence times. The size-limiting property of this channel is the central constriction (d = 1.4 nm), which allows single-stranded DNA (d = 1.0 nm) to pass through the β-barrel but not double-stranded DNA (d = 2.0 nm).[49] This unique structure of αHL has been capitalized upon as a next-generation DNA sequencing platform.[8] The idea of using αHL nanopore for DNA sequencing was first proposed by Deamer et al. with the ultimate aim of obtaining different conductance levels for different bases as each base moves through the tightest constriction of the nanopore. [50]

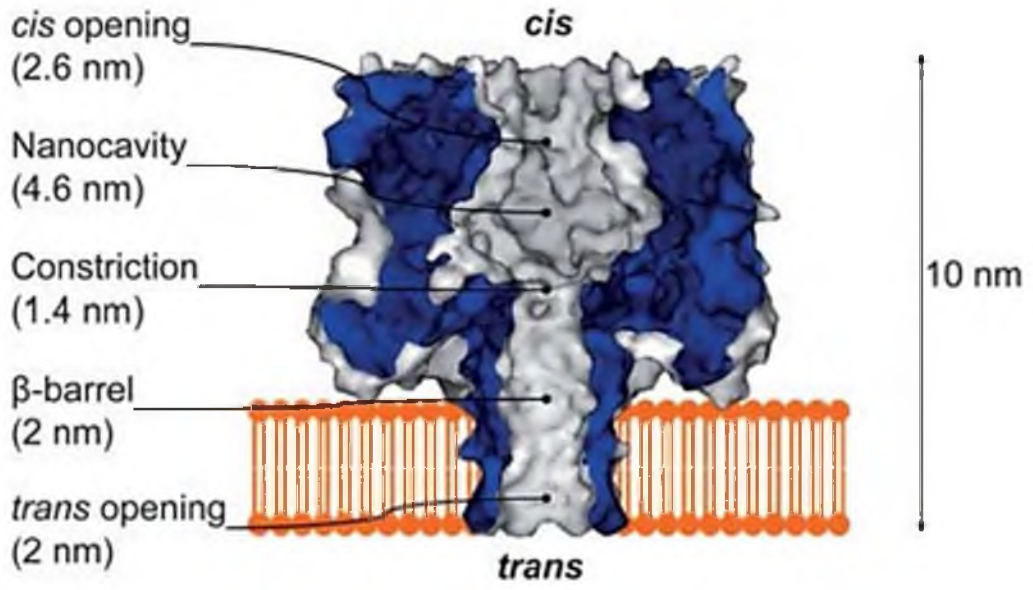

Figure 1.5. The structure of the heptameric αHL pore with the dimensions in the lumen. This figure is reprinted with the permission of reference 37. Gu, L.Q.; Shim, J. W. *Analyst* **2010**, *135*, 441

The first demonstration of DNA translocation through αHL was published in 1996 by Kasianowicz and co-workers.[13] The potential to sequence DNA with nanopores was well-recognized and many research groups are contributing to the development of methods towards the ultimate goal of sequencing DNA.

Further, the αHL channel also provides an excellent system for monitoring reactions and conducting biophysical experiments to interrogate solutes in solution. Chapters 3 and 4 present studies that have been performed using αHL. Chapter 3 focuses on detecting a biologically relevant cancer biomarker using simple translocation experiments whereas Chapter 4 presents the use of unzipping experiments to distinguish between structural differences among A and B forms of duplexes.

1.2.1. Nanopore Ion Channel Recordings and Single Strand Translocation

As a solid support to form the lipid bilayer, we used the GNM discussed in section 1.1. GNMs used in these experiments have significant advantages over SiN and Teflon solid supports that are commonly in use. The diameter of the GNMs we use here are at least one to two orders of magnitude smaller, and this results in more stable bilayers. The bilayers formed on GNMs are more resistive to environmental disturbances. Our studies have shown the bilayer can be stable for more than a week.[51] Most importantly, the smaller surface area of the GNM can result in lower noise due to reduced charging effects on the bilayer and less capacitance across the solid support. The silanol groups on glass allow surface modification and introducing more hydrophobic functionality to the surface can enhance the bilayer stability.[24,51,52]

After the lipid bilayer is formed on the GNM, monomeric αHL is added to one side of the electrolyte reservoir. Monomeric αHL forms a stable heptametrical ion channel that immediately inserts in to the bilayer, forming a transmembrane ion channel. To study the desired analyte, for example, DNA, a voltage is applied across the protein to guide the analyte toward the nanopore by the electric field. The change in conductance is measured as a function of time as the DNA passes through the protein nanopore. This allows information to be obtained related to the structure of the DNA (Figure 1.6).

The key information that can be extracted from a statistical analysis of a single strand DNA translocation experiment includes translocation time (t), current blockage (I), or residual current (I/I_o, where I_o is the open channel current), and event frequency (f). Both translocation time and current blockage amplitude histograms exhibit Gaussian-like distributions; the peak value of the histograms are reported as the mean translocation time

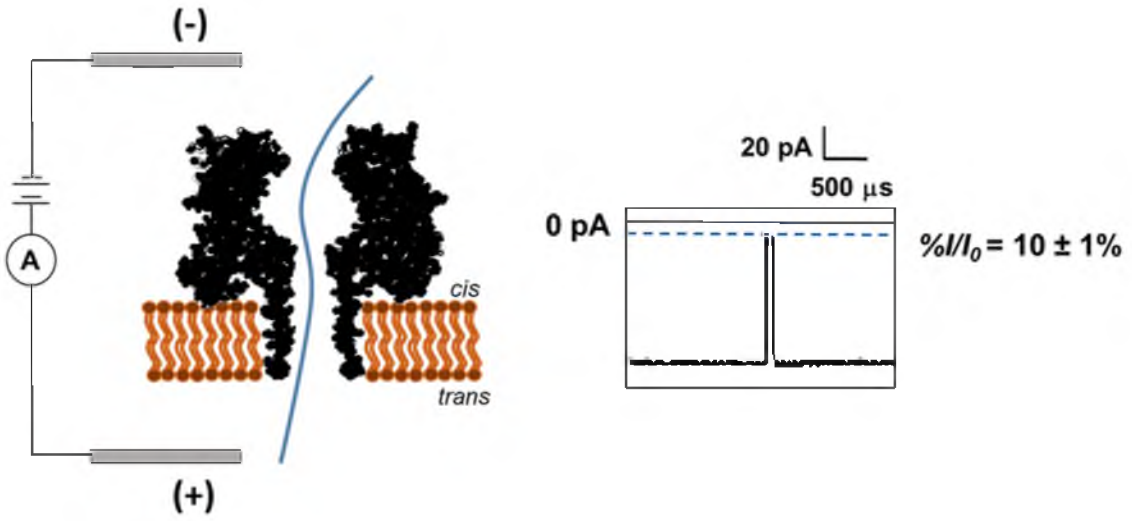

Figure 1.6. A schematic diagram showing single strand DNA translocation through αHL nanopore under the applied voltage (right). A typical *i-t* trace observed for single strand DNA translocation (left)

and the mean current blockage, respectively.[13,46]

After the first demonstration of DNA and RNA oligomer translocation was reported by Kasianowicz and coworkers in 1996, extensive studies have been performed on DNA and RNA translocation.[53-55] In more recent work, the White and Burrows laboratories have demonstrated the use of translocation experiments to detect bulkier adducts.[56,57] Interestingly, single-stranded DNA modified with one or two crown ether adducts showed distinct current blockage (Figure 1.7 (A) and (B)). These studies have concluded the nanopore can detect a single abasic site or two abasic sites per strand as the lesion-containing strand translocates through the pore.

Inspired by the idea that bulky adducts can modulate the current, we have found that the introduction of the bulkier benzo[a]pyrene diol epoxide (BPDE) adduct can perturb translocation and give rise to unique current signals. Binding of BPDE to G residues in the *TP53* gene can cause lung cancer and is therefore considered as a biomarker.[49,58-60]

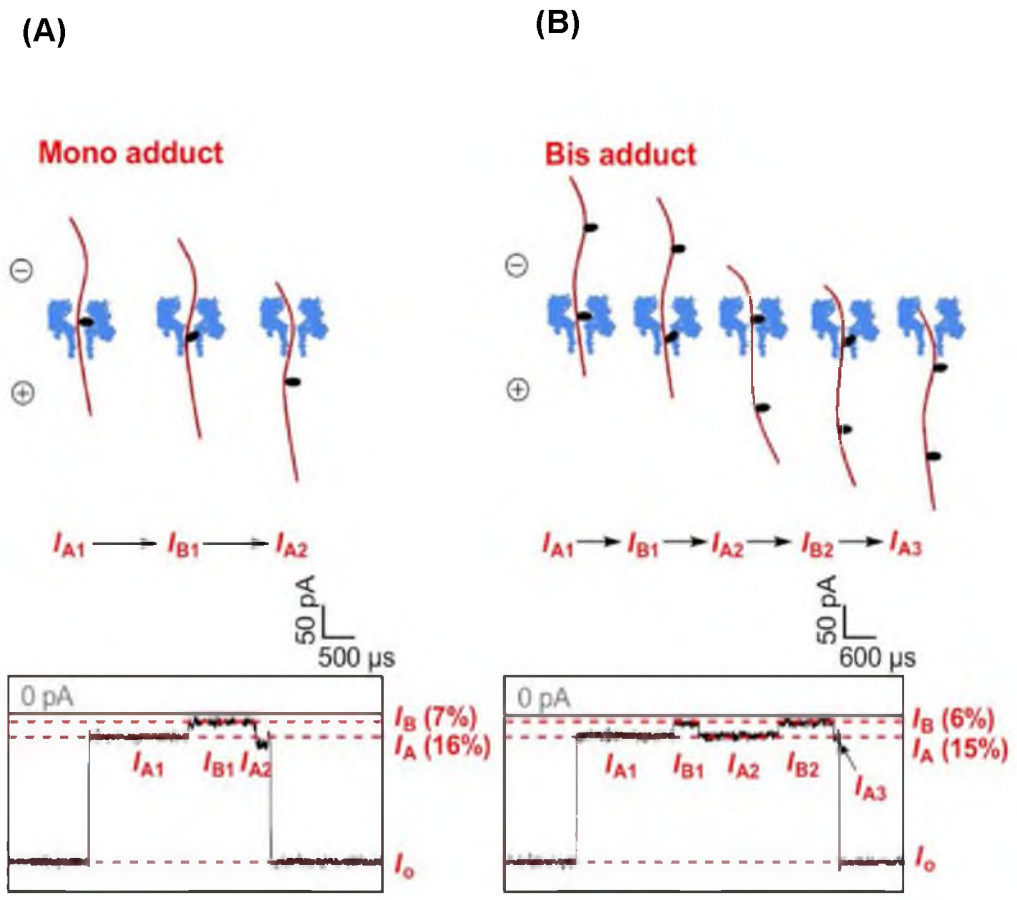

Figure 1.7. Current defection observed during the DNA-crown ether adducts translocation. Sample *i-t* traces of 5′ entry for (A) mono and (B) bis adducts (120 mV *trans* versus *cis*). reprinted with permission from reference 51, An, N.; Fleming, A. M.; White, H. S.; Burrows, C. J. *Proc. Natl. Acad. Sci. U.S.A.* **2012**, *109*, 11504.

The identification of adducts and their locations in the genome are highly important to locate hot spots for mutations. These results are presented in Chapter 3.

1.2.2. Duplex Unzipping

The size-limiting properties of αHL at the central constriction (d = 1.4 nm) only permit single-stranded DNA (d = 1.0 nm) to pass through the β-barrel but not double-stranded DNA. While a duplex cannot translocate through αHL, it can unzip within the vestibule into two strands at moderate applied voltages (Figure 1.8 (A)). Both experimental and molecular dynamics simulation studies have suggested that the majority of the voltage drop occurs at the β-barrel.[47,61]

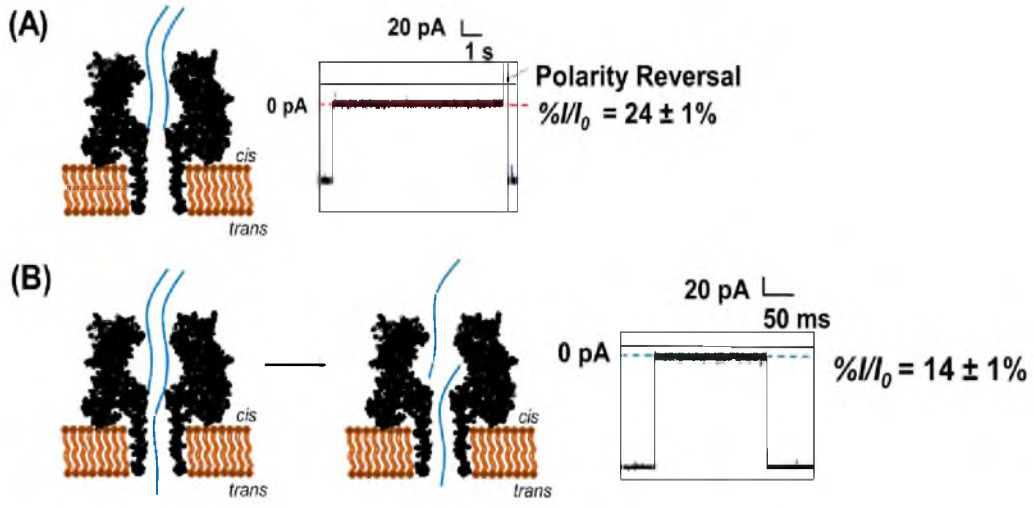

Figure 1.8. Duplex unzipping inside the αHL vestibule. (A) A duplex without an overhang entering the vestibule. The double strand does not unzip, and the molecule is removed by switching the potential. (B) A duplex with an overhang entering the vestibule and eventually unzipping under the applied electric field. The deep blockage current returns to the open channel current suggesting unzipping and translocation of the longer strand. Further, long strands of DNA were collected and identified via PCR on the *trans* side, proving that the longer strand actually translocates through the pore after unzipping. This study also reveals that duplexes that have a mismatch have different unzipping times, hence showing different unzipping kinetics.

Therefore, an overhang attached to one of the strands can occupy the total cross section of the αHL, and the electric field inside the β- barrel can pull the strands that can result in unzipping of the two strands.

Typically, a homo-polymeric overhang greater than 20 nucleotides is required to induce unzipping of the double-stranded DNA.[62] Unzipping eventually permits the longer strand to pass through the β-barrel, giving rise to a current blockage. The unzipping time is at least an order of magnitude higher compared to simple translocation due to the longer residence time inside the vestibule.

Branton and coworkers demonstrated the first example of duplex unzipping.[63] In their study, they captured a duplex with an overhang inside αHL and subjected it to unzipping by applying an electric field. Statistical analysis of the unzipping times shows first order kinetics, which suggests the unzipping is an energy dependent process.

Other duplex unzipping studies have been performed to understand unzipping kinetics,[64] probe base pairing energy,[65] and to detect microRNAs[66] and oxidative damage.[67] Recent unzipping studies performed in the White and Burrows laboratories revealed a new sensing zone of the αHL.[68-71] A missing base or a lesion placed in the duplex that sits close to the sensing zone of the nanopore can produce different unzipping currents and durations (Figure 1.9). The discovery has led to the detection of damage in DNA and base-flipping kinetics using duplex unzipping inside αHL. Studies were extended to detect damage in RNA by utilizing the latch-sensing zone, and the unzipping behavior of DNA-RNA duplexes were carefully studied. In this dissertation, Chapter 4 presents unzipping studies of DNA-DNA, DNA-RNA, and DNA-PNA to demonstrate the use of αHL to distinguish between different forms of duplexes (A-and B-forms). In these studies, we built a physical

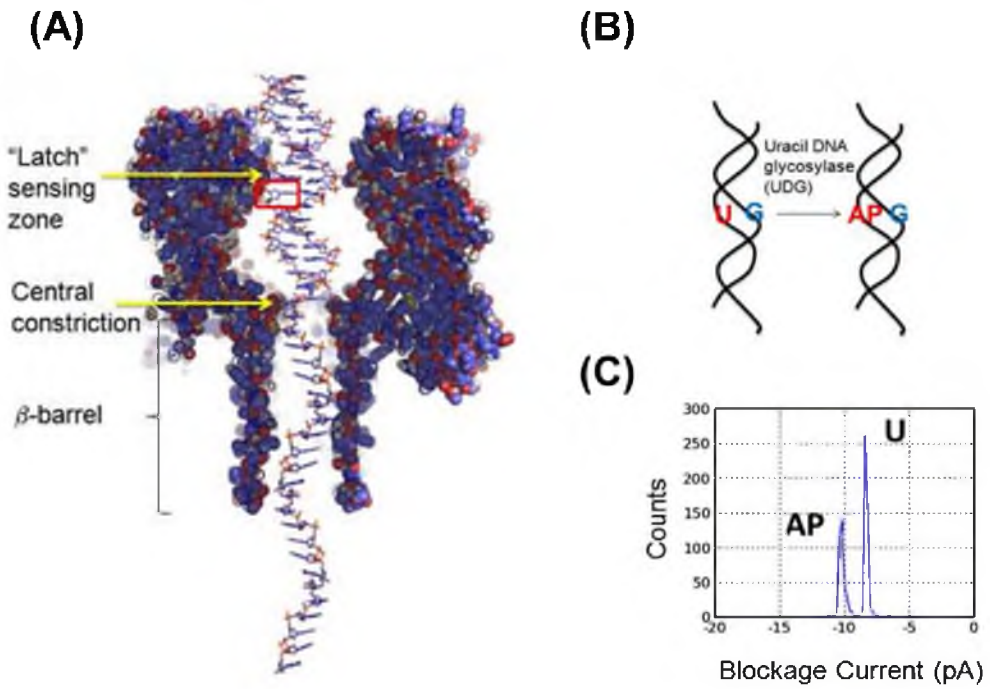

Figure 1.9. Monitoring the uracil DNA glycosylase (UDG) enzyme activity for dsDNA using an αHL channel. (A) The structure of dsDNA with a 5'-polydT24 tail within α-HL. The red box indicates the location of the uracil (U) base or the abasic site (AP). (B) A Scheme of the UDG hydrolysis reaction. (C) The blockage current difference observed for uracil (U) and abasic site (AP).

model for the interaction of the DNA duplexes with the nanopore, which were tested by changing the length of the ssDNA overhang. This work provides useful insight on the interaction between dsDNA/DNA-RNA/DNA-PNA molecules and the αHL nanopore and is important in designing probes.

1.3. References

(1) Wanunu, M.; Dadosh, T.; Ray, V.; Jin, J.; McReynolds, L.; Drndic, M. *Nat. Nanotechnol.* **2010**, *5*, 807.

(2) Miles, B. N.; Ivanov, A. P.; Wilson, K. A.; Dogan, F.; Japrung, D.; Edel, J. B. *Chem. Soc. Rev.* **2013**, *42*, 15.

(3) Venkatesan, B. M.; Bashir, R. *Nat. Nano.* **2011**, *6*, 615.

(4) Vercoutere, W.; Winters-Hilt, S.; Olsen, H.; Deamer, D.; Haussler, D.; Akeson, M. *Nat. Biotechnol.* **2001**, *19*, 248.

(5) Li, J.; Stein, D.; McMullan, C.; Branton, D.; Aziz, M. J.; Golovchenko, J. A. *Nature* **2001**, *412*, 166.

(6) Han, J.; Craighead, H. G. *Science* **2000**, *288*, 1026.

(7) Firnkes, M.; Pedone, D.; Knezevic, J.; Doblinger, M.; Rant, U. *Nano Lett.* **2010**, *10*, 2162.

(8) Wanunu, M. *Phys. Life. Rev.* **2012**, *9*, 125.

(9) Song, L.; Hobaugh, M. R.; Shustak, C.; Cheley, S.; Bayley, H.; Gouaux, J. E. *Science* **1996**, *274*, 1859.

(10) Coulter, W. H. Means for Counting Particles Suspended in a Fluid. U.S. Patent 2,656,508, 1953.

(11) Cornell, B. A.; Braach-Maksvytis, V. L. B.; King, L. G.; Osman, P. D. J.; Raguse, B.; Wieczorek, L.; Pace, R. J. *Nature* **1997**, *387*, 580.

(12) Poutrel, B.; Lerondelle, C. *J. Dairy Sci.* **1983**, *66*, 2575.

(13) Kasianowicz, J. J.; Brandin, E.; Branton, D.; Deamer, D. W. *Proc. Natl. Acad. Sci. U. S. A.* **1996**, *93*, 13770.

(14) Siwy, Z. S. *Adv. Funct. Mater.* **2006**, *16*, 735.

(15) Wei, C.; Bard, A. J.; Feldberg, S. W. *Anal. Chem.* **1997**, *69*, 4627.

(16) White, H. S.; Bund, A. *Langmuir* **2008**, *24*, 2212.

(17) Gong, M. M.; Nosrati, R.; San Gabriel, M. C.; Zini, A.; Sinton, D. *J. Am. Chem. Soc.* **2015**, 137, 13913.

(18) Luo, L.; Holden, D. A.; White, H. S. *ACS Nano* **2014**, *8*, 3023.

(19) Dekker, C. *Nat. Nanotechnol.* **2007**, *2*, 209.

(20) Siwy, Z.; Fulinski, A. *Phys. Rev. Lett.* **2002**, *89*, 198103.

(21) Storm, A. J.; Chen, J. H.; Ling, X. S.; Zandbergen, H. W.; Dekker, C. *Nat. Mater.* **2003**, *2*, 537.

(22) Chen, P.; Mitsui, T.; Farmer, D. B.; Golovchenko, J.; Gordon, R. G.; Branton, D. *Nano Lett.* **2004**, *4*, 1333.

(23) Zhang, B.; Galusha, J.; Shiozawa, P. G.; Wang, G.; Bergren, A. J.; Jones, R. M.; White, R. J.; Ervin, E. N.; Cauley, C. C.; White, H. S. *Anal. Chem.* **2007**, *79*, 4778.

(24) White, R. J.; Ervin, E. N.; Yang, T.; Chen, X.; Daniel, S.; Cremer, P. S.; White, H. S. *J. Am. Chem. Soc.* **2007**, *129*, 11766.

(25) Israelachvili, J. I, *Intermolecular and Surface Forces*, 2nd ed.; Academic Press: London, 2003.

(26) Helmholtz, H. *Ann. Phys.* **1879**, *243*, 337.

(27) Bard, A. J.; Faulkner, L. R. *Electrochemical Methods*; John Wiley and Sons: New York, 1980.

(28) Gouy, M. *J Phys. Theor. Appl.* **1910**, *9*, 457.

(29) Chapman, D. L. *Philos. Mag.* **1913**, *25*, 475.

(30) Baldessari, F.; Santiago, J. G. *J. Colloid Interface Sci.* **2008**, *325*, 526.

(31) Cheng, L. J.; Guo, L. J. *Chem. Soc. Rev.* **2010**, *39*, 923.

(32) Vilozny, B.; Wollenberg, A. L.; Actis, P.; Hwang, D.; Singaram, B.; Pourmand, N. *Nanoscale* **2013**, *5*, 9214.

(33) He, H.; Xu, X.; Jin, Y. *Anal. Chem.* **2014**, *86*, 4815.

(34) Deng, X. L.; Takami, T.; Son, J. W.; Kang, E. J.; Kawai, T.; Park, B. H. *Sci. Rep.* **2014**, *4*, 4005.

(35) Actis, P.; Vilozny, B.; Seger, R. A.; Li, X.; Jejelowo, O.; Rinaudo, M.; Pourmand, N. *Langmuir* **2011**, *27*, 6528.

(36) Umehara, S.; Pourmand, N.; Webb, C. D.; Davis, R. W.; Yasuda, K.; Karhanek, M. *Nano Lett.* **2006**, *6*, 2486.

(37) Kubeil, C.; Bund, A. *J. Phys. Chem. C* **2011**, *115*, 7866.

(38) Gu, L.-Q.; Shim, J. W. *Analyst* **2010**, *135*, 441.

(39) Manrao, E. A.; Derrington, I. M.; Laszlo, A. H.; Langford, K. W.; Hopper, M. K.; Gillgren, N.; Pavlenok, M.; Niederweis, M.; Gundlach, J. H. *Nat. Biotechnol.* **2012**, *30*, 349.

(40) Fennouri, A.; Przybylski, C.; Pastoriza-Gallego, M.; Bacri, L.; Auvray, L.; Daniel, R. *ACS Nano* **2012**, *6*, 9672.

(41) Biesemans, A.; Soskine, M.; Maglia, G. *Nano Lett.* **2015**, *15*, 6076.

(42) Choi, L. S.; Mach, T.; Bayley, H. *Biophys. J.* **2013**, *105*, 356.

(43) Cracknell, J. A.; Japrung, D.; Bayley, H. *Nano Lett.* **2013**, *13*, 2500.

(44) Rodriguez-Larrea, D.; Bayley, H. *Nat. Nanotechnol.* **2013**, *8*, 288.

(45) Boersma, A. J.; Bayley, H. *Angew. Chem. Int. Ed. Engl.* **2012**, *51*, 9606.

(46) Meller, A.; Nivon, L.; Branton, D. *Phys. Rev. Lett.* **2001**, *86*, 3435.

(47) Howorka, S.; Bayley, H. *Biophys. J.* **2002**, *83*, 3202.

(48) Shim, J. W.; Tan, Q.; Gu, L. Q. *Nucleic Acids Res.* **2009**, *37*, 972.

(49) Denissenko, M. F.; Pao, A.; Tang, M.; Pfeifer, G. P. *Science* **1996**, *274*, 430.

(50) Church, G.; Deamer, D. W.; Branton, D.; Baldarelli, R.; Kasianowicz, J.; Characterization of individual polymer molecules based on monomer-interface interactions. U.S. Patent 5,795,782. Mar 17, 1995

(51) White, R. J.; Zhang, B.; Daniel, S.; Tang, J. M.; Ervin, E. N.; Cremer, P. S.; White, H. S. *Langmuir* **2006**, *22*, 10777.

(52) Seed, B. *Silanizing Glassware*; John Wiley & Sons, Inc., 2001.

(53) de Zoysa, R. S.; Krishantha, D. M.; Zhao, Q.; Gupta, J.; Guan, X. *Electrophoresis* **2011**, *32*, 3034.

(54) Guy, A. T.; Piggot, T. J.; Khalid, S. *Biophys. J.* **2012**, *103*, 1028.

(55) Mathe, J.; Aksimentiev, A.; Nelson, D. R.; Schulten, K.; Meller, A. *Proc. Natl. Acad. Sci. U. S. A.* **2005**, *102*, 12377.

(56) An, N.; Fleming, A. M.; White, H. S.; Burrows, C. J. *Proc. Natl. Acad. Sci. U. S. A.* **2012**, *109*, 11504.

(57) Schibel, A. E.; An, N.; Jin, Q.; Fleming, A. M.; Burrows, C. J.; White, H. S. *J. Am. Chem. Soc.* **2010**, *132*, 17992.

(58) Pfeifer, G. P.; Besaratinia, A. *Hum. Genet.* **2009**, *125*, 493.

(59) Godschalk, R. W.; Van Schooten, F. J.; Bartsch, H. *J. Biochem. Mol. Biol.* **2003**, *36*, 1.

(60) Chuang, C. Y.; Tung, J. N.; Su, M. C.; Wu, B. C.; Hsin, C. H.; Chen, Y. J.; Yeh, K. T.; Lee, H.; Cheng, Y. W. *Arch. Oral. Biol.* **2013**, *58*, 102.

(61) Aksimentiev, A.; Schulten, K. *Biophys. J.* **2005**, *88*, 3745.

(62) Henrickson, S. E.; DiMarzio, E. A.; Wang, Q.; Stanford, V. M.; Kasianowicz, J. J. *J. Chem. Phys.* **2010**, *132*, 135101.

(63) Sauer-Budge, A. F.; Nyamwanda, J. A.; Lubensky, D. K.; Branton, D. *Phys. Rev. Lett.* **2003**, *90*, 238101.

(64) Jin, Q.; Fleming, A. M.; Burrows, C. J.; White, H. S. *J. Am. Chem. Soc.* **2012**, *134*, 11006.

(65) Viasnoff, V.; Chiaruttini, N.; Bockelmann, U. *Eur. Biophys. J.* **2009**, *38*, 263.

(66) Zhang, X.; Wang, Y.; Fricke, B. L.; Gu, L. Q. *ACS Nano* **2014**, *8*, 3444.

(67) Schibel, A. E. P.; Fleming, A. M.; Jin, Q.; An, N.; Liu, J.; Blakemore, C. P.; White, H. S.; Burrows, C. J. *J. Am. Chem. Soc.* **2011**, *133*, 14778.

(68) Jin, Q.; Fleming, A. M.; Johnson, R. P.; Ding, Y.; Burrows, C. J.; White, H. S. *J. Am. Chem. Soc.* **2013**, *135*, 19347.

(69) Jin, Q.; Fleming, A. M.; Ding, Y.; Burrows, C. J.; White, H. S. *Biochemistry* **2013**, *52*, 7870.

(70) Johnson, R. P.; Fleming, A. M.; Burrows, C. J.; White, H. S. *J. Phys. Chem. Lett.* **2014**, *5*, 3781.

(71) Johnson, R. P.; Fleming, A. M.; Jin, Q.; Burrows, C. J.; White, H. S. *Biophys. J.* **2014**, *107*, 924.

CHAPTER 2

EFFECT OF THE ELECTRIC DOUBLE LAYER ON THE ACTIVATION ENERGY OF ION TRANSPORT IN CONICAL NANOPORES

2.1 Introduction

This chapter presents a fundamental study of ion transport in conical-shaped nanopores using the activation energy (E_A) of ion transport as a parameter. The results highlight the relationships between the distribution of ions with the nanopore, ionic current, and E_A, and their dependence on pore size, temperature, ion concentration, and applied voltage. Ion transport phenomena in nanopores have attracted significant attention over the past 15 years in the context of the development of nanoscale resistive pulse sensors[1-8] and in fundamental studies of transport in confined spaces.[9-15] The push towards high performance energy storage devices also requires a fundamental understanding of ion transport phenomena near charged surfaces on the nanometer length scale.[16-23]

Typically, nanopores are constructed within polymers, glass, or silica, and have internal and external surfaces that are electrically charged. In an electrolyte, these charged surfaces attract counter ions from solution, resulting in the creation of an electric double layer (EDL) that screens the surface charge over a distance that is dependent primarily on the electrolyte concentration, but also the temperature. At the nanoscale domain, where the length of the EDL is comparable to that of the pore diameter, the consequences of the

EDL on the ion transport, and subsequently the current-voltage (*i*-*E*) characteristics, are significant, with non-linear *i*-*E* behavior typically observed.[24-34] However, the effect of temperature on ion transport in nanoscale domains has not been investigated in detail with the exception of the recent work published by Taghipoor and coworkers.[35] These researchers examined the temperature dependence of ion transport through uniform (35 nm height) nanochannels.

In this chapter, we examine how the presence of EDLs inside a conical glass nanopore affect the temperature dependence of ion transport, and by extension, the energy required for electrolyte transport through the nanopore. In any electrolyte solution, the movement of an ion by diffusion and migration along a potential gradient is associated with an activation energy, E_A. We experimentally measured E_A for electrolyte transport through conical glass nanopores of several pore sizes and varying electrolyte concentrations, as schematically shown in Figure 2.1.

In conjunction with our experiments, we have performed a systematic series of finite element simulations to compute E_A in conical nanopores based on the Poisson-Nernst-Planck model for ion transport. We show that at low electrolyte concentrations and in small pores, the confined geometry alters E_A for electrolyte transport relative to that in bulk solution. In agreement with expectations based on the Gouy-Chapman theory,[36] our simulations show that the electric potential profile perpendicular to the pore walls is strongly dependent on the temperature, resulting in significant changes in the ion concentration profile as the temperature is altered. This temperature dependence results in unusual potential-dependent values of E_A for ion transport through a nanopore.

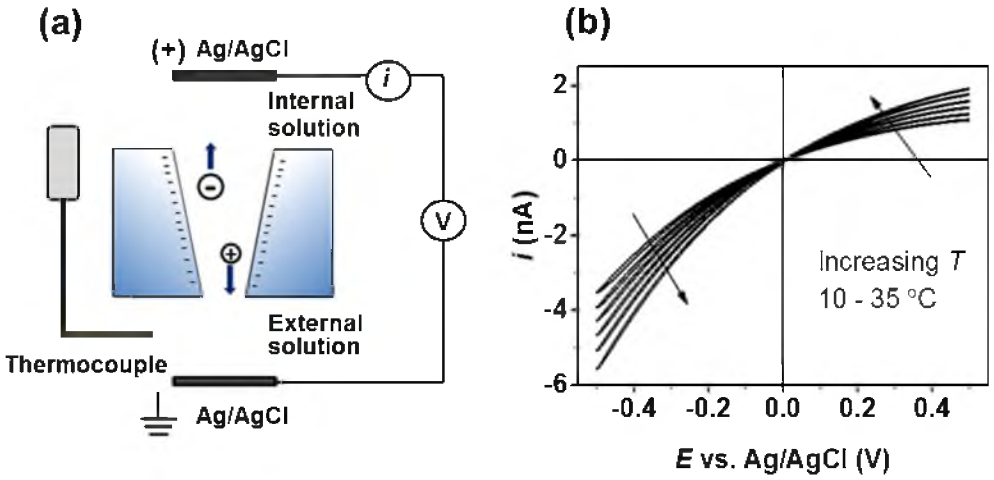

Figure 2.1. (a) Experimental design for measuring the temperature- and electrolyte concentration-dependent *i-E* response for conical glass nanopores. KCl electrolyte is placed both inside the capillary and in the external reservoir, and a voltage applied across the two Ag/AgCl electrodes. Temperature is controlled by a Peltier heater/cooler, and measured via a K-type thermocouple. (b) Representative *i-E* curves recorded at a scan rate of 10 mV s^{-1} and temperatures between 10 and 35 °C for a 35 nm pore in 0.1 mM KCl electrolyte. *E* refers to the potential of the Ag/AgCl electrode in the internal solution relative to the external solution.

2.2 Experimental Section

2.2.1 Chemicals and Materials

All solutions were prepared using water (18.1 MΩ cm) obtained from a Banstead E-pure system. KCl (99.8%, Fisher Scientific) was used without further purification. All electrolyte solutions were filtered using a 0.22 μm filter (Millipore, Inc.) prior to use.

2.2.2 Glass Nanopore Membrane (GNM) Fabrication

Glass nanopore membranes were prepared from soda-lime glass capillaries (Dagan) as previously reported by our lab.[37] The half-cone angle of the glass nanopore was estimated by optical microscopy and found to be 10.0 ± 1.5°. The radius of the orifice was determined from the ionic resistance (R) of the pore in 1 M KCl solution at a temperature of 25 °C using the expression $r = 18.5/R$.[26] Four nanopores with radii of 20 nm, 35 nm, 56 nm, and 2000 nm were used. The uncertainty in the radii is approximately ~10 %.

2.2.3 Cell Configuration and Data Acquisition

Current-voltage (i-E) curves were recorded using a CH Instruments 1030A potentiostat (Austin, TX). One Ag/AgCl Electrode was placed inside the capillary and the other (taken to be ground in these experiments) was placed in the external electrolyte reservoir. The voltage was scanned between 0.5 V and -0.5 V, starting from 0.5 V, at a scan rate of 10 mV s^{-1}. Temperature control was achieved by a Peltier heater/cooler (custom PID control of a small-scale thermoelectric cooler (CUI Inc., CP20151)) situated directly below the cell, while the temperature was measured by a K-type thermocouple immersed in the solution of the external reservoir. i-E curves were recorded at

temperatures between 10 and 45 °C (results for temperatures between 10 and 35 °C are reported in the main text, the full range is considered in the Figure S2.1), and in electrolyte concentrations of 0.1 to 50 mM (with the 1 M solution used only for measuring nanopore sizes). The temperature is measured by a thermocouple (0.1 °C precision) residing in the same solution as the pore (volume 350 μL) which has a lid on top. The distance between the pore orifice and the thermocouple is <2 mm, which will lead to minimal temperature differences between them. These components lie within a much larger polycarbonate block (~1 inch cube). The relatively large thermal mass of the block results in stable temperatures of the solution. A thermal equilibrium is reached in ~2 min and each measurement reported herein was taken after standing a minimum of 5 min to equilibrate, after which the solution (internal and external) and thermocouple will be at the same temperature.

2.2.4 Computational Analysis and Simulations

Finite element simulations were performed with COMSOL Multiphysics 4.3 (COMSOL Inc.) on a desktop computer (Intel Core i7 CPU with 8 GB RAM). Details of the boundary conditions and meshing are presented later.

2.3 Results and Discussion

2.3.1 Experimental Activation Energies

Using the experimental configuration shown in Figure 2.1(a), the current-voltage (*i-E*) response of conical glass nanopores of 20, 35, 56, and 2000 nm radius were recorded as a function of both temperature (10 - 35 °C) and KCl concentration (0.1 – 50 mM). The observed non-ohmic *i-E* response (Figure 2.1b), or ion-current rectification (ICR), is more

prominent for lower electrolyte concentrations and smaller pores. ICR occurs in asymmetric charged nanopores and is due to the generation of an EDL at the interface between the nanopore walls and the electrolyte, and can be explained by an ion accumulation-depletion model.[38-40] Due to the conical shape of the nanopore, when a negative potential is applied to the interior of the nanopore relative to the exterior, positively charged K^+ ions move from the bulk solution towards the interior of the pore while negatively charged Cl^- ions move in the opposite direction. However, since the pore wall is negatively charged, K^+ accumulate at the pore orifice while the transit of Cl^- ions is partially blocked, resulting in an accumulation of both ions and a conductance higher than the bulk value. Conversely, when a positive voltage is applied to the interior of the pore, Cl^- ions will be rejected by the pore and ions will be depleted at the pore orifice giving rise to a lower conductivity. Accumulation of ions may still occur when a pore is geometrically symmetric; however, the *i-E* response also is symmetric.[41-44]

From the individual *i-E* traces, we extracted values of the current between -0.5 and 0.5 V as a function of both KCl concentration and temperature. At negative voltages, a slight hysteresis of ~2% current (at -0.35 V) is observable between the forward and backward scan and thus the average of the current on the forward and backward scans was used. The current is proportional to the flux of the ions through the pore (diffusion and migration), and there is an energy penalty associated with moving ions through the nanopore. This activation energy (E_A) is related to the measured current at a given voltage by the Arrhenius equation:

$$i = A\exp\left(-\frac{E_A}{RT}\right) \tag{2.1}$$

where R is the gas constant, T is the temperature and A is the pre-exponential factor. The resulting Arrhenius plots are linear (Figure 2.2a and b and S2.2) over the range 10 – 35 °C. However, at temperatures > 35 °C, slight nonlinear behavior becomes apparent (see Figure S2.1); only data between 10 - 35 °C were used in the analysis presented here.

Values of E_A measured as a function of electrolyte concentration and pore size are shown in Figures 2.2c and 2.2d. For the 2000 nm pore, E_A does not show any significant change with the electrolyte concentration above 1 mM KCl and is equal to 13.4 ± 0.3 kJ mol^{-1}, comparable to E_A (13.5 ± 0.2 kJ mol^{-1}) based on temperature-dependent conductance values reported for bulk solution.[45]

As the pore diameter is reduced, the charge on the nanopore surface begins to influence ion transport, resulting in E_A values different from that observed in bulk solution. The effect is greatest when small nanopores are employed in conjunction with low electrolyte concentrations. At positive potentials, as shown in Figure 2.2c, E_A increases above the value observed in bulk solution, whereas at negative potentials, as shown in Figure 2.2d, a decrease in E_A is observed. This dependence of E_A on the voltage is discussed below. A similar dependence on E_A on the electrolyte concentration and at different voltages for a 20 nm radius nanopore is presented in the S2.10.

2.3.2 Finite Element Simulations

Finite element simulations were used to understand how the nanopore geometry influences E_A for ion transport relative to that observed in bulk solution, and to explain the dependence of E_A on the applied potential, nanopore radius, and KCl concentration. The

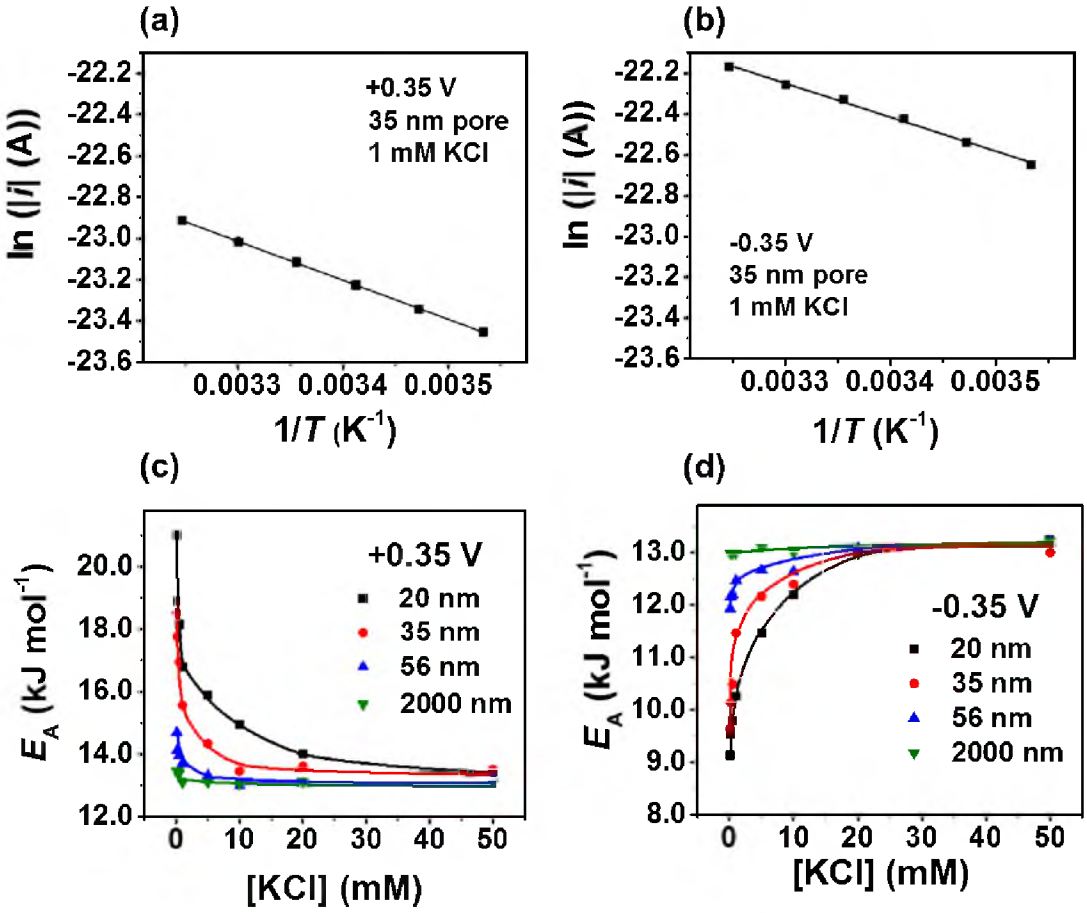

Figure 2.2. Determining the activation energy of electrolyte transport through a conical glass nanopore. (a,b) Representative Arrhenius plots constructed from ionic currents measured at +0.35 V and -0.35 V for a 35 nm pore in 1 mM KCl electrolyte. (c,d) E_A as a function of both KCl concentration and pore size at +0.35 V and -0.35 V, respectively. Error bars, representing the standard deviation of 3 repeated current recordings and the standard error arising from the least squares fit to ln ($|i|$) - T^{-1} data are smaller than the data points used to present experimental E_A values in this paper.

ion fluxes from each simulation were integrated over the boundaries of the simulation domain to compute the ionic current at different temperatures. An Arrhenius analysis of the dependence of the simulated current on temperature was used to compute values of E_A for comparison to experimental data.

The 2D axisymmetric finite element model used to simulate the ionic current in conical nanopores is shown in Figure 2.3. A fine mesh is necessary to resolve the EDL potential and ion distribution on the charged walls. As such, the mesh size was fixed at 0.35 nm on the charged walls near the pore orifice (boundaries EF and FG in Figure 2.3), which is ~1/4 of the reciprocal Debye length (~1.3 nm) for the conditions giving the smallest double layer (50 mM, 10 °C). All other meshing parameters were left at the default values defined in the software for a 'normal' mesh. We confirmed that our mesh was sufficiently fine by observing that a mesh consisting of elements of half the size gave no change in the solution.

The half-cone angle of the glass nanopore was estimated by optical microscopy and found to be 10.0 ± 1.5°. Since the cone angle can vary from pore-to-pore by 15%, we also conducted simulations over a range of cone-angles between 8-12° while keeping the electrolyte concentration and voltage constant (see Figure S2.3). Calculated values of E_A were found to vary by less than 2% over this range of angles.

The surface charge of the pore wall was kept constant at -2 mC/m^2 for all simulations, which is reasonable for the range of electrolyte concentrations used (0.02 mM - 50 mM) at pH 7.0.[39,40,45-47] Changes in surface charge density as a function of electrolyte concentration were not included as they have been shown to be negligible tor the range of experimental conditions used (i.e., <0.1 M, 0 – 35 °C); however, some dependence of the

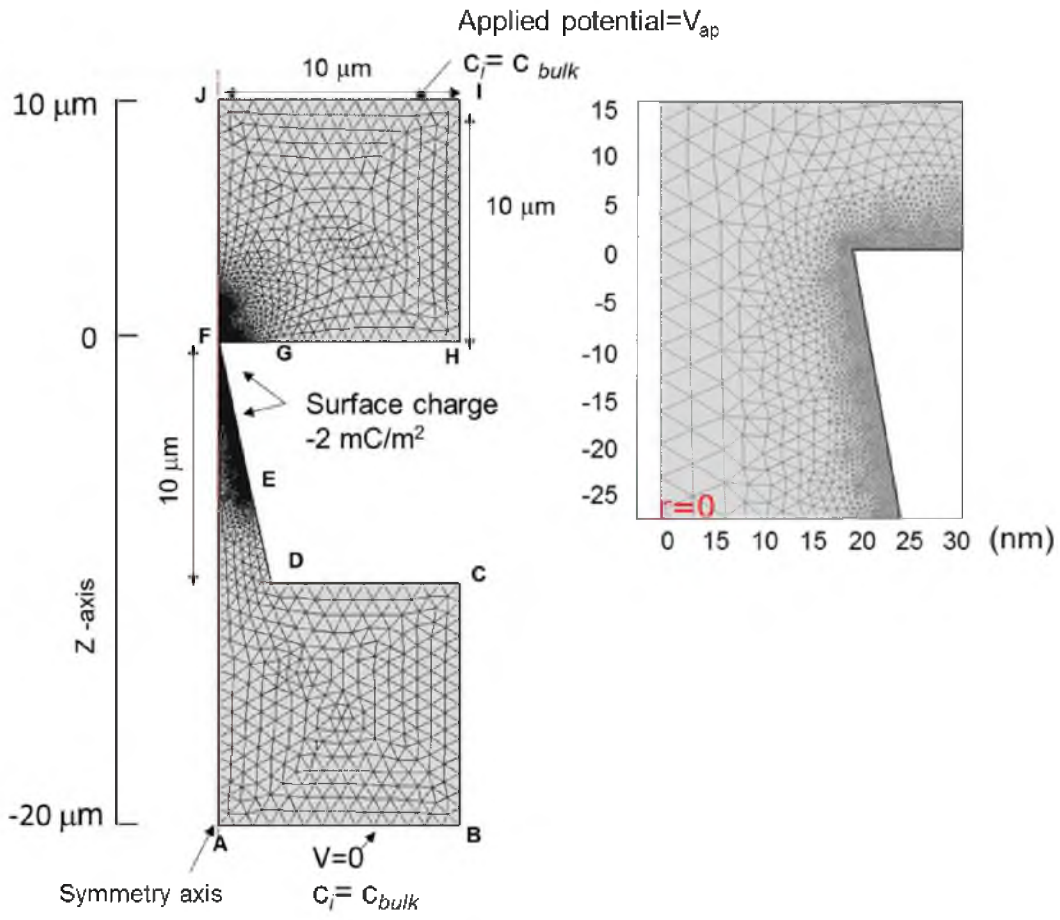

Figure 2.3. The 2D axisymmetric finite element model used to simulate the current through a conical pore as a function of temperature, voltage, and ion concentration. The boundary conditions and mesh are shown in the figure. A potential is applied to IJ while AB is held at zero potential. The electrolyte concentration at AB and IJ is maintained at the bulk value. A surface charge of -2 mC/m^2 is applied to EF and FG and a finer mesh size is used close to the pore orifice. The boundaries far from the pore orifice (GH, ED and CD) are set at zero charge, which does not appreciably affect the calculated currents. This allows for a coarser mesh in these regions, as no double-layer need be resolved. AJ is the symmetry axis. The total normal ion flux (mol/m^{2}s) at the semi-infinite boundary AB was computed by an integration and converted to the ionic current (C/s) by multiplying by Faraday's constant (96500 C/mol). The inset shows the expanded area of the pore mouth.

surface charge on electrolyte concentration would be expected at higher concentrations and temperatures.[35] A recent study by Taghipoor et al. has reported the dependence of surface charge of silicon dioxide with temperature (~16 mC/m^2 in 0.1m M KCl at 25 °C).[35] An equation for the dependence of the surface charge on temperature was extracted from values reported in this work to study the effect of temperature on E_A. However, E_A values calculated by this method are not in reasonable agreement with the experimental values (see Figure S2.4). These findings suggests that the glass nanopores used in these experiments do not bear a surface charge as high as ~-16 mC/m^2 (at 25 °C) and/or the dependence of the surface charge on temperature is not as significant as reported for silicon dioxide by Taghipoor et al.

All simulations are based on solving the coupled Poisson and Nernst-Planck equations, which describe the local ion distributions and the ion fluxes, respectively, as a function of the local electrical potential, Φ. The ionic flux, J, of species i (K^+ or Cl^-) is given by:

$$J_i = -D_i \nabla c_i - z_i \mu_i F c_i \nabla \Phi \tag{2.2}$$

where D_i, c_i, and z_i are the diffusivity, concentration, and charge of ionic species, respectively, and μ_i represents the ionic mobility. T, F, and R are the temperature, Faraday's constant, and the gas constant, respectively.

The relationship between the local ion distributions and potential is given by:

$$\nabla^2 \Phi = -\frac{F}{\varepsilon} \sum_i z_i c_i \tag{2.3}$$

where $\varepsilon = 78$ is the dielectric constant of the medium.

The use of the Nernst-Planck (NP) equation to describe ion fluxes is reasonable when the applied pressure is zero and the electro-osmotic flow is negligible, conditions that match those used in this experiment.[48-51] Solving the coupled Poisson and Nernst-Planck equations as a function of temperature requires that D_i for K^+ and Cl^- are known as a function of temperature. We used the Stokes-Einstein relationship to estimate the ion diffusion coefficients:

$$D_i = \frac{k_B T}{6\pi\eta(T) r_i} \tag{2.4}$$

where k_B is the Boltzmann constant, $\eta(T)$ represents the dynamic viscosity of the medium and r_i is the radii of the ions. Since $\eta(T)$ is temperature dependent, literature values were used to construct an expression that accurately describes the dependence of $\eta(T)$ over the 10 – 35 °C range studied[53]. Details of this calculation are presented in the S2.5.

Representative simulated Arrhenius plots of $\ln|i|$ vs T^{-1} are shown in Figure 2.4a and b. Additional Arrhenius plots at different concentrations are given in Figure 2.6. For the experimental Arrhenius plots (Figures 2.2a and b), we observe a linear trend within this temperature range. Linear fits to these plots were used to calculate E_A for electrolyte transport. This process was repeated for a range of electrolyte concentrations, pore sizes and potentials, chosen to match the experimental conditions for direct comparison. Calculated values of E_A are displayed in Figure 2.4c and d.

The trends for simulated activation energies (Figure 2.4c and d) are in qualitative agreement with the experimental values (Figure 2.2c and d); activation energies increased

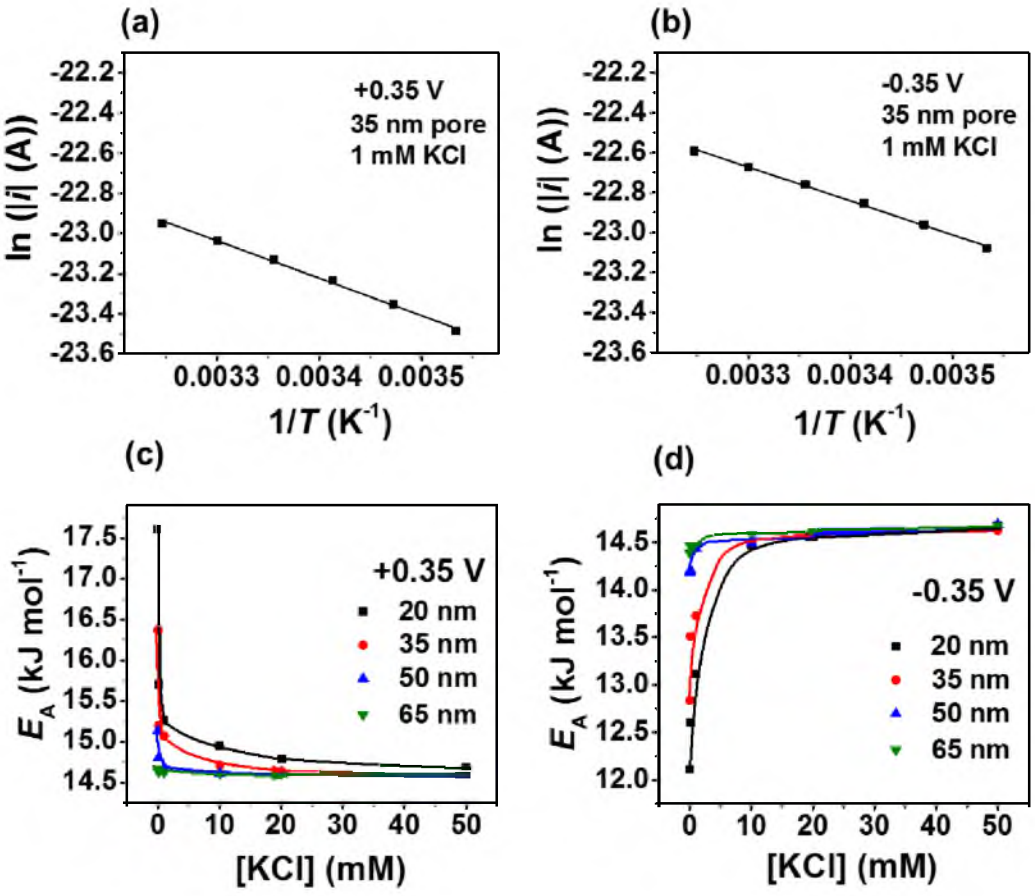

Figure 2.4. Simulated activation energies of electrolyte transport through a conical glass nanopore. (a,b) Representative Arrhenius plots constructed for currents measured at +0.35 V and -0.35 V for a 35 nm pore in 1 mM KCl electrolyte, from which E_A are calculated. (c,d) Simulated E_A as a function of both KCl concentration and pore size at +0.35 V and -0.35 V, respectively. See Figure 2.2 for a direct comparison to the experimental Arrhenius plots and values of E_A for the same conditions.

at positive external potentials and decreased at negative potentials. The slight difference in the values of experimental and simulated values of E_A at higher concentrations (13.4 ± 0.1 kJ mol^{-1} and 14.7± 0.1 kJ mol^{-1}) arises because the diffusion coefficient depends on concentration as well as temperature.[52] The simulations were performed using the temperature-dependent but concentration-independent diffusion coefficient (limit at infinite dilution, see Figure S2.5). The limiting value of E_A at high concentration derived from simulations is precisely as expected when compared to the experimental values at infinite dilution, upon which the model is based, thus confirming correct implementation of the model.

2.3.3 Dependence of Activation Energy as a Function of Applied Voltage

Both experimental and simulated values of E_A as a function of voltage for a 20 nm pore are given in Figure 2.5. In both the experiments and the simulations, E_A decreases relative to bulk values at negative potentials and increases relative to bulk values at positive potentials.

The resistance on the nanopore is determined by the solution at of the pore orifice and it is the potential- and temperature-dependent concentration distribution within this region that determines the dependence of E_A on the applied voltage. For low concentrations of KCl and small pores, where the deviation of activation energy from its value in bulk solution is largest, the concentrations of K^+ and Cl^- in the vicinity of the nanopore orifice are strongly dependent on the polarity of the applied potential. This is shown in Figure 2.6 through color distribution plots of the concentrations of K^+ and Cl^- for a 20 nm radius pore with 0.1 mM KCl at +0.35 V and -0.35 V. At both positive and negative applied voltages,

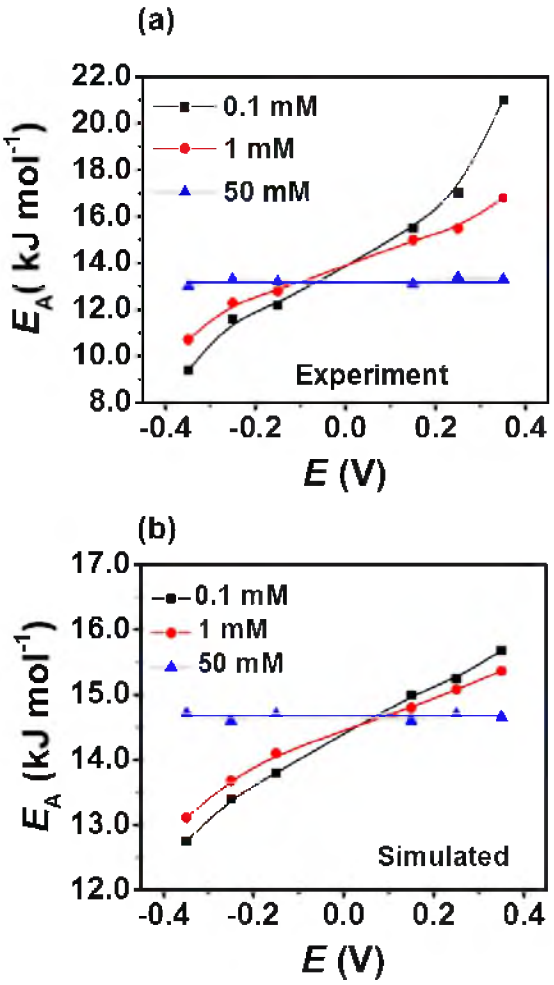

Figure 2.5. Experimental (a) and simulated (b) activation energies for a 20 nm pore for different KCl concentration as a function of applied potential. The error bars are smaller than the data points.

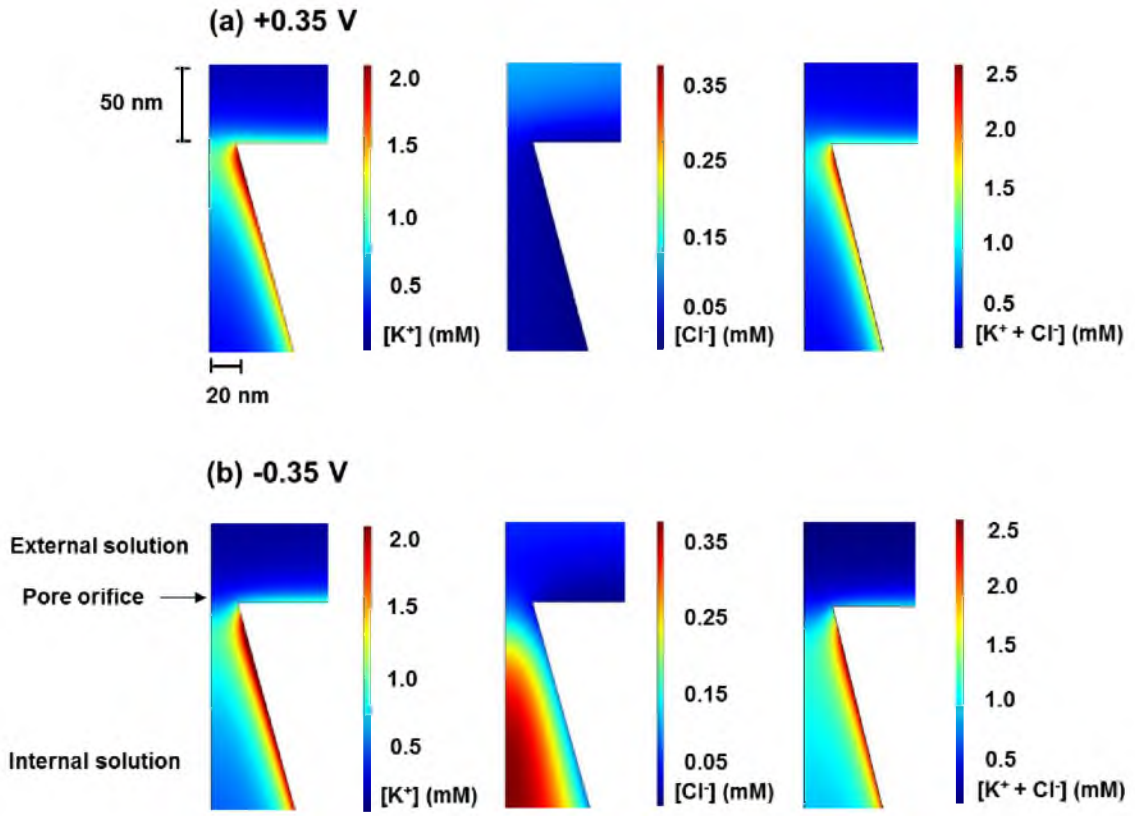

Figure 2.6. Concentration profiles of K^+ and Cl^- ions in the vicinity of a 20 nm nanopore orifice at (a) +0.35 V and (b) -0.35 V (relative to the internal electrode). The surface charge on the wall is -2 mC/m^2 and the bulk concentration is 0.1 mM at 25 °C. Note, different color scales are used for the two species. Plots for different pore sizes and cross-sectional plots of the species concertation are shown in Figure S2.7.

the K^+ concentration close to the pore opening is significantly higher than its value in bulk solution (0.1 mM) due to accumulation of the cation at the negatively charged pore wall. A slight inward shift and spreading of the zone of high K^+ concentration at the pore mouth is observed when changing from positive to negative applied potentials.

Conversely, the concentration of Cl^- ions is lowest on the pore walls; this is due to electrostatic repulsion from the negative surface charge. At positive applied potentials the concentration of Cl^- within the pore is less than that in bulk solution (~half its value in bulk solution for the conditions shown), whereas at the negative applied potentials an accumulation of Cl^- in the center of the pore is observed (~3.5 enhancement for these conditions) as they are simultaneously repelled by the charged walls and the applied potential. However, it is important to note that these Cl^- concentrations are smaller than those of the K^+ ion.

The total concentration of K^+ and Cl^- at the vicinity of the pore orifice is also shown in Figure 2.6. From this plot we can observe that the total ion concentration is greater for negative applied potentials compared to positive potentials for all but a small region from $z = 0$ to -15 nm. The comparatively higher concentration of ions when a negative potential is applied results in to the higher current magnitudes at negative potentials, for example, ICR, which can also be observed experimentally in the *i-E* curves of Figure 2.1b. E_A values are calculated directly from the current measured at different temperatures.

Figure 2.7 shows plots of the simulated total ionic concentration at +0.35V and -0.35V in the vicinity of a 20 nm nanopore orifice at two different temperatures. At -0.35 V, the ionic concentration in the vicinity of the pore orifice decreases as the temperature is increased from 10 °C to 35 °C. This can be seen in the concentration plot (Figure 2.7a),

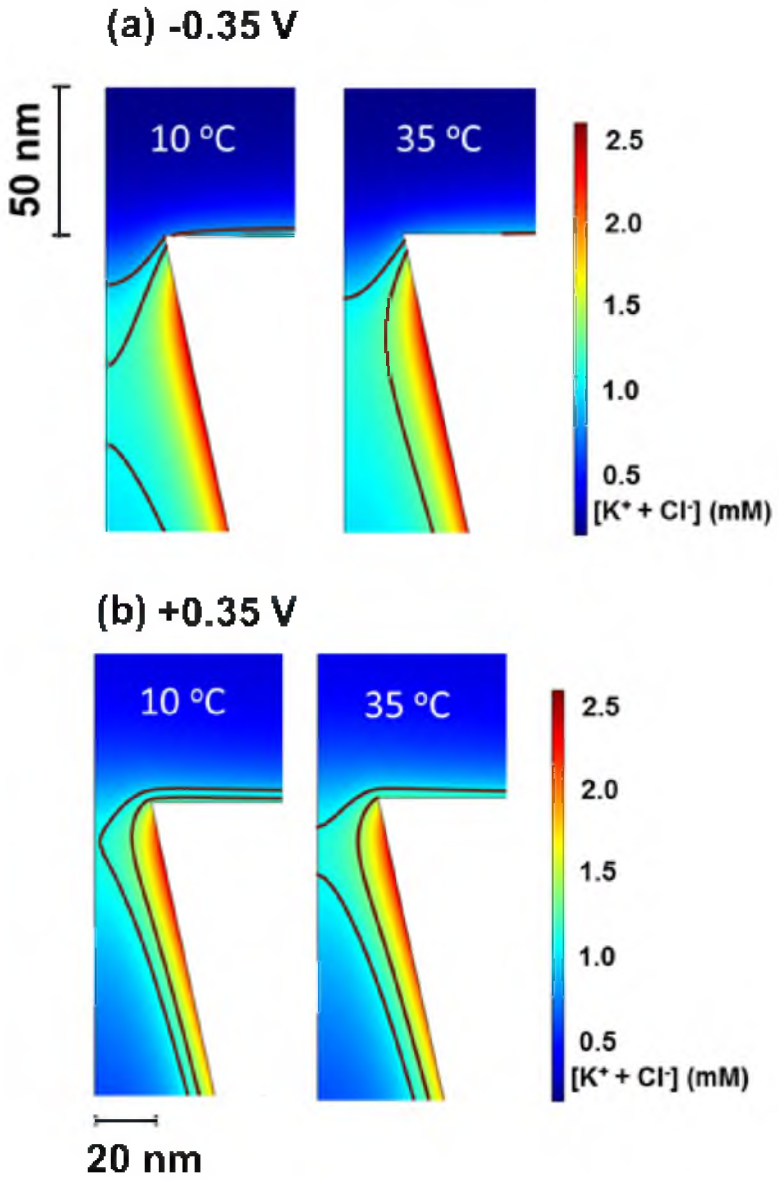

Figure 2.7. The total ionic concentration at the orifice of a 20 nm nanopore at 0.1 mM KCl, at 10 and 35 ºC and for (a) -0.35 V and (b) +0.35 V applied potential. Contours have been added at 1.0 and 1.3 mM to aid interpretation.

where contours have been added to aid in this interpretation. The opposite situation is observed at positive potentials, where an increase in ion concentration at the pore orifice is observed with increasing temperature.

The activation energy for transport through the pore describes the rate of change of current with temperature. The current, in turn, is affected by two factors, (i) the ion mobility, and (ii) the ion concentration. The increase in the mobility of the ions with increasing temperature is the main driving factor in the current increasing when the temperature is increased from 10 °C to 35 °C, and is the sole factor in bulk solution, where ion concentrations remain constant. If the current scaled solely by the increase in mobility we would expect the calculated E_A would be precisely the value for bulk solution (14.7 kJ mol^{-1}). Instead the change in nanopore current as a function of temperature is effectively modulated by the concentration of the ions at the vicinity of the nanopore orifice (where most of the resistance drop occurs). The lower concentration of ions with increasing temperature observed at negative voltages leads to a lower conductivity, a lower current, and hence, a value of E_A = 12.7 kJ mol^{-1} that is below that for bulk solution. Implicit in this reasoning is that the electric field is largely unchanged with changing temperature, as is shown in the Figure S2.9

At an applied potential of +0.35 V the ionic concentration within the nanopore increases as the temperature is increased, as seen in Figure 2.7b. The spreading of the region of higher concentration in the center of the pore can be visualized most easily by the 1.0 mM contour in the color plot (Figure 2.7b). In contrast to the situation with a negative applied potential, the increased concentration within the pore leads to an increase in current as the temperature is increased over and above that predicted by purely

considering the increase in mobility with temperature and explains the E_A=15.7 kJ mol^{-1} being greater than the value of E_A in bulk solution. Line graphs of total ion concentration at different temperatures inside a 20 nm nanopore is shown in Figure 2.8.

For larger pore geometries and/or higher electrolyte concentrations the Debye length represents a smaller proportion of the pore radius. The deviation of ion concentration from the bulk is confined closer (relatively) to the pore walls and as it is this deviation that is the source of the behaviors discussed above, activation energies in large pores and at high electrolyte concentrations remain similar to those in the bulk.

2.4 Conclusions

The apparent activation energies of ion transport through conical-shaped glass nanopores of varying size and over a range of electrolyte concentrations have been measured experimentally. At low electrolyte concentrations (< 50 mM) and small pore radii (< ~100 nm), E_A deviates from the value observed in bulk, increasing at positive applied potentials and decreasing at negative potentials. Finite element simulations support our interpretation that the change in the E_A can be explained by changes in the ion concentration profile within the pore as a function of temperature and voltage. At negative potentials, the ion concentration inside the pore decreases as a function of temperature, moderating the mobility-driven increase in conductivity with temperature, and hence decreasing the activation energy relative to bulk solution. At positive potentials, the rate of change in conductivity with temperature is enhanced by an increase in ion concentration within the pore as a function of temperature. These two dependencies suggest that the

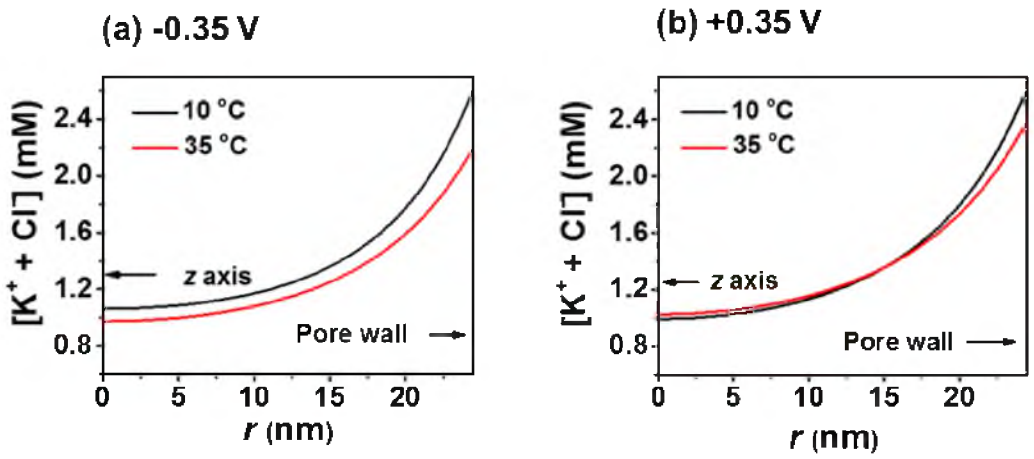

Figure 2.8. The total ionic concentration at the orifice of a 20 nm nanopore at 0.1 mM KCl, at 10 ℃ and 35 ℃. (a) Radial cross section plot taken inside the pore at z = -20 nm at -0.35 V and (b) +0.35 V. Individual concentration profiles along z axis are given in Figure S2.8

agreement with the expectation that the effect of the electrostatic fields in determining ion distributions is reduced at higher temperatures. These effects may be applied to conical nanopores if their surface charge and geometry are fixed in the temperature range studied.

2.5 References

(1) Lan, W. J.; Holden, D. A.; Liu, J.; White, H. S. *J. Phys. Chem. C* **2011**, *115*, 18445.

(2) DeBlois, R. W.; Wesley, R. K. *J. Virol.* **1977**, *23*, 227.

(3) Sexton, L. T.; Mukaibo, H.; Katira, P.; Hess, H.; Sherrill, S. A.; Horne, L. P.; Martin, C. R. *J. Am. Chem. Soc.* **2010**, *132*, 6755.

(4) Jin, P.; Mukaibo, H.; Horne, L. P.; Bishop, G. W.; Martin, C. R. *J. Am. Chem. Soc.* **2010**, *132*, 2118.

(5) Han, J.-H.; Kim, K. B.; Kim, H. C.; Chung, T. D. *Angew. Chemie. Int. Ed.* **2009**, *48*, 3830.

(6) Umehara, S.; Pourmand, N.; Webb, C. D.; Davis, R. W.; Yasuda, K.; Karhanek, M. *Nano Lett.* **2006**, *6*, 2486.

(7) Siwy, Z.; Trofin, L.; Kohli, P.; Baker, L. A.; Trautmann, C.; Martin, C. R. *J. Am. Chem. Soc.* **2005**, *127*, 5000.

(8) Wanunu, M.; Morrison, W.; Rabin, Y.; Grosberg, A. Y.; Meller, A. *Nat. Nanotecnol.* **2010**, *5*, 160.

(9) Pu, Q.; Yun, J.; Temkin, H.; Liu, S. *Nano Lett.* **2004**, *4*, 1099.

(10) Van der Heyden, F. H.; Stein, D.; Dekker, C. *Phys. Rev. Lett.* **2005**, *95*, 116104.

(11) Plecis, A.; Schoch, R. B.; Renaud, P. *Nano Lett.* **2005**, *5*, 1147.

(12) Pennathur, S.; Santiago, J. G. *Anal. Chem.* **2005**, *77*, 6772.

(13) Pennathur, S.; Santiago, J. G. *Anal. Chem.* **2005**, *77*, 6782.

(14) Baldessari, F.; Santiago, J. G. *J. Nanobiotechnol.* **2006**, *4*, 12.

(15) Hibara, A.; Saito, T.; Kim, H.-B.; Tokeshi, M.; Ooi, T.; Nakao, M.; Kitamori, T. *Anal. Chem.* **2002**, *74*, 6170.

(16) Balke, N.; Kalnaus, S.; Dudney, N. J.; Daniel, C.; Jesse, S.; Kalinin, S. V. *Nano Lett.* **2012**, *12*, 3399.

(17) Okubo, M.; Tanaka, Y.; Zhou, H.; Kudo, T.; Honma, I. *J. Phys. Chem. B* **2009**, *113*, 2840.

(18) Rolison, D. R.; Long, J. W.; Lytle, J. C.; Fischer, A. E.; Rhodes, C. P.; McEvoy, T. M.; Bourg, M. E.; Lubers, A. M. *Chem. Soc. Rev.* **2009**, *38*, 226.

(19) Long, J. W.; Dunn, B.; Rolison, D. R.; White, H. S. *Chem. Rev.* **2004**, *104*, 4463.

(20) Gowda, S. R.; Reddy, A. L. M.; Shaijumon, M. M.; Zhan, X.; Ci, L.; Ajayan, P. M. *Nano Lett.* **2011**, *11*, 101.

(21) Xiong, J.; Chen, Q.; Edwards, M. A.; White, H. S. *ACS Nano* **2015,** *9*, 8520

(22) Taghipoor, M.; Bertsch, A.; Renaud, P. *Phys. Chem. Chem. Phys* **2015**, *17*, 4160.

(23) James, T.; Kalinin, Y. V.; Chan, C. C.; Randhawa, J. S.; Gaevski, M.; Gracias, D. H. *Nano Lett.* **2012**, *12*, 3437.

(24) Wei, C.; Bard, A. J.; Feldberg, S. W. *Anal. Chem.* **1997**, *69*, 4627.

(25) Siwy, Z. S. *Adv. Funct. Mater.* **2006**, *16*, 735.

(26) White, R. J.; Zhang, B.; Daniel, S.; Tang, J. M.; Ervin, E. N.; Cremer, P. S.; White, H. S. *Langmuir* **2006**, *22*, 10777.

(27) Sa, N.; Baker, L. A. *J. Am. Chem. Soc.* **2011**, *133*, 10398.

(28) Xia, F.; Guo, W.; Mao, Y.; Hou, X.; Xue, J.; Xia, H.; Wang, L.; Song, Y.; Ji, H.; Ouyang, Q.; Wang, Y.; Jiang, L. *J. Am. Chem. Soc.* **2008**, *130*, 8345.

(29) Guerrette, J. P.; Zhang, B. *J. Am. Chem. Soc.* **2010**, *132*, 17088.

(30) Vlassiouk, I.; Kozel, T. R.; Siwy, Z. S. *J. Am. Chem. Soc.* **2009**, *131*, 8211.

(31) Yameen, B.; Ali, M.; Neumann, R.; Ensinger, W.; Knoll, W.; Azzaroni, O. *J. Am. Chem. Soc.* **2009**, *131*, 2070.

(32) Cheng, L.-J.; Guo, L. J. *Chem. Soc. Rev.* **2010**, *39*, 923.

(33) Kosinska, I. D. *J. Chem. Phys.* **2006**, *124*, 244707.

(34) Siwy, Z.; Heins, E.; Harrell, C. C.; Kohli, P.; Martin, C. R. *J. Am. Chem. Soc.* **2004**, *126*, 10850.

(35) Taghipoor, M.; Bertsch, A.; Renaud, P. *ACS Nano* **2015**, *9*, 4563.

(36) Bard, A. J.; Faulkner, L. R. *Electrochemical Methods, Fundamentals & Applications*, 2nd ed.; John Wiley & Sons: New Jersey, 2001.

(37) Zhang, B.; Galusha, J.; Shiozawa, P. G.; Wang, G.; Bergren, A. J.; Jones, R. M.; White, R. J.; Ervin, E. N.; Cauley, C. C.; White, H. S. *Anal. Chem.* **2007**, *79*, 4778.

(38) White, H. S.; Bund, A. *Langmuir* **2008**, *24*, 2212.

(39) Kubeil, C.; Bund, A. *J. Phys. Chem. C* **2011**, *115*, 7866.

(40) Lan, W.-J.; Kubeil, C.; Xiong, J.; Bund, A.; White, H. S. *J. Phys. Chem. C* **2014**, *118*, 2726.

(41) Hou, X.; Liu, Y.; Dong, H.; Yang, F.; Li, L.; Jiang, L. *Adv. Mater.* **2010**, *22*, 2440.

(42) Cheng, L.-J.; Guo, L. J. *Nano Lett.* **2007**, *7*, 3165.

(43) He, Y.; Gillespie, D.; Boda, D.; Vlassiouk, I.; Eisenberg, R. S.; Siwy, Z. S. *J. Am. Chem. Soc.* **2009**, *131*, 5194.

(44) Karnik, R.; Duan, C.; Castelino, K.; Daiguji, H.; Majumdar, A. *Nano Lett.* **2007**, *7*, 547.

(45) Wu, Y. C. K., W. F. Feng, D. Holland, L. A.; Juhasz, E.; Arvay, E. Tomek, A *J. Res. Natl. Inst. Stand. Technol.* **1994**, *99*, 241.

(46) Behrens, S. H.; Grier, D. G. *J. Chem. Phys.* **2001**, *115*, 6716.

(47) Sa, N.; Lan, W.-J.; Shi, W.; Baker, L. A. *ACS Nano* **2013**, *7*, 11272.

(48) Ai, Y.; Zhang, M.; Joo, S. W.; Cheney, M. A.; Qian, S. *J. Phys. Chem. C* **2010**, *114*, 3883.

(49) Daiguji, H.; Yang, P.; Majumdar, A. *Nano Lett.* **2003**, *4*, 137.

(50) Vlassiouk, I.; Siwy, Z. S. *Nano Lett.* **2007**, *7*, 552.

(51) Kubeil, C.; Bund, A. *J. Phys. Chem. C* **2011**, *115*, 7866.

(52) *Handbook of Chemistry and Physics*; 95th ed.; CRC Press: Florida, 2014.

(53) Bakajin, O.; Noy, A.; Fornasiero, F.; Park, H. G.; Holt, J.; Kim, S. Membranes with functionalized carbon nanotube pores for selective transport. US8940173. Dec 10, 2009.

(54) Robinson, R. A.; Stokes, R. H. *Electrolyte Solutions*; 2nd ed.; Dover Publications: London, 2002.

(55) Swindells, J. F.; Coe, J. R.; Godfrey, T. B. *J. Appl. Phys.* **1944**, *15*, 625.

S2.6 Supplemental Material

S2.6.1 Arrhenius Plot over an Extended Range of Temperature

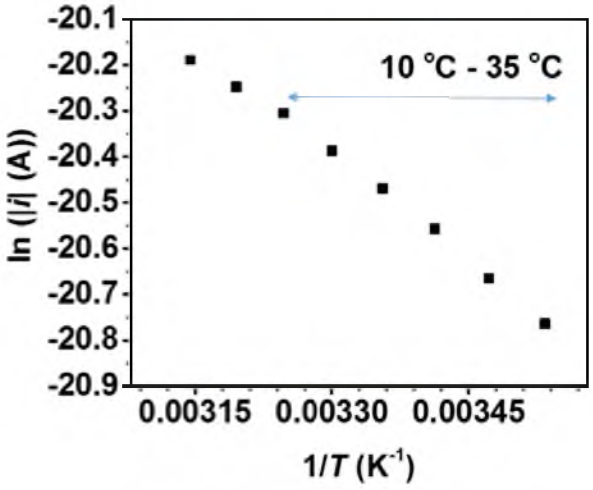

Figure S2.1. A sample Arrhenius plot (ln $|i|$ vs T^{-1}) for values of i measured at 0.35 V for a 65 nm pore at 100 mM KCl from 10 ºC to 45 ºC showing the nonlinearity of the curve over a wider temperature range. Nonlinear behavior was observed for other pores and concentrations. The linear range 10 ºC to 35 ºC was chosen for all the experiments.

S2.6.2 Arrhenius Plots for a 35 nm Radius Pore at Different KCl Concentrations

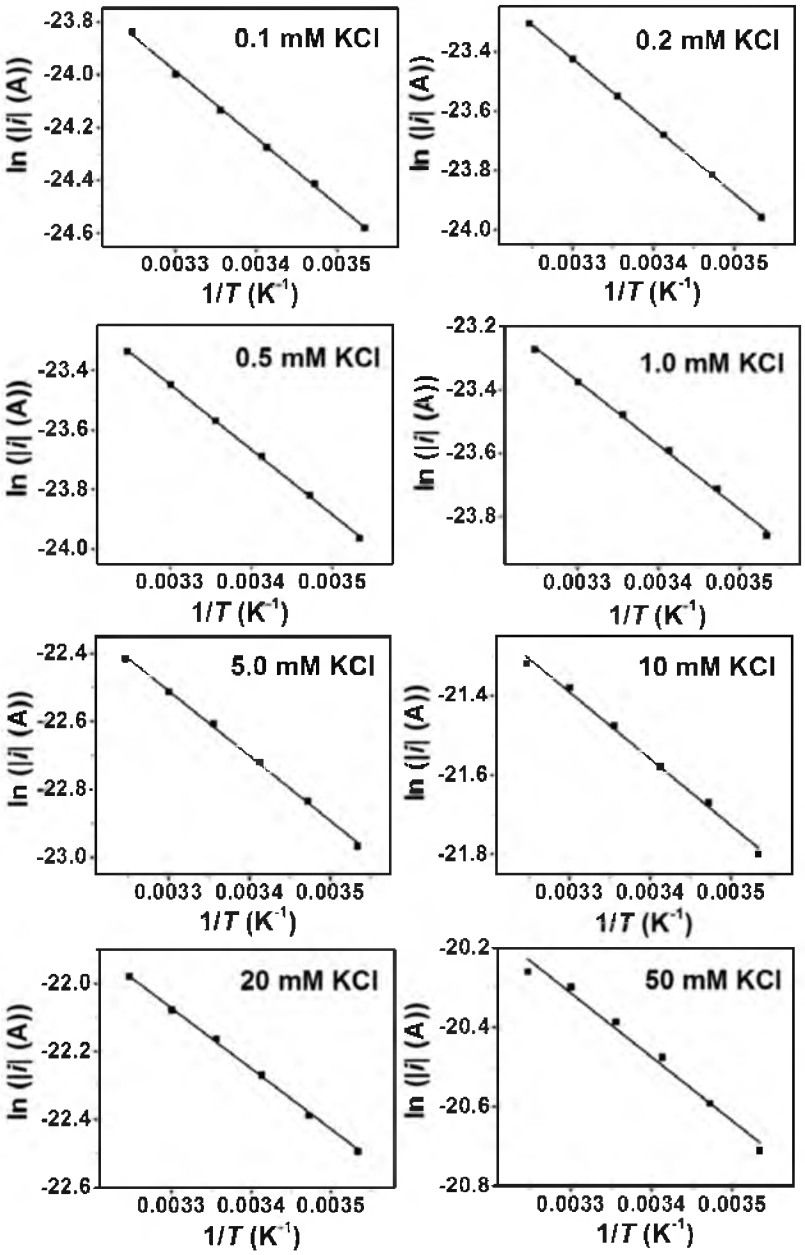

Figure S2.2. Arrhenius plots (ln $|i|$ vs T^{-1}) for values of i measured at 0.35 V for a 35 nm pore. The above Arrhenius plots were used to extract the activation energy values presented in Figure 2.2 of the main text, at +0.35 V for a 35 nm pore.

S2.6.3 Assessment of the uncertainty in simulated activation energy due to measurement error in the half-cone angle

The half-cone angles of the pores were determined by optical microscopy and were estimated to be 10 ±1.5°. The radii of the pores were then determined from *i-E* measurements as described in our previous work, assuming a half-cone angle of 10°.[26] Uncertainty in the half-cone angle gives rise to uncertainty in the pore radius. Figure S2.3b plots pairs of radius and half-cone angle that all give a resistance of 9.18 MΩ (9.18 MΩ corresponds to the measured resistance of a 20 nm pore of a cone angle 10° in 0.1 mM KCl at 25 °C). In this example, a half-cone angle of 10° gives a radius of 20 nm. Figure S2.3c shows the simulated activation energies for several radius/half-cone angle pairs. (only the half-cone angle is labelled). The ±1.5° uncertainty in the half-cone angle gives an uncertainty of 0.3 kJ/mol the simulated activation energies, indicating this is not a significant source of uncertainty.

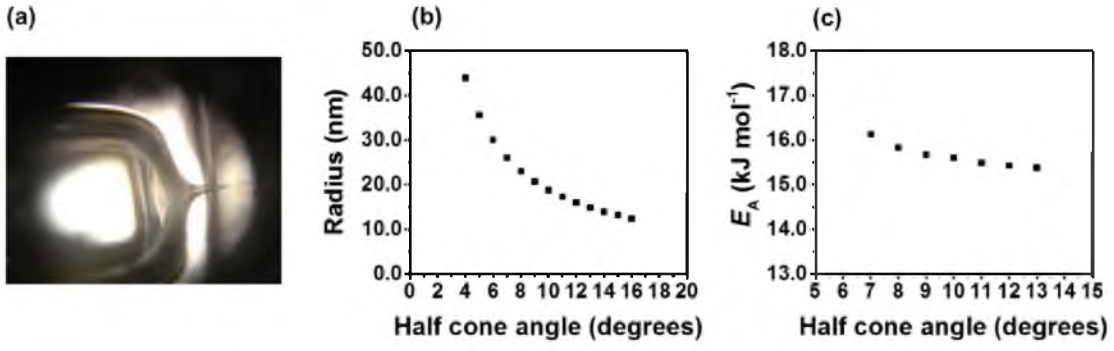

Figure S2.3. (a) An optical microscopy image of the glass nanopore. The image is roughly 40 times enlarged of the actual size (b) radius vs half-cone angle pairs that corresponding to a nanopore with a 9.18 MΩ resistance and (c) the variation in activation energy as a function of half-cone angle in 0.1 mM at 0.35 V.

S2.6.4 Simulated Activation Energies as a Function of Voltage

An equation (-0.0002044 x (T[°C]) -0.010469) for the dependence of the surface charge on temperature was extracted from values reported by Taghipoor et al.[35] to study the effect of temperature on surface charge. Activation energies calculated as a function of voltage assuming surface charge using this relation are shown in Figure S2.4 (b) as a black line. When compared with the red line that represents experimental data for the same conditions (20 nm pore, 0.1 mM KCl), we see the curve is offset considerably (~7 kJ mol^{-1}, at 0 V). A difference in the magnitude of the change in E_A with E is observed as well, although the trend of increasing E_A values with increasing potential is observed.

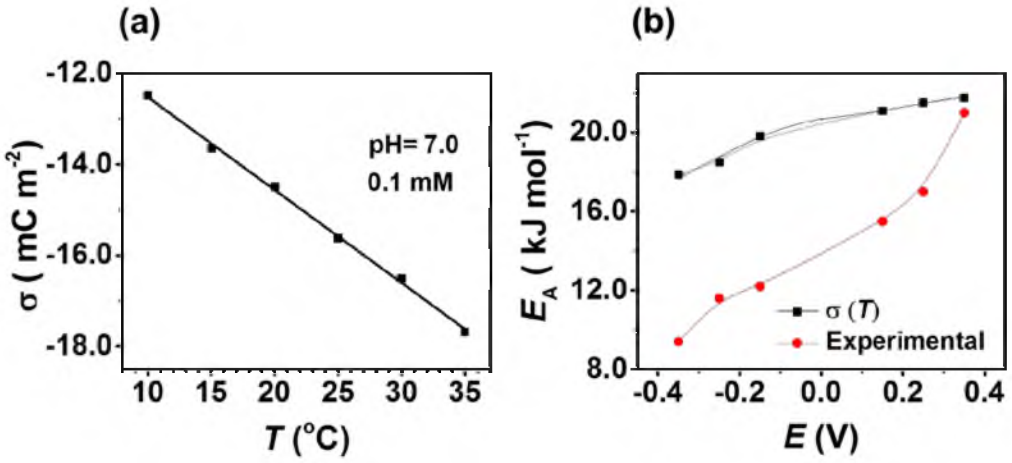

Figure S2.4. (a) The surface charge density as a function of temperature. (b) Simulated activation energies for a 20 nm pore for 0.1 mM KCl as a function of applied potential using temperature dependent surface charge (black line) and experimental data (red line). The Arrhenius plot were linear for the between 10 °C – 35 °C.

S2.6.5 Temperature Dependence of Diffusion Coefficients

Values of the ion diffusion coefficients (D_i) as a function of temperature were estimated using the Stokes-Einstein relationship (2.4)

$$D_i = \frac{k_B T}{6\pi\eta(T) r_i} \tag{2.4}$$

where k_B is the Boltzmann constant, T is absolute temperature, $\eta(T)$ represents the dynamic viscosity of the medium, and r_i is the radius of the ion. Values of $r_{K+} = 1.25 \times 10^{-10}$ m and $r_{Cl-} = 1.21 \times 10^{-10}$ m were used for the radii of K^+ and Cl^-, respectively.[53] Because the dynamic viscosity changes with the temperature, literature values listed (given in Table S2.1) for the viscosity of water were used.[54,55] The dependence of $\eta(T)$ on ion concentration is negligibly small, varying by only 0.8 % between pure water and 500 mM KCl.[54,55]

Table S2.1. The viscosity of water at different temperatures.

***T* / K**	***η(T)* / mPa s**
283	1.3077
288	1.1527
293	1.0227
298	0.9177
303	0.8377
308	0.7827

In the Comsol finite element simulations, the Nernst-Plank equation (Equation 2 in the main text) is written in terms of the ionic mobilities. As the ionic radii of the two species are very similar we choose to assume that they[53] both have the same diffusion coefficients and mobilities (those calculated using the ionic radius for K^+). Values of μ_i as a function of T computed from the corresponding values of D_i ($\mu_i = D_i/RT$) are shown in Figure S2.5. NB: The unit, s mol kg^{-1} (used in Comsol simulations) can be converted to the conventional mobility (units $m^2\ V^{-2}s^{-1}$) by multiplying by Faraday's constant.

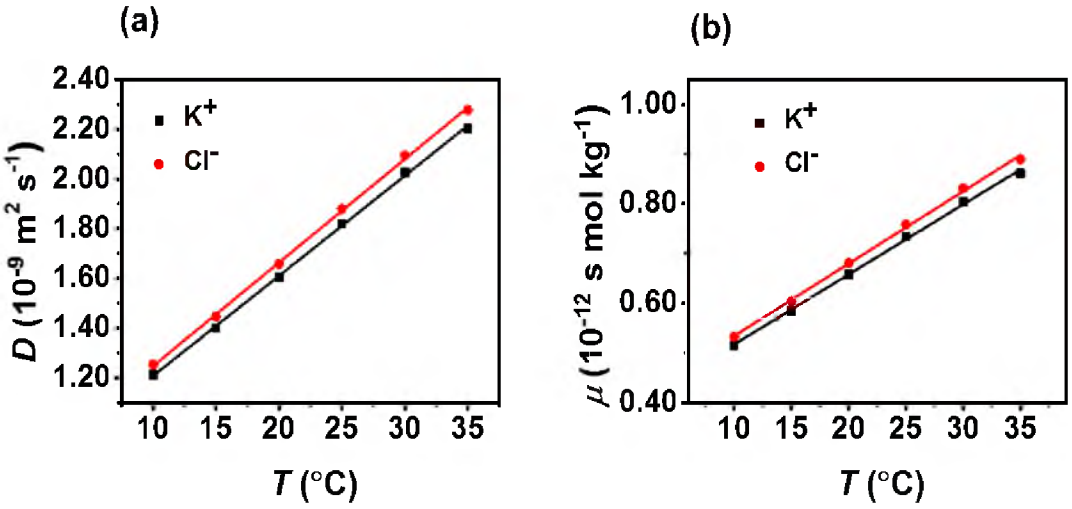

Figure S2.5. (a) Diffusion coefficient as a function of temperature. The expression D = 4.03 x10^{-11} T + 1.02 x 10^{-9} m^2/s (T in °C) for K^+ was used for both K^+ and Cl^- because the diffusion coefficients vary less than 2 %.(b) Ionic mobility is derived from $\mu = D/RT$ (T in K). The expression μ = 1.5 x10^{-14} T+ 3.94 x 10^{-13} s mol kg^{-1} (T in °C) describe the data and was used in the finite element simulations.

S2.6.6 Simulated Arrhenius plots for 35 nm Pore at Different KCl Concentrations

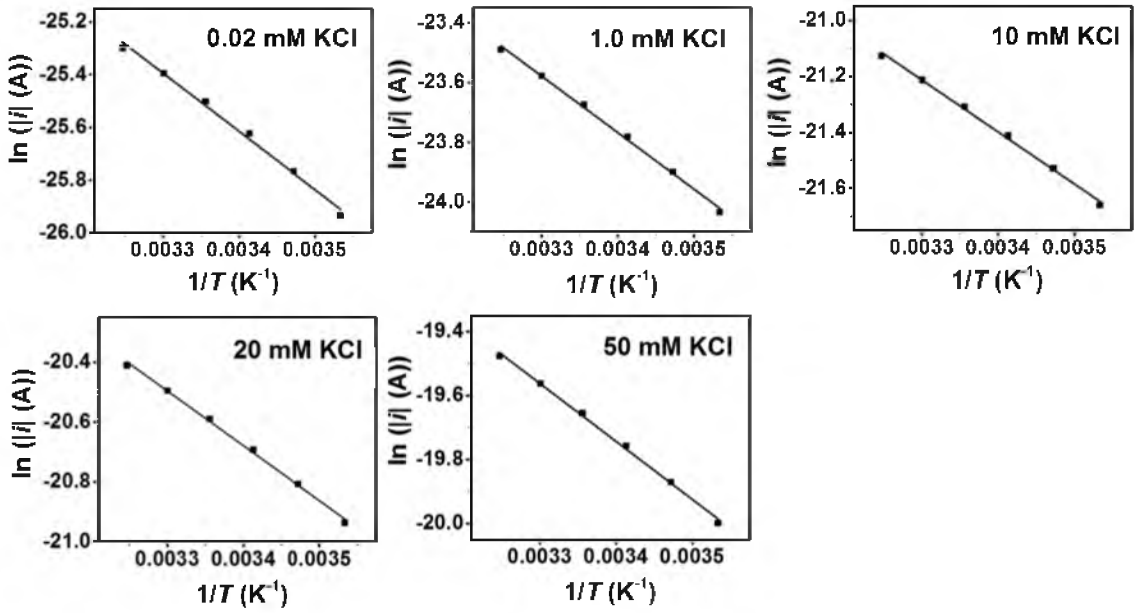

Figure S2.6. Arrhenius plots constructed from the simulated temperature-dependent currents obtained at +0.35 V for a 35 nm pore. These Arrhenius plots were used to extract the activation energy values shown in Figure 2.2 in main text.

S2.6.7 Concentration Distribution of K^+ in Vicinity of the Nanopore Orifice

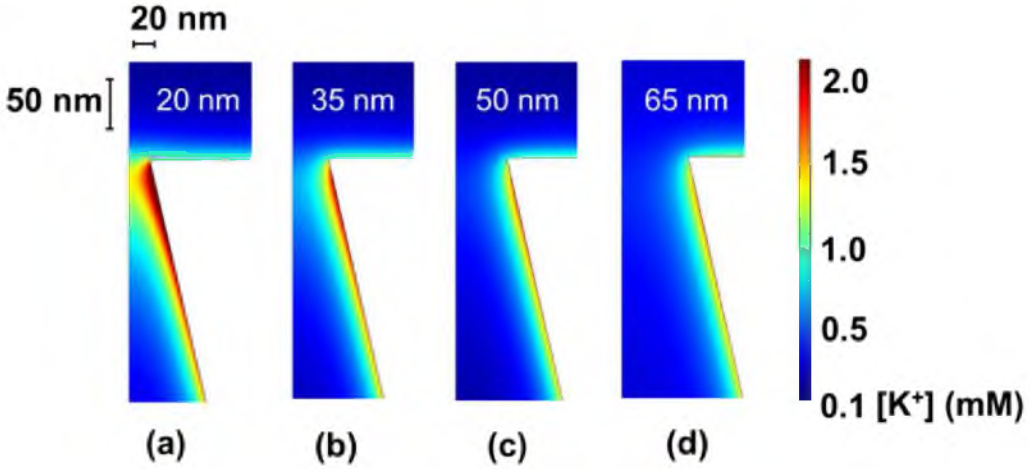

Figure S2.7. Concentration distributions at 25 °C in the vicinity of the orifice of (a) 20 nm (b) 35 nm (c) 50 nm and (d) 65 nm nanopores. The surface charge on the nanopore wall is -2 mC/m^2 and the bulk concentration is 0.1 mM. The applied voltage is +0.35 V.

S2.6.8 Simulated Concentration Profiles of K^+ and Cl^- Along the *z* Axis of a 20 nm Nanopore

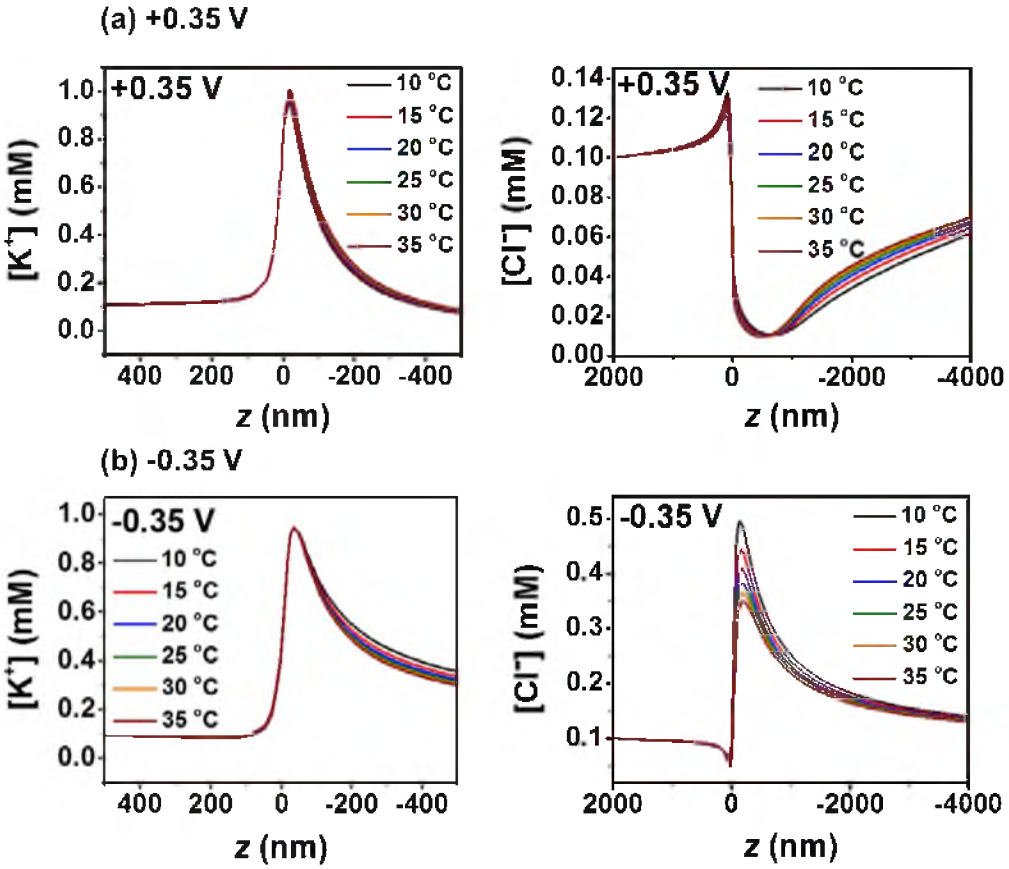

Figure S2.8. Concentration profiles of K^+ and Cl^- in the vicinity of 20 nm nanopore orifice at (a) +0.35 V and (b) -0.35 V. The surface charge on the wall is -2 mC/m^2 and the bulk KCl concentration is 0.1 mM.

S2.6.9 Electric Field Profiles for a 20 nm Pore at Different Temperatures

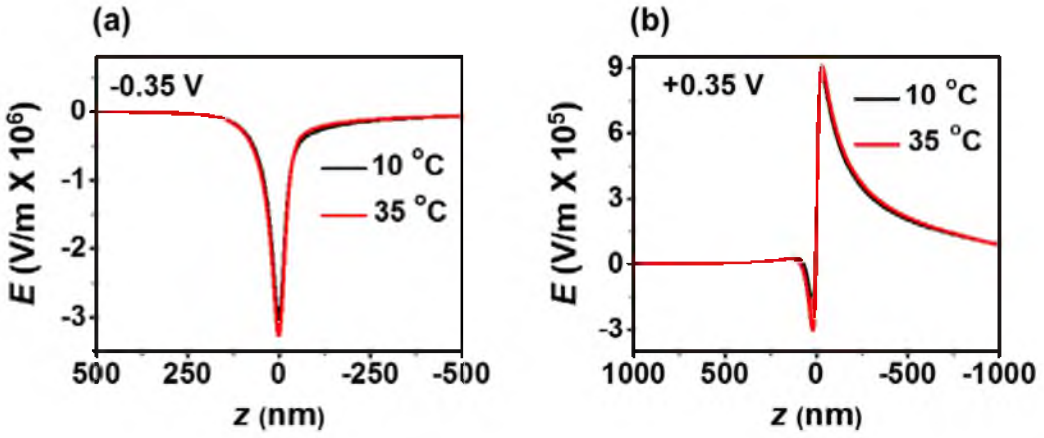

Figure S2.9. The axial component of the electric field inside the pore at z = -20 nm for a 20 nm nanopore (0.1 mM KCl, 10 ℃ and 35 ℃). At (a) -0.35 V and (b) +0.35 V

S2.6.10 Apparent Activation Energies Calculated at Different Applied Voltages

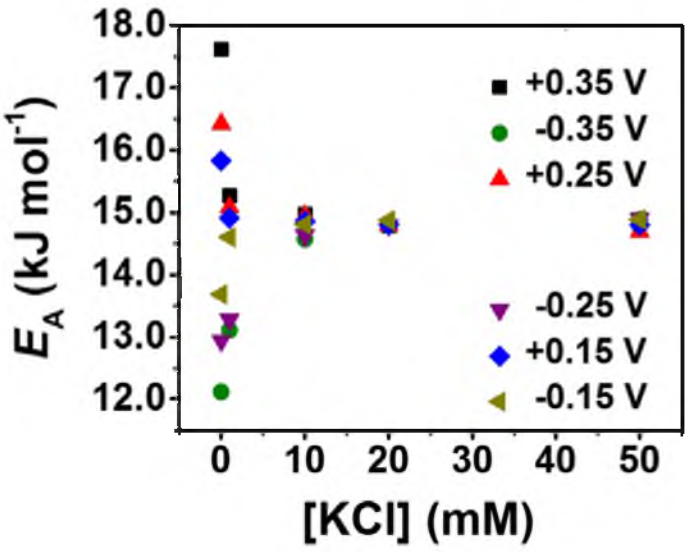

Figure S2.10. Apparent activation energies calculated from finite element simulations at different applied voltages for a 20 nm pore.

CHAPTER 3

DETECTION OF BENZO[A]PYRENE-GUANINE ADDUCTS IN SINGLE-STRANDED DNA USING THE α-HEMOLYSIN NANOPORE

3.1 Introduction

In this chapter, we report that the α-hemolysin (αHL) nanopore platform can be used to detect a BPDE adduct to guanine (G) in synthetic oligodeoxynucleotides. Polycyclic aromatic hydrocarbons (PAHs) emitted into the environment by the incomplete combustion of coal, crude oil, and gasoline were reported to have carcinogenic properties in humans as early as 1876.[1,2] In 1930, the PAH benzo[a]pyrene (BP) was identified as the carcinogen in these substances. Workers in tar distilleries, aluminum production, fossil fuel processing, and road paving are exposed to high levels of BP, as are smokers and consumers of grilled meats.[3-6] Exposure to BP has been shown to increase susceptibility to lung and colon cancers.[7]

Cellular studies have demonstrated that one of the principal pathways through which BP is removed from the body is via cytochrome p450s (CYP450), yielding the final product benzo[a]pyrene diol epoxide (BPDE, Figure 3.1). BPDE exists in four isomeric forms with the (+)-*anti*-7α,8β-dihydroxy-9α,10α-epoxy-7,8,9,10-tetrahydro-benzo[a]pyrene (BPDE) isomer being the predominant one observed from enzymatic studies.[8,9] BPDE is electrophilic and susceptible to nucleophilic attack from DNA, where

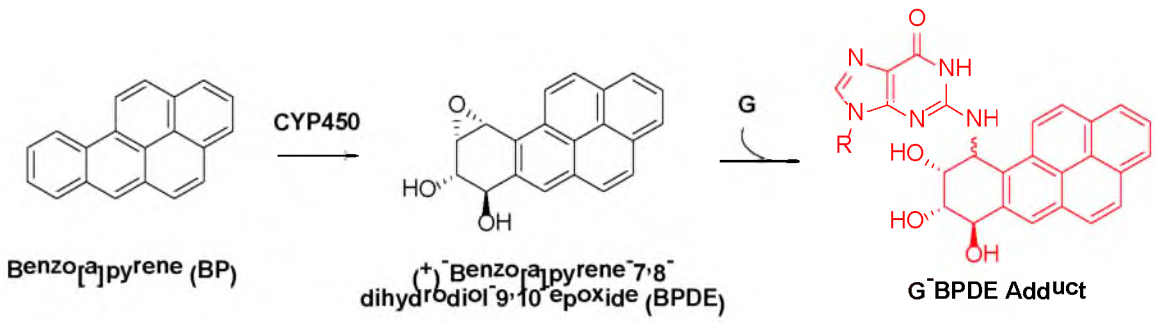

Figure 3.1. Benzo[a]pyrene metabolism leading to guanine adducts in DNA.

the base guanine (G) is a chief site for adduction of BPDE, yielding a stable adduct at the N^2 position (G-BPDE, Figure 3.1). Because the epoxide ring-opening can occur by either S_N1 or S_N2 mechanisms, two diastereomers of G-BPDE are formed (Figure 3.1), leading to different structural perturbations of the DNA double helix. Moreover, mutations at specific G residues in the *TP53* gene are responsible for the mutagenic properties of BPDE that lead to lung cancer.[10-12] Therefore, identification of these adducts and their locations in the genome are critical to addressing an individual's susceptibility to cancers caused by BPDE.

Several methods have been developed for quantification of BPDE adducts in genomes.[13-15] The most commonly used methods include [^{32}P]-postlabeling[16] enzyme-linked immunosorbent assay (ELISA),[16] liquid chromatography coupled to mass spectrometry (LC-MS),[17] capillary electrophoresis MS, or HPLC coupled with a fluorescence detector.[18] Analysis of BPDE adducts in DNA by these methods requires exhaustive nuclease digestion of the DNA sample to the nucleoside monomers. There are two major drawbacks with this step: (1) digestion of these adducts in DNA to the nucleoside monomers is often incomplete because the lesion is not a good substrate for any

nucleases, and (2) digestion of the DNA causes all sequence information to be lost.[19] Methods for quantification of G-BPDE adducts by LC-MS have identified this lesion to exist at a concentration of <10 adducts/10^8 nucleotides in the human genome,[19,20] and a method that can directly analyze these adducts in the genome would be advantageous for quantification of BPDE adducts. In addition, a single-molecule method would have the added advantage of addressing the question of the distribution of adducts and identifying any hotspots for adduct formation. A powerful strategy for analyzing DNA is achieved by electrophoretically driving single-stranded DNA through the α-hemolysin (αHL) nanopore.[21,22] Studies with this nanopore have demonstrated the potential for sequencing the four DNA bases,[23] epigenetic markers,[24] damage to DNA resulting from oxidation[25-27] or deamination,[28,29] photochemical damage,[27] and base release that yields abasic sites.[29,30]

Herein, we demonstrate that the nanopore ion channel method can be applied to the direct detection of a G-BPDE adduct. In these studies, short (4-mer) and long (41-mer) synthetic DNA oligomers with a centrally located BPDE adduct were electrophoretically driven through the αHL nanopore while monitoring the current fluctuations and event times. These studies demonstrate that the BPDE adduct is capable of passing through the pore while producing a current blockage signature characteristic of the biomarker. These observations represent the initial step toward applying the nanopore method for the detection and quantification, and ultimately for reading the sequence, in which BPDE adducts reside in the genome.

3.2. Experimental Section

Caution: All PAHs are potentially carcinogenic and should be handled in accordance with NIH Guidelines for the Use of Chemical Carcinogens.

3.2.1 Chemicals and Materials for Preparation of BPDE-DNA Adduct

All DNA strands were synthesized from commercially available phosphoramidites by the DNA/peptide core facility at the University of Utah. (±)-Benzo[*a*]pyrene-7α,8β-dihydrodiol-9α,10α-epoxide was purchased from MRIGlobal and used as received. All other chemicals were used without further purification.

3.2.2 Preparation of BPDE-DNA Adduct

DNA samples were purified by ion-exchange HPLC prior to their use via the following method: solvent A = 10% CH_3CN, 90% ddH_2O; B = 1 M NaCl in 10% CH_3CN 90% ddH_2O, 25 mM Tris pH 8; flow rate = 1 mL/min while monitoring the absorbance at 260 nm. The method was initiated at 15% B followed by a linear increase to 100% B over 30 min. Synthesis of the BPDE adducted DNA strands were carried out according to a literature protocol.[31] Briefly, the BPDE stock solution was made by dissolving BPDE in 19:1 THF and 1.5% aqueous triethylamine. Reactions were performed in 100-μL aliquots in Eppendorf tubes containing 2 mM DNA and 1 mM BPDE stock solution in 25 mM Tris, 1.5% aqueous triethylamine, 200 mM NaCl all at pH 9.2. The reaction was carried out overnight in the dark at 37 °C. The reaction mixture was neutralized by adding 3 mL of 20 mM PBS buffer (pH 7.5) before purification. Products were purified by ion-exchange HPLC running the same solvent system as reported above and shown in Figure 3.2.

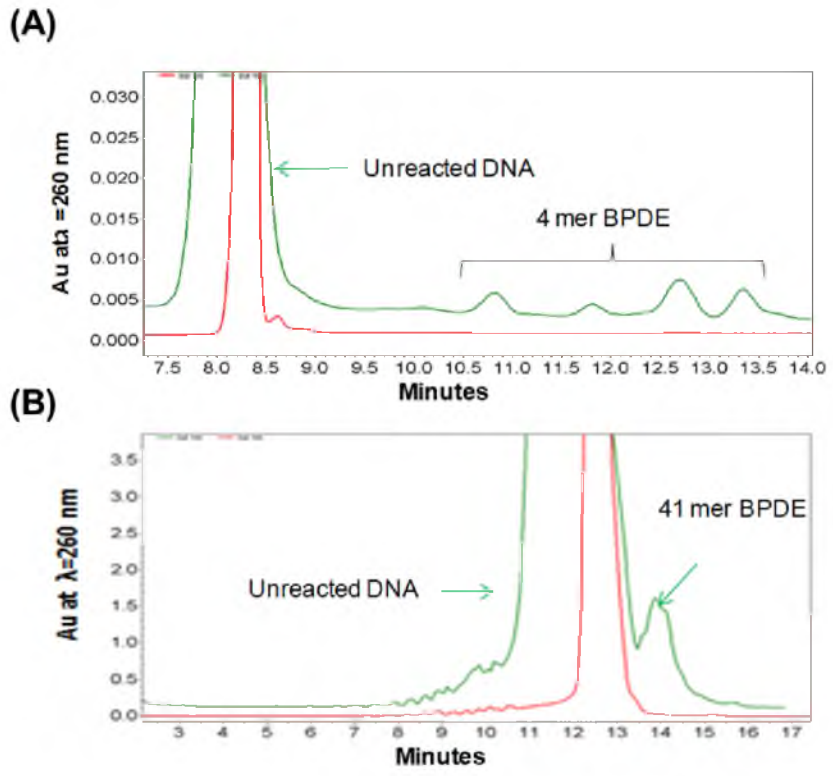

Figure 3.2. Ion-exchange HPLC traces. (A) For 4 mer-BPDE. (B) 41-mer BPDE. Green color traces represent the reaction mixture, whereas red traces represent the standard DNA mixture. The HPLC conditions utilized solvent A = 10% CH_3CN, 90% ddH2O; B = 1 M NaCl in 10% CH_3CN 90% ddH2O, 25 mM Tris pH 8; flow rate = 1 mL/min while monitoring the absorbance at 260 nm. The separation was initiated at 15% B followed by a linear increase to 100% B over 30 min.

All isomeric products were collected together and analyzed by ESI-MS to give the following result: 41-mer BPDE calcd mass = 12136.9, expt mass = 12139.2. Reaction yields were ~5%.

3.2.3. Glass Nanopore Membrane (GNM) and Bilayer Formation for Ion Channel Recording

The method for fabrication of a conical-shaped nanopore in a thin glass capillary membrane has been previously reported.[32] The nanopores used for these studies had an orifice with a 300 to 600 nm radius. Silanization of the glass surface was achieved with 2% (v:v) 3-cyanopropyldimethylchlorosilane in CH_3CN for 6 h at room temperature to introduce a hydrophobic surface to which the lipid bilayer could form. Two Ag/AgCl electrodes were placed in solution on the inside (*trans*) and outside (*cis*) of the capillary. The electrolyte solution was comprised of either 1 M KCl or 3 M NaCl in 10 mM PBS pH 7.4. Current-time (*i-t*) recordings were performed using a custom built high-impedance, and low-noise system (Electronic BioSciences Inc., San Diego, CA). The lipid bilayer was formed with 1,2-diphytanoyl-*sn*-glycero-3-phosphochline across the silanized GNM; bilayer formation was indicated by a resistance increase from ~10 MΩ to ~100 GΩ. A gas-tight syringe was used to apply a pressure of 20-40 mmHg to the inside of the GNM capillary that facilitated protein insertion into the lipid bilayer.[33] Wild type αHL was reconstituted from the monomer peptide added to the *cis* side of the GNM (0.2 μL of a 1 mg/mL solution). Formation of a properly functioning nanopore was determined by an I_o at 120 mV of 122 pA or 244 pA at 25 °C in 1 M KCl or 3 M NaCl, respectively. Ion channel measurements were performed at 120, 140, 160, and 180 mV (*trans* versus *cis*), while

recording the data with a 100 kHz low-pass filter and at a 500 kHz data acquisition rate. All experiments were performed at 25.0 ± 0.5 °C.

3.2.4 Data Analysis

Events were extracted using QUB 2.0.0.29 and data were analyzed using OriginPro 9.1 and software donated by Electronic BioSciences Inc. (San Diego, CA). The *i-t* traces presented were refiltered to 50 kHz for presentation purposes unless stated otherwise.

3.3 Results and Discussion

3.3.1. Ion Channel Measurements

Two DNA oligomers were chosen for study, a 4-mer and a 41-mer, with the sequences 5'-CCGC-3' and 5'-C_{20}-G-C_{20}-3', respectively. These oligomers were allowed to react with (±)-benzo[*a*]pyrene-7α,8β-dihydrodiol-9α,10α-epoxide following a literature protocol to yield an adduct at G.[31] The presence of a single G ensured that only one adduct was formed per strand; hereafter, the adducted oligomers are referred to as 4-mer BPDE and 41-mer BPDE. A single αHL ion channel was inserted into a lipid bilayer spanning a glass nanopore membrane. [34] The DNA analyte was added to the *cis* side of the channel in a buffered (25 mM PBS, pH 7.4) 1 M KCl or 3 M NaCl solution. A voltage was applied to electrophoretically drive the DNA from the *cis* to *trans* side of αHL, while monitoring the ion current as a function of time.

3.3.2. Translocation of 4-mer BPDE Adduct

Previous studies conducted in our laboratories have monitored translocation of DNA strands modified by a broad range of molecular adducts through the nanopore.[29,30] In these studies, some adducts were found to be too large to translocate through the central constriction of αHL (1.4 nm in diameter).[29,35] Due to the size and hydrophobic nature of the BPDE adduct, a short 4-mer BPDE strand was chosen for our initial experiments to determine if the adduct was too large to pass through the narrow constriction zone. The short modified strand was advantageous because of its ease of synthesis and characterization (Figure 3.2A), and this simplified study provided the basis for understanding how the BPDE adduct interacts with the αHL channel.

A comparison of ion current versus time (*i-t*) recordings for the unmodified 4-mer and the 4-mer BPDE DNA oligomers recorded at 180 mV (*trans* versus. *cis*) in 1 M KCl solution is shown in Figure 3.3. Based on previous studies, the anticipated residence time for the C-rich 4-mer strand in the αHL nanopore is predicted to be ~4-8 μs, and events of >50% blockage to the current in this time range were measured.[36] Translocation of the 4-mer BPDE oligomer resulted in longer (>10 μs) events and exhibited unique current patterns that were not observed for the unmodified 4-mer strand (Figure 3.3B). All events initiated with a decrease in the open channel current (Figure 3.3B, I_o) to a mid-level current blockage (I_A) that was centered at ~10% I_o and lasted 10-200 μs. Next, the events progressed to a noisy deep-level current blockage (I_B) that was centered at ~75 % I_o and lasted from 10 to 100 μs (Figure 3.3B). All events returned to I_o (Figure 3.3B) without the appearance of another midlevel current suggesting the oligomer moved through the β-barrel and exited the *trans* side of the pore. [37]

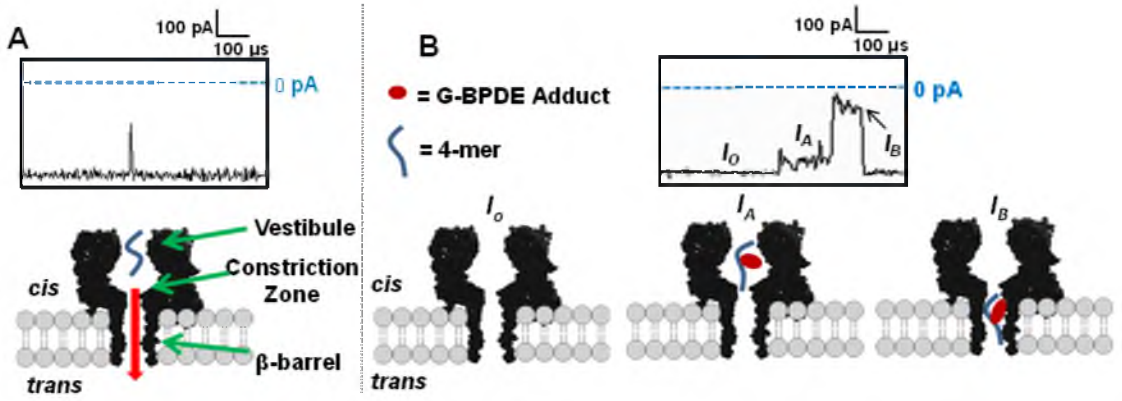

Figure 3.3. Proposed model for translocation of a 4-mer and 4-mer BPDE adduct through the αHL nanopore. (A) Representative *i-t* trace for the 4-mer (5'-CCGC-3') strand, (B) representative *i-t* trace for a 4-mer BPDE adducted oligomer. All data were recorded at 180 mV (*trans* versus *cis*) in 1 M KCl at 25.0 ± 0.5 °C with a 100 kHz low-pass filter and 500 kHz data acquisition rate.

Based on the *i-t* traces above, we propose the following model to describe how the 4-mer BPDE strand translocates through the αHL pore. The initial midlevel current, I_A, is established when the 4-mer BPDE strand enters the vestibule of αHL from the *cis* side (Figure 3.3B, I_A).Next, the BPDE strand enters the β-barrel and the current drops to a deep blockage level (Figure 3.3B, I_B), during which the 4-mer BPDE strand is driven through the narrow β-barrel (d ~1.4 nm) to the *trans* side of αHL. The sharp return to I_o, and not back to the mid-level current I_A indicates that the 4-mer BPDE exited the *trans* side of the channel and does not return through the *cis* opening, because exit from the *cis* opening would give a second mid-level current (I_A). This promising result suggests that BPDE adducts can be detected in longer oligomer model systems that would occupy the full length of the channel while the adduct interacts with the protein walls.

3.3.3. Translocation of 41-mer BPDE Adduct

In the second study, a 41-mer poly-2'-deoxycytidine (poly-C) strand with a centrally located G was synthesized and allowed to react with BPDE to give an adduct yield of ~5%. After HPLC purification, reinjection of the adduct sample established that it contained 30% unreacted DNA. Therefore, when analyzing the 41-mer translocation data, events shorter than 50 μs were attributed to unreacted starting material (t_{max} = 44 μs at 120 mV) and discarded. Analysis of the 41-mer strand with a BPDE adduct (2 μM) was conducted in buffered solutions (25 mM PBS, pH 7.4) containing 1 M KCl and 3 M NaCl. Typical *i-t* translocation events that are characteristic of the unique pattern observed for the DNA-BPDE adduct in 1 M KCl electrolyte are shown in Figure 3.4, and data collected in 3 M NaCl are presented in Figure S3.3. The time traces for unmodified 41-mer strands are presented in Figure S3.1 and S3.2

3.3.4. Deep Blockage Level Analysis

Translocation events for the 41-mer BPDE are initiated when the open channel current is reduced to a shallow shoulder level (I_1) that has a $\%(I_1/I_o)$ = 55 ± 5% (Figure 3.5). The entry of either the 3' or 5' end of the strand into the vestibule leads to varying lengths of the tail in the vestibule resulting in a shallow and broad distribution in current levels. Currents of this magnitude were previously described to result from partial entry of the DNA strand into the channel,[38] similar to our results. Next, the event transitions to a deep level blockage current with values of I_2 measured as 18 ± 2% and 21 ± 2% (Figure 3.5B and C). Based on previous studies of poly-C translocation, these two current distributions represent the entry directionally (5' or 3') into the β-barrel.[37,39] Current histograms for the I_2 currents can be deconvoluted into two pseudo-Gaussian distributions

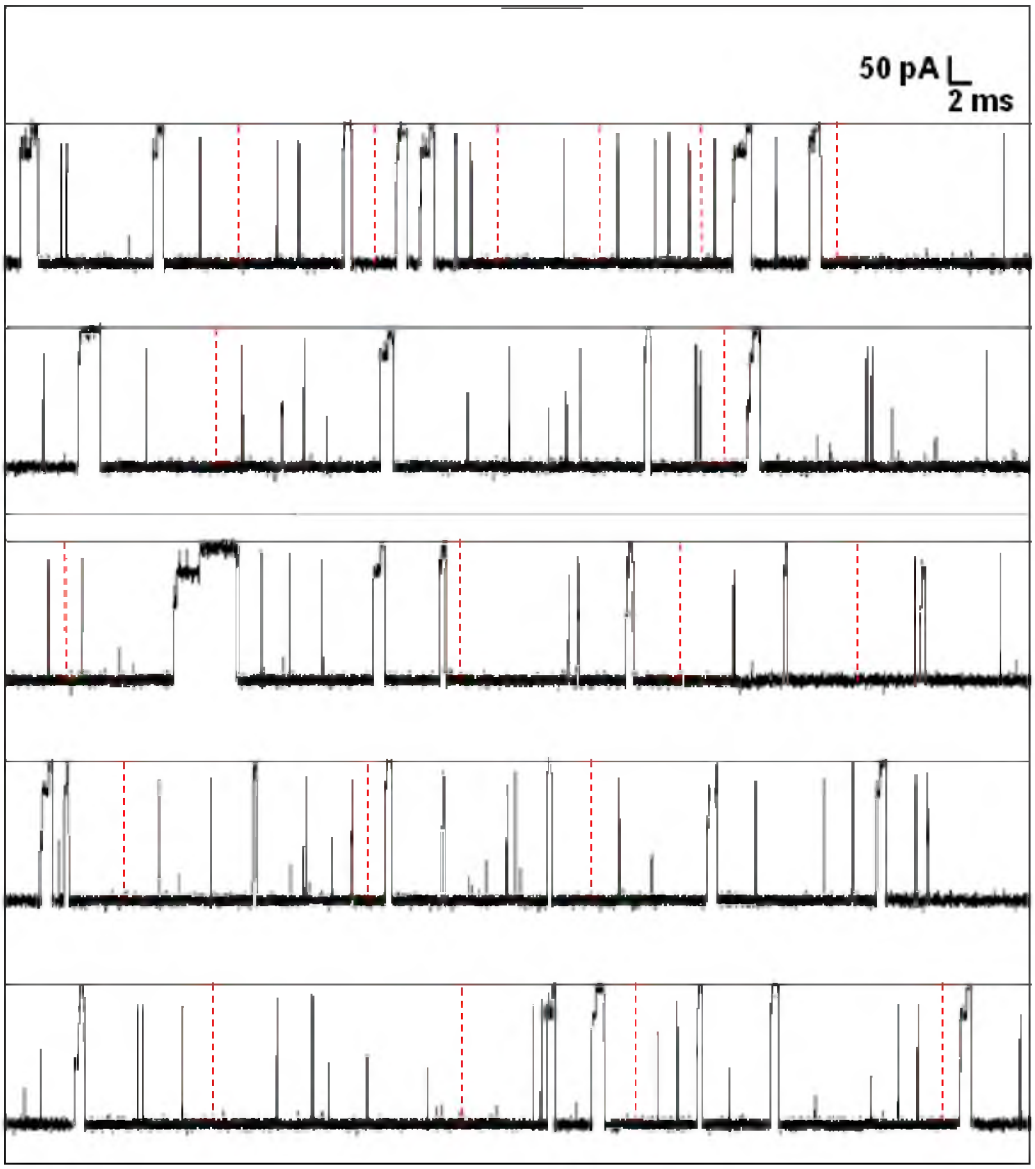

Figure 3.4. Current versus. time profile collected over 20 s for 41-mer BPDE (2 μM) in 1 M KCl. The data were recorded at 180 mV (*trans* versus. *cis*) at 25.0 ± 0.5 °C. The red dotted lines indicate the places where long open channel blockages were removed.

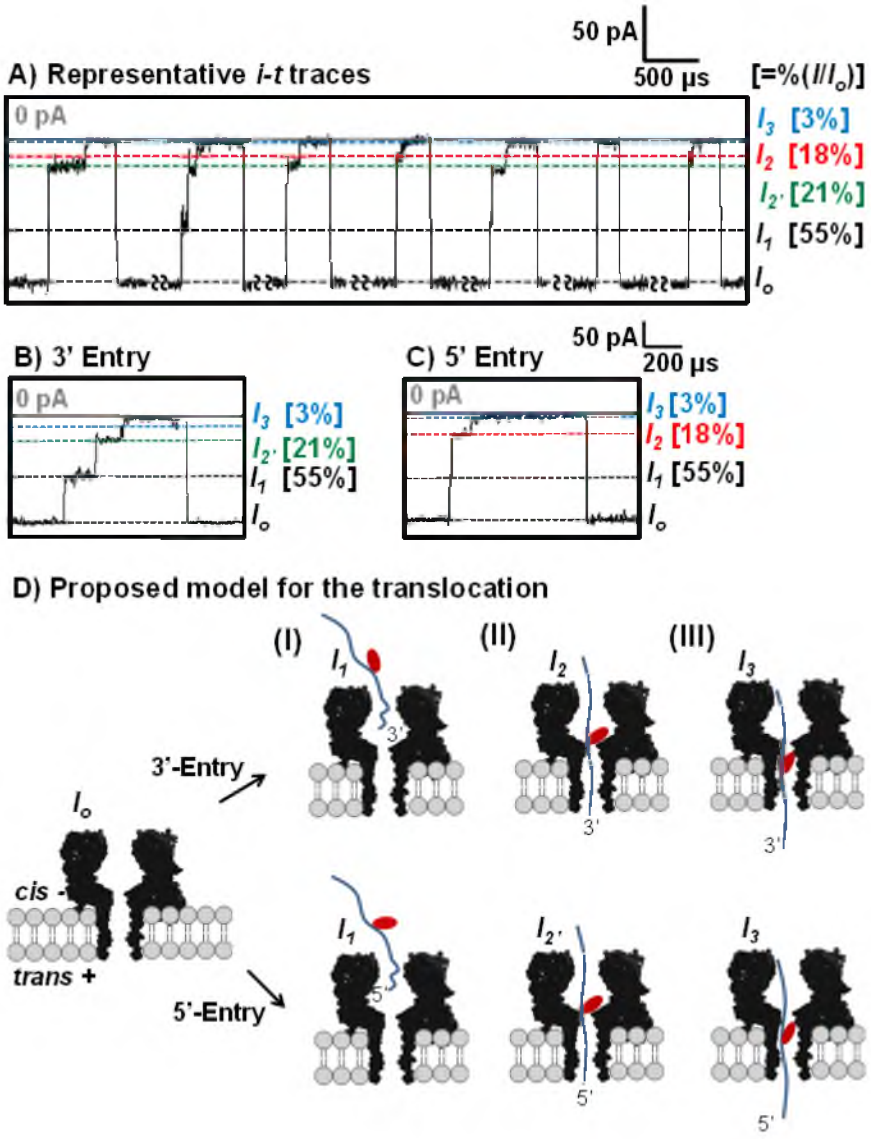

Figure 3.5. Event types detected during translocation of the 41-mer BPDE sample. (A) Representative *i-t* traces for translocation of the 41-mer BPDE sample, (B) blowup of a 3'-entry event, and (C) blowup of a 5'-entry event. The data were recorded at 180 mV (*trans* versus *cis*) at 25.0 ± 0.5 °C. The data were refiltered to 50 kHz. Results from measurements are presented as percent ratio of the blockage current versus open channel current %(I/I_o). The *i–t* traces for events >50 µs were analyzed. Long open channel current segments (20 - 500 ms) were manually removed, as indicated on the *i-t* trace. A relatively low capture rate (~70 events/s) was observed due to the low concentration (2 µM) of the 41-mer BPDE studied. (D) Proposed model for the translocation of a 41-mer BPDE adduct through αHL. (I) DNA enters from the *cis* side of the channel by threading either the 3' or 5' tail. (II) The BPDE adduct becomes caught at the 1.4 nm central constriction that gives rise to the deep blockage in the ion current recorded that marks the presence of the BPDE adduct. (III)The DNA translocates through the β-barrel.

that are centered at the currents for 5' and 3' entry (Figure 3.6). In these studies, the 3' events with lower residual current dominate at lower voltage, and as the voltage is increased, the higher residual current events corresponding to 5' entry increased.

We propose that the $\%(I_2/I_o)$ current represents the bulky BPDE adduct being captured at the central constriction of αHL (Figure 3.5D), The adduct strand then remains caught in this position until a conformation feasible for overcoming the energy barrier and entering into the β-barrel is found. After the strand progresses through the β-barrel the current returns to the open channel value.

Events then advance to a final current level, I_3, in which nearly all of the ion flux is attenuated ($\%(I_3/I_o) = \sim 3\%$). After the exit of the BPDE adduct, the ion flow returns to the open-channel current indicating translocation because exit through the *cis* opening would mirror the entry current pattern with a midlevel current blockage. This observation, along with the inverse correlation of time with increased voltage (Table 3.1), supports the hypothesis that the 41-mer BPDE adduct translocates through αHL.

The observed current blocking is consistent with the adduct causing a steric restriction to the movement of the strand through the pore that nearly blocks the ion flux. The distribution in the event time can be modeled by an exponential decay time distribution (see Figure S3.4) with a time constant τ for steps 2 and 3. These events were consistently longer (780 μs at 120 mV and 555 μs at 180 mV) than those observed for the standard (44 μs at 120 mV and 18 μs at 180 mV), suggesting that bulky BPDE adducts significantly slows translocation of the DNA strand through αHL (Table 3.1).

Interestingly, 3'-entry and 5'-entry events both give the characteristic ion current, I_3, for the BPDE adduct (Figure 3.5B and C).

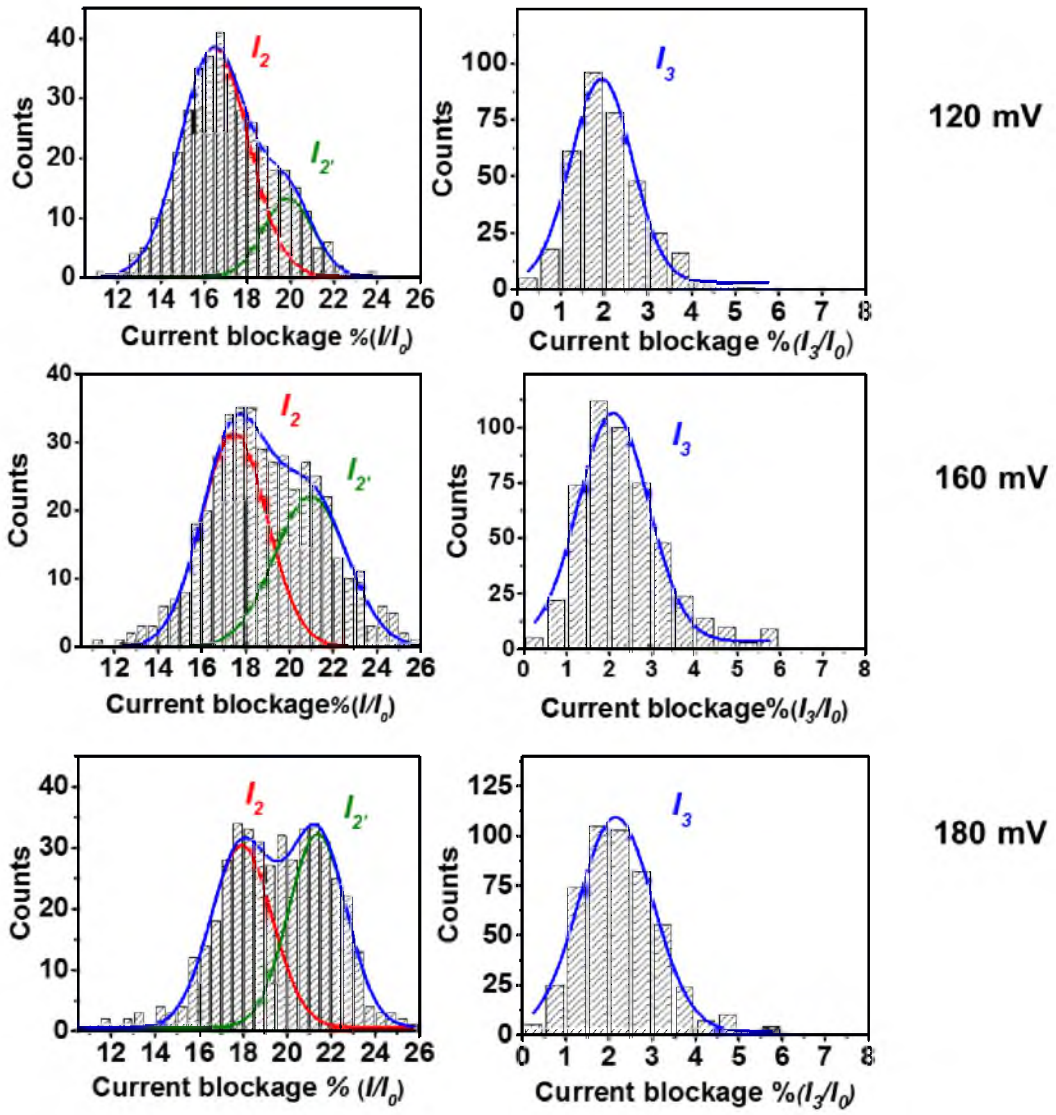

Figure 3.6. Current histograms for the step-current levels monitored for the 41-mer BPDE events. (A) Plots of frequency distributions for the I_2 and $I_{2'}$ current levels. (B) Plots of frequency distributions for the I_3 current levels. The data were collected at 120, 160, and 180 mV (*trans* versus. *cis*) in 1 M KCl at 25.0 ± 0.5 °C and plotted with a bin size of 0.5 pA. Population distributions represent 400-450 events.

Table 3.1. Time constants measured for the 41-mer standard and 41-mer BPDE strand versus voltage.

Voltage (mV)[a]	**41-mer BPDE 5' & 3' Events** τ **(μs)**[b]	**41-mer Standard** t_{max} **(μs)**[c]
120 mV	780 ± 15	44.1 ± 0.5
160 mV	640 ± 20	21.0 ± 0.5
180 mV	555 ± 15	18.5 ± 0.8

[a] Voltage was measured *trans* versus. *cis* at 25 °C.
[b] The time constant was determined by fitting the frequency versus time histogram to a single-exponential decay function.
[c] The reported time constant was determined by fitting the frequency versus time histogram to a Gaussian function (see Appendix B.4).

In previous studies from our laboratories, an 18-crown-6 adduct also gave a characteristic low residual current (6-7%)[29] however, these adducts were only detectable upon 5'-entry of the strand. In contrast, the BPDE adduct yields the current signature upon both 3' and 5' entry, which most likely occurs because of the larger size and rigidity of this adduct. Detection of BPDE adducts from both 3' and 5' entry will be very advantageous for its detection by the αHL nanopore.

3.4. Conclusions

In the current work, we set out to determine if BPDE adducts to G in DNA could be detected using the wild-type αHL nanopore. We demonstrate that a 41-mer DNA strand translocates through αHL and yields a characteristic three-step ion-current signature. We anticipate that the approach we outline here will be useful in the study of other lesions

created by the adduction of polycyclic organic compounds, such as aflatoxin[40] and ochratoxin.[41] We anticipate that this result will provide the groundwork for future studies that aim to detect, quantify, and eventually sequence this lesion from cellular DNA sources.

3.5. Reference

(1) Toyooka, T.; Ibuki, Y. *Environ. Toxicol. Pharmacol.* **2007**, *23*, 256.

(2) Baird, W. M.; Hooven, L. A.; Mahadevan, B. *Environ. Mol. Mutagen.* **2005**, *45*, 106.

(3) Phillips, D. H. *Nature* **1983**, *303*, 468.

(4) Boffetta, P.; Jourenkova, N.; Gustavsson, P. *Cancer Causes Control* **1997**, *8*, 444.

(5) Brookes, P.; Lawley, P. D. *Nature* **1964**, *202*, 781.

(6) Armstrong, B.; Hutchinson, E.; Unwin, J.; Fletcher, T. *Environ. Health Perspect.* **2004**, *112*, 970.

(7) Mastrangelo, G.; Fadda, E.; Marzia, V. *Environ. Health Perspect.* **1996**, *104*, 1166.

(8) Kapitulnik, J.; Wislocki, P. G.; Levin, W.; Yagi, H.; Jerina, D. M.; Conney, A. H. *Cancer Res.* **1978**, *38*, 354.

(9) Yang, S. K.; McCourt, D. W.; Roller, P. P.; Gelboin, H. V. *Proc. Natl. Acad. Sci.* **1976**, *73*, 2594.

(10) Pfeifer, G. P.; Besaratinia, A. *Hum. Genet.* **2009**, *125*, 493.

(11) Denissenko, M. F.; Pao, A.; Tang, M.; Pfeifer, G. P. *Science* **1996**, *274*, 430.

(12) Jiang, H.; Shen, Y.-M.; Quinn, A. M.; Penning, T. M. *Chem. Res. Toxicol.* **2005**, *18*, 365.

(13) Azbal, C. C.; Skipper, P. L.; Yu, M. C.; London, S. J.; Dasari, R. R.; Tannenbaum, S. R. *Cancer Epidemiol. Biomarkers Prev.* **2000**, *9*, 733.

(14) Godschalk, R. W.; Van Schooten, F. J.; Bartsch, H. *J. Biochem. Mol. Biol.* **2003**, *36*, 1.

(15) Manchester, D. K.; Weston, A.; Choi, J. S.; Trivers, G. E.; Fennessey, P. V.; Quintana, E.; Farmer, P. B.; Mann, D. L.; Harris, C. C. *Proc. Natl. Acad. Sci. U. S. A.* **1988**, *85*, 9243.

(16) Gelboin, H. V. *Physiol. Rev.* **1980**, *60*, 1107.

(17) Chen, Y. L.; Wang, C. J.; Wu, K. Y. *Rapid Commun. Mass Spectrom.* **2005**, *19*, 893.

(18) Gennaro, L. A.; Vadhanam, M.; Gupta, R. C.; Vouros, P. *Rapid Commun. Mass Spectrom.* **2004**, *18*, 1541.

(19) Tretyakova, N.; Villalta, P. W.; Kotapati, S. *Chem. Rev.* **2013**, *113*, 2395.

(20) Singh, R.; Gaskell, M.; Le Pla, R. C.; Kaur, B.; Azim-Araghi, A.; Roach, J.; Koukouves, G.; Souliotis, V. L.; Kyrtopoulos, S. A.; Farmer, P. B. *Chem. Res. Toxicol.* **2006**, *19*, 868.

(21) Branton, D.; Deamer, D. W.; Marziali, A.; Bayley, H.; Benner, S. A.; Butler, T.; Di Ventra, M.; Garaj, S.; Hibbs, A.; Huang, X.; Jovanovich, S. B.; Krstic, P. S.; Lindsay, S.; Ling, S. L.; Mastrangelo, C. H.; Meller, A.; Oliver, J. S.; Pershin, Y. V.; Ramsey, J. M.; Riehn, R.; Soni, G. V.; Tabard-Cossa, V.; Wanunu, M.; Wiggin, M.; Schloss, J. S. *Nat. Biotechnol.* **2008**, *26*, 1146.

(22) Stoloff, D. H.; Wanunu, M. *Curr. Opin. Biotechnol.* **2013**, *24*, 699.

(23) Stoddart, D.; Heron, A.; Mikhailova, E.; Maglia, G.; Bayley, H. *Proc. Natl. Acad. Sci. U. S. A.* **2009**, *106*, 7702.

(24) Wallace, E. V. B.; Stoddart, D.; Heron, A. J.; Mikhailova, E.; Maglia, G.; Donohoe, T. J.; Bayley, H. *Chem. Commun.* **2010**, *46*, 8195.

(25) Wolna, A. H.; Fleming, A. M.; Burrows, C. J. *J. Phys. Org. Chem.* **2014**, *27*, 247.

(26) Schibel, A. E.; An, N.; Jin, Q.; Fleming, A. M.; Burrows, C. J.; White, H. S. *J. Am. Chem. Soc.* **2010**, *132*, 17992.

(27) Wolna, A. H.; Fleming, A. M.; An, N.; He, L.; White, H. S.; Burrows, C. J. *Isr. J. Chem.* **2013**, *53*, 417.

(28) Jin, Q.; Fleming, A. M.; Johnson, R. P.; Ding, Y.; Burrows, C. J.; White, H. S. *J. Am. Chem. Soc.* **2013**, *135*, 19347.

(29) An, N.; Fleming, A. M.; White, H. S.; Burrows, C. J. *Proc. Natl. Acad. Sci. U. S. A.* **2012**, *109*, 11504.

(30) An, N.; White, H. S.; Burrows, C. J. *Chem. Commun.* **2012**, *48*, 11410.

(31) Pirogov, N.; Shafirovich, V.; Kolbanovskiy, A.; Solntsev, K.; Courtney, S. A.; Amin, S.; Geacintov, N. E. *Chem. Res. Toxicol.* **1998**, *11*, 381.

(32) Zhang, B.; Galusha, J.; Shiozawa, P.; Wang, G.; Bergren, A.; Jones, R.; White, R.; Ervin, E.; Cauley, C.; White, H. *Anal. Chem.* **2007**, *79*, 4778.

(33) Schibel, A. E. P.; Heider, E. C.; Harris, J. M.; White, H. S. *J. Am. Chem. Soc.* **2011**, *133*, 7810.

(34) White, R. J.; Ervin, E. N.; Yang, T.; Chen, X.; Daniel, S.; Cremer, P. S.; White, H. S. *J. Am. Chem. Soc.* **2007**, *129*, 11766.

(35) Song, L.; Hobaugh, M.; Shustak, C.; Cheley, S.; Bayley, H.; Gouaux, J. *Science* **1996**, *274*, 1859.

(36) Kawano, R.; Schibel, A.; Cauley, C.; White, H. *Langmuir* **2009**, *25*, 1233.

(37) Butler, T. Z.; Gundlach, J. H.; Troll, M. A. *Biophys. J.* **2006**, *90*, 190.

(38) Akeson, M.; Branton, D.; Kasianowicz, J. J.; Brandin, E.; Deamer, D. W. *Biophys. J.* **1999**, *77*, 3227.

(39) An, N.; Fleming, A. M.; White, H. S.; Burrows, C. J. *Proc. Natl. Acad. Sci. U. S. A.* **2012**, *109*, 11504.

(40) Akman, S. A.; Adams, M.; Case, D.; Park, G.; Manderville, R. A. *Toxins* **2012**, *4*, 267.

(41) Kensler, T. W.; Roebuck, B. D.; Wogan, G. N.; Groopman, J. D. *Toxicol. Sci.* **2011**, *120*, S28.

S3.6 Supplemental Material

S3.6.1 Sample *i-t* Trace for the Unmodified 41-mer in 1 M NaCl.

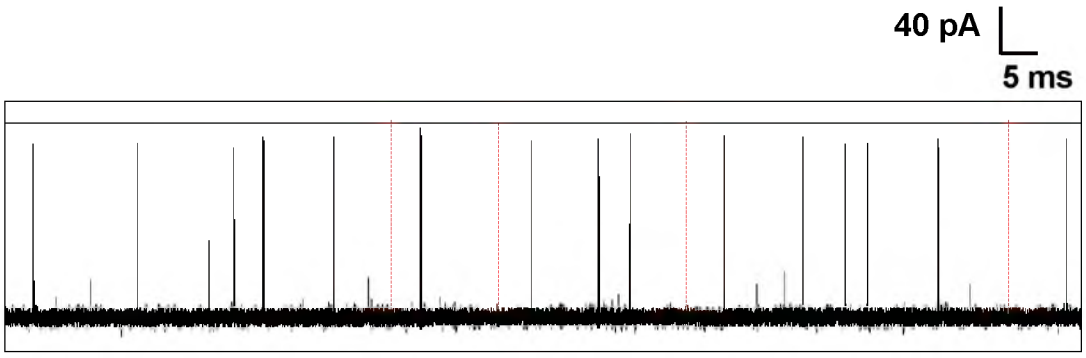

Figure S3.1. Current versus. time profile for the 41-mer standard (4 μM) in 1 M KCl. The data were recorded at 180 mV (*trans* versus *cis*) at 25.0 ± 0.5 °C. Open channel baseline current intervals longer than 20 ms were removed from the following *i–t* traces and indicated by the red dashed lines.

S3.6.2 Sample *i-t* Trace for the Unmodified 41-mer in 3 M NaCl.

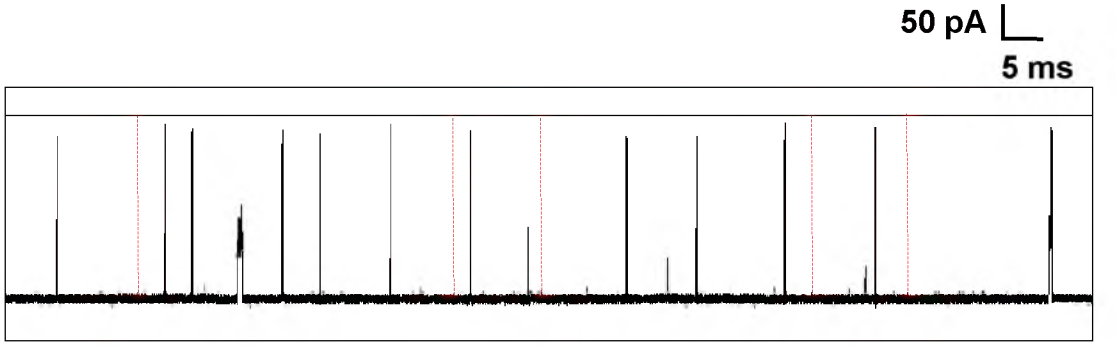

Figure S3.2. (A) Current versus time traces collected over 20 s for the 41-mer standard (4 μM) in 3 M NaCl. The data were recorded at 180 mV (*trans* versus. *cis*) at 25.0 ± 0.5 °C.

S3.6.3 Sample *i-t* Trace for the modified 41-BPDE Adduct in 3 M NaCl.

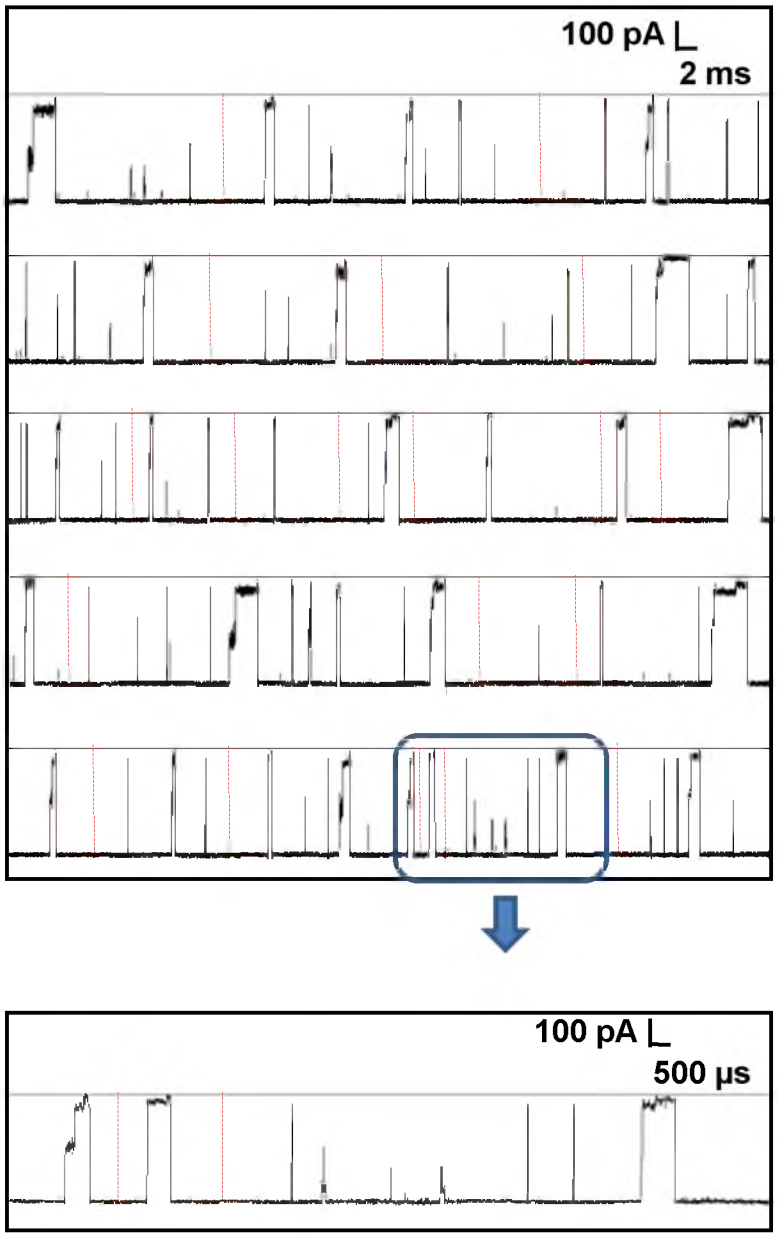

Figure S3.3. Current versus time profile for the 41-mer BPDE (2 µM) in 3 M NaCl. The data were recorded at 180 mV (*trans* versus *cis*) at 25.0 ± 0.5 °C.

S3.6.4 Translocation Analysis of the 41-mer and 41-mer BPDE in 1 M KCl and 3 M

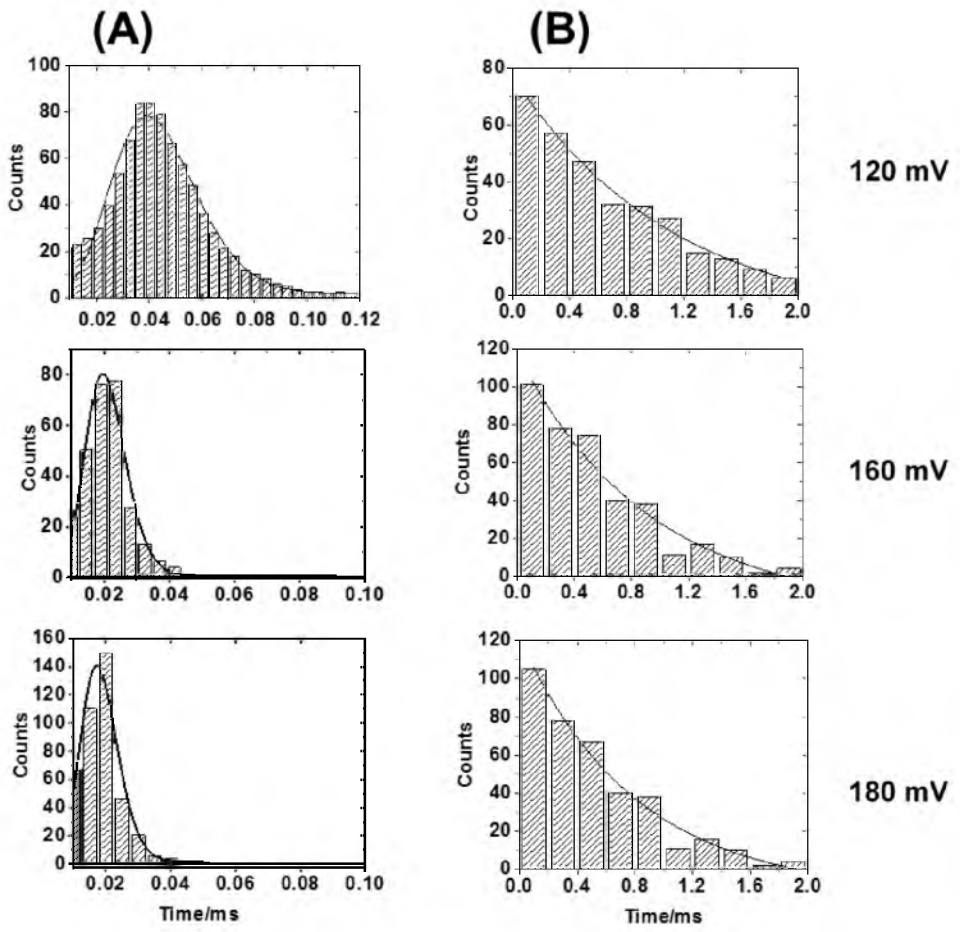

Figure S3.4. Translocation time analysis of the 41-mer and 41-mer BPDE in 1 M KCl. Only the events longer than 70 μs were used for translocation analysis of 41-BPDE. The data were recorded at 120,160, and 180 mV (*trans* versus *cis*) at 25.0 ± 0.5 °C. The time distribution for translocation of 41-mer was fit with a Gaussian model. The modified 41-mer BPDE showed longer translocation times (325-375 events were analyzed), and its duration histogram exhibits an exponential decay.

CHAPTER 4

SIZE-DEPENDENT UNZIPPING OF DUPLEXS OF A-FORM DNA-RNA, A-FORM DNA-PNA, AND B-FORM DNA-DNA IN THE ALPHA-HEMOLYSIN NANOPORE

4.1 Introduction

This chapter presents comparative studies on A-form DNA-RNA duplexes and B-form DNA-DNA duplexes with a single-stranded tail identified significant differences in the blockage current and in the unzipping duration between the two helical forms. The results show that the B-form duplex blocks the channel ~2 pA more and unzips ~15-times slower than an A-form duplex at 120 mV. A model is developed to describe the dependence of duplex unzipping on structure. Nanopores have found broad utility in a number of sensing applications.[1-7] Protein-based nanopores harness the reproducibility of biological systems to furnish well-defined channels, some of which have high-resolution crystal structures to aid in understanding their properties.[8,9] The most well studied is the alpha-hemolysin (αHL) nanopore that has been applied to detect small molecules,[10-13] proteins,[14,15] carbohydrates,[16] RNA,[17-19] and predominantly DNA.[20-22] Further, this protein channel also provides an excellent system for monitoring reactions[17,23] and conducting biophysical experiments to interrogate DNA secondary structures in solution.[24-27] The size of the central constriction (d = 1.4 nm) allows single-stranded DNA (d = 1.0 nm) to pass through

the β-barrel but not double-stranded (ds) DNA.[13,28] However, at higher voltages, the electric field along the pore is sufficient to unzip the duplex into single strands. After the first experimental demonstration of DNA unzipping by Sauer-Budge et al.,[29] many studies have focused on utilizing duplex unzipping to detect metal ion binding,[30] micro-RNA,[31-33] and base mismatches.[29,34,35]

Recently, our laboratory demonstrated that the latch zone of αHL can be used to differentiate a C•G base pair from an abasic site opposite G in duplex DNA when the duplex is temporarily immobilized in the channel.[23,36] Immobilization is achieved through a single-stranded tail appended to one partner of the duplex to thread the molecules in to the channel. These latch zone monitoring capabilities have been potentially optimized by adjusting electrolyte concentration, cation identity, and the temperature.[37,38]

The ~2.6 nm interior diameter of the latch acts to allow smaller molecules to enter the vestibule and larger ones to remain outside when electrophoretically driven to the channel.[13] Examples of this feature are the ability of single-stranded DNA or RNA,[17,18], blunt-ended hairpins,[39,40] fishhook hairpins,[41] DNA-DNA duplexes (B-form duplexes),[29] small G-quadruplexes,[27,42] and i-motif DNA[25] to enter the vestibule, while internal hairpins,[41] large G-quadruplexes,[27] and large proteins[20,40] cannot enter the vestibule.

In this article, we report the use of αHL nanopore to identify structural differences between A-form DNA-RNA, DNA-PNA and B-form DNA-DNA. The A-form duplex (*d* = 2.4 nm)[43-45] has a diameter that is larger in diameter than that of the B-form duplex (*d* = 2.0 nm).[28,45]

The major differences between the A- and B-form duplex structures stem from the conformation of the sugar ring. In the B-form duplex, the sugar adopts the C2` endo

conformation, whereas the A-form has a C3` endo conformation as a consequence of the 2`-OH in RNA. Moreover, the bases in A-form duplexes are displaced away from the central axis resulting a ribbon-like helical structure[43] with a wider core and larger diameter (Figure. 4.1 C).

In the present study, a comparison between A- and B-form duplex unzipping in αHL was conducted by electrophoretically driving the anionic oligomers toward the nanopore. Lin et al.[46] have reported RNA-RNA unzipping in αHL and reported the kinetics of helix to coil transformation of polyadenylic acid inside the β-barrel. Calmer et al.[47] also have reported interaction between single-stranded RNA and the β-barrel. Therefore, for a better comparison, the A-form helix of a DNA-RNA hybrid was chosen over an RNA-RNA to eliminate possible interactions between the RNA overhang and the β-barrel. Examination of duplexes without a single-stranded tail and with a 10, or 24-nucleotide (nt)-tail attached to the 3`-end of one strand was probed, and comparisons of tail length versus unzipping of A- or B-form duplexes were made. Based on the work performed by Zhang et al.,[31] it is assumed that the A-form DNA-RNA duplex enter the vestibule before it unzips. However, our comparative studies provide data for a model that suggests that B-form duplexes enter the vestibule and unzip inside the nanopore, while the larger A-form DNA-RNA duplexes cannot enter the nanopore and unzip on the outside. These features impose practical limitations for attempting to study A-form duplexes inside the nanopore of wild-type αHL.

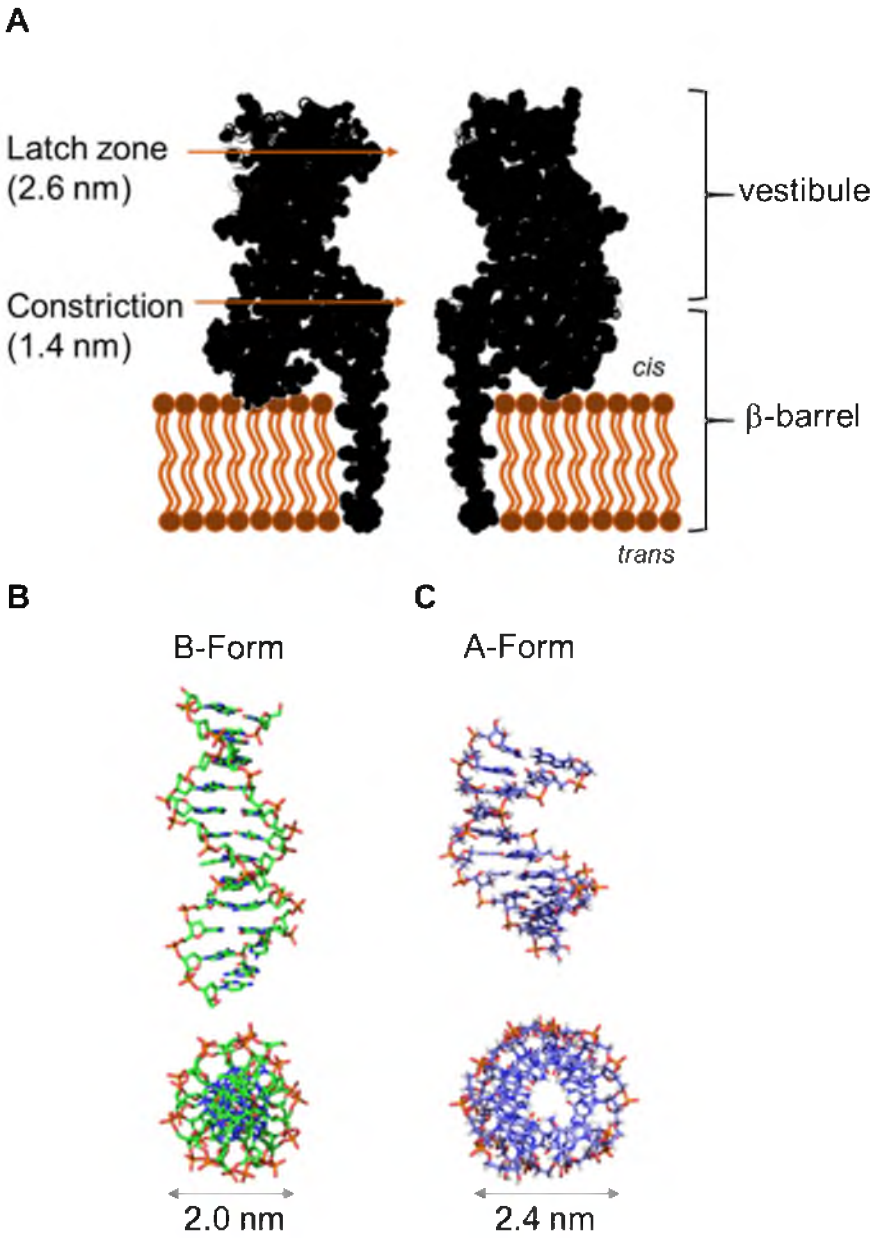

Figure 4.1. Structures for αHL and the duplex nucleic acids studied. (A) The structure of wild-type αHL based on an x-ray crystal structure (pdb 7αHL).[13] (B) The structure of a B-form DNA-DNA duplex (pdb 1BNA),[28] (C) and the structure of an A-form DNA-RNA duplex (pdb 1RRR).[43]

4.2 Experimental Section

4.2.1 DNA and RNA Preparation

All DNA and RNA strands were synthesized from commercially available phosphoramidites (Glen Research, Sterling, VA) by the DNA/Peptide core facility at the University of Utah. The synthesized DNA oligomers were cleaved from the solid support and deprotected according to the manufacturer's protocol. Afterward, the DNA oligomers were purified by ion-exchange HPLC using a previously described method.[23] The PNA oligomers were synthesized on NovaSyn TGR R resin (0.2 mmol/g) using solid-phase peptide synthesis via literature methods.[48] The PNA strands were purified by reversed-phase HPLC using a previously described method.[49] The purification salts were removed by dialysis against double-distilled water (ddH_2O) for 36 h at 4 °C followed by concentration of the oligomers via lyophiliziation. The lyophilized samples were resuspended in ddH_2O and the concentrations were determined by the absorbance at 260 nm using the primary sequence to derive the extinction coefficient. All other chemicals were used without further purification.

4.2.2 Chemicals and Materials

All electrolyte solutions contained 1 M KCl, 10 mM PBS, and 1 mM EDTA at pH 7.4. A conical-shaped nanopore in a ~ 50-μm thick glass membrane at the end of the capillary was fabricated following literature methods[50] and was used to support the lipid bilayer[51]. Prior to lipid bilayer formation, the glass surface was modified with 2% (v:v) 3-cyanopropyldimethylchlorosilane in CH_3CN for 6 h at room temperature to introduce a moderately hydrophobic surface. A solution of 1,2-diphytanoyl-*sn*-glycero-3-

phosphochline (DPhPC) dissolved in decane at 10 mg/mL was used to form the bilayer. Monomeric αHL purchased from List Biological Laboratories was diluted to a 1 mg/mL solution in ultrapure water (18 MΩ·cm) and stored at -80 °C prior to use. The DNA-DNA and DNA-RNA duplexes were formed by mixing them at a ratio of 1:4 target to probe, to ensure complete hybridization followed by annealing in a 90 °C water bath for 3 min and cooling to room temperature over 2 h.

4.2.3 Ion Channel Recordings

Current-time (*i-t*) recordings were performed using a custom built high-impedance, and low-noise system (Electronic Bio Sciences Inc., San Diego, CA). The glass capillary and the reservoir was filled with the electrolyte solution. Two Ag/AgCl electrodes were placed in the solutions inside (*trans*) and outside (*cis*) of the capillary. A lipid bilayer formed across the glass nanopore membrane (GNM) was indicated by a resistance increase from ~10 MΩ to ~100 GΩ. A gas-tight syringe was used to apply a pressure of 30-50 mmHg to the inside of the GNM capillary to facilitate protein insertion into the lipid bilayer [51]. Heptameric wild-type αHL was reconstituted in the bilayer from the monomer peptide by adding 0.2 μL of a 1 mg/mL solution to the *cis* side (volume = 350 μL) of the GNM. Formation of a proper nanopore was determined by an I_o at 120 mV of 120 pA at 20 °C. Nanopore measurements were performed at different applied voltages (*trans* versus *cis*), while recording the data with a 10 kHz low-pass filter and a 50 kHz data acquisition rate. A K-type thermocouple was used to control the temperature with a precision of ± 0.5 °C.

4.2.4 Data Analysis

The *i*–*t* blockades longer than 500 μs were identified as duplex unzipping events. Shorter events were assigned to translocation of the excess single-stranded DNA (ssDNA) present in the solution. A 4:1 mol ratio (longer strand versus shorter strand, see sequences below) was used to anneal the duplex, in order to favor formation of the duplex. The current and duration of individual events were extracted using QUB 2.0.0.29 software and the data were analyzed using OriginPro 9.1. Density plots of blockade current versus duplex unzipping duration were generated using data analysis software provided by Electronic Bio Sciences Inc. (San Diego, CA). Histograms of the current amplitude were fitted by a Gaussian function; the maximum of the distribution is reported for each duplex structure. The unzipping time τ was extracted by fitting the time histograms to an exponential decay and measuring the decay constant τ. The error values reported are standard errors for individual experiments. Unless otherwise stated, the representative data presented in each figure is from a single experiment. However, each experiment was repeated at least three times. The residual current varies by only 0.2 - 0.4% between the different pores.

4.3 Results and Discussion

4.3.1 Unzipping of DNA-DNA versus DNA-RNA Duplexes

A- and B-form duplexes were pulled into the αHL nanopore via an electrophoretic force to investigate their unzipping behavior. The representative A-form duplex was comprised of one strand of DNA and one of RNA (DNA-RNA), while the representative B-form duplex was only DNA (DNA-DNA). The poly-C tail length was varied from 0, 10,

or 24-nt long. Both duplexes had the same sequence with the exception of U in RNA T in DNA.

DNA-RNA 5`-TCA TCA GTA GAA CTC AGA AAC $TCC_n$-3` n = 0, 10, or 24

3`-AGU AGU CAU CUU GAG UCU UUG AG-5`

DNA-DNA 5`-TCA TCA GTA GAA CTC AGA AAC $TCC_n$-3` n = 0, 10, or 24

3`-AGT AGT CAT CTT GAG TCT TTG AG-5`

Unzipping experiments were performed in solutions containing the DNA-DNA B-form duplex, the DNA-RNA A-form duplex, and a mixture of the A- and B-forms. A representative *i-t* trace for the mixture of A and B-form duplexes is shown in Figure 4.2 (data collected over 20 s for all three experiments are given supplemental material, Figure S4.1, S4.2, S4.3. Data collected in the presence of both A-and B-forms clearly identified significant differences between the unzipping times and blockage currents for the A- and B-form duplexes as demonstrated in Figure 4.3.

A solution of the DNA-DNA B-form duplex studied at 120 mV (*trans* versus *cis*) gave a Gaussian-distributed histogram (n = 433) of blocking currents centered at 17 ± 0.1 pA (Figure 4.3A). Analysis of this population found an exponential distribution of times with a time constant (τ) of 390 ± 9 ms. The observed exponential time distribution is expected based on the first order kinetic model for duplex unzipping, [29] and consistent with the previous studies reported. [34,52,53] Next, a solution of the DNA-RNA A-form duplex, studied under identical conditions, showed a Gaussian-distributed histogram (n = 794) of

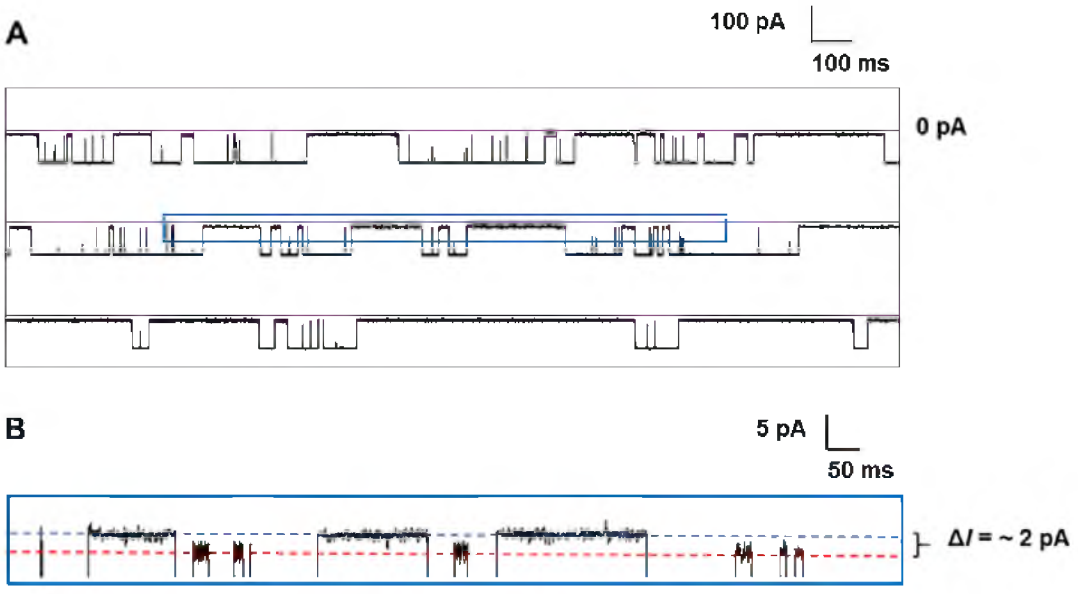

Figure 4.2. (A) A representative *i-t* trace showing uninterrupted data collected at 10 kHz at 120 mV. The mixture contained 8 μM of both A- and B-form duplexes with a 24-nt overhang in 1 M KCl, 10 mM PBS, pH 7.4 at 20 °C. (B) The expanded window in Figure 4.2 shows the deep-block current differences between A- and B-form duplexes. The red dashed line represents the blocking current of A- form duplex and the blue dashed line indicates the blocking current of B-form duplex during the unzipping process based on the individual experiments shown on Figure 4.3 A and 4.3 B. The expanded trace in (B) is filtered to 1 kHz for presentation purposes

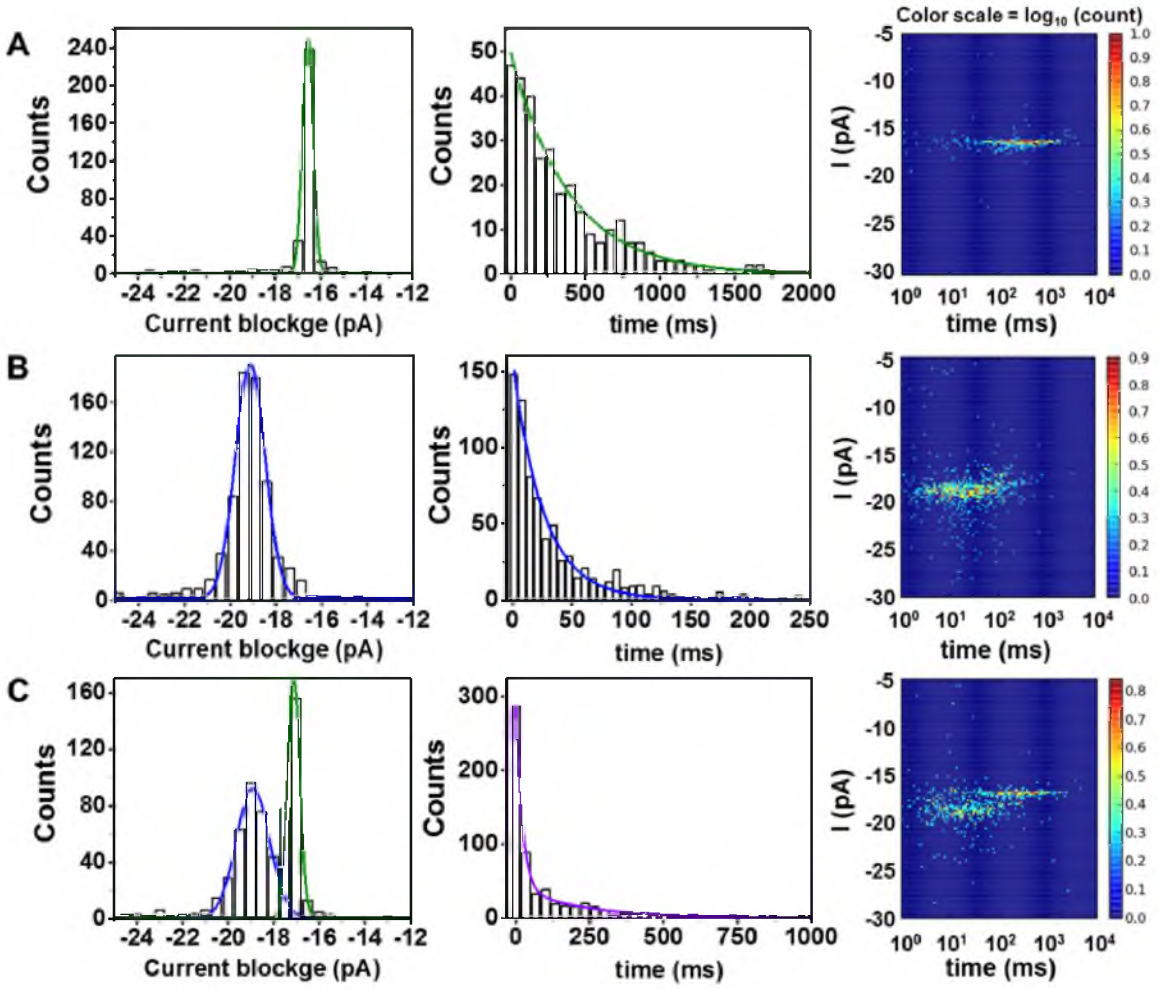

Figure 4.3. Current blockage, unzipping time duration, and *i-t* density plots for the duplex systems studied. (A) DNA-DNA duplex (B-form), (B) DNA-RNA duplex (A-form), and (C) A- and B-form duplexes analyzed as a 1:1 mixture. All experiments were performed at 120 mV (*trans* versus *cis*) in 1 M KCl (10 mM PBS, pH 7.4), at 20 °C in the presence of 8 μM duplex.

blocking currents of 19 ± 0.2 pA (Figure 4.3B). A broader distribution of blockage currents was observed for the DNA-RNA duplex unzipping, a consequence of the shorter timescale of analysis compared to the longer unzipping duration of the DNA-DNA duplex. Again, an exponential distribution of times was observed with τ = 25.9 ± 0.6 ms. Voltage-dependent studies for both duplex systems demonstrated that the unzipping duration decreases with the applied voltage (Figure S4.4), providing further evidence for unzipping.[54,55]

We also performed an unzipping experiment for DNA-RNA with a 40-nt overhang to investigate the dependence of unzipping kinetics on overhang length above 24-nt (Figure S4.5). The difference between the residual currents for the DNA-RNA with 24-nt and 40-nt overhangs is 0.4%, while the unzipping time differed only by 4.4 ± 2.1 ms. The results suggests the longer overhang above 24-nt has a small effect on unzipping time or current blockage. Lastly, when both duplex systems were mixed together in an equimolar ratio, a histogram of blocking currents (n = 652) identified two Gaussian populations, one centered at 17 pA and the other at 19 pA (Figure 4.3C). The areas under the fitted Gaussian distributions were nearly identical (~295 and 269 events), suggesting the capture frequency to be independent of the duplex form, consistent with the capture frequency observed when each duplex was studied individually.

Comparisons between the A- and B-form duplex unzipping results identify critical differences in the unzipping times and blocking currents that at first glance appear to be counterintuitive. The larger A-form duplex gave a larger residual current (i.e., less blocking to the current) by 2 pA compared to the smaller B-form duplex (Figure 4.3C). Additionally, previous studies have demonstrated that A-form duplexes are generally more

stable than B-form duplexes of the same sequences.[56] This feature is determined by thermal melting experiments that identify the temperature (T_m) of the midpoint during the thermal denaturing process. A-form duplexes generally have T_m values that are 10 - 15 °C above those measured for B-form duplexes with the same sequence (except U in RNA and T in DNA).[57] For the electrolytes used here, the A-form duplex showed a T_m 10.5 °C greater than the B-form duplex under the nanopore buffer and electrolyte conditions (Figure S4.6). On the basis of these comparisons, it was anticipated that the A-form duplex would exhibit the longer unzipping time. However, the opposite was observed, the A-form duplex displayed a 15-fold faster unzipping time than the B-form duplex (Figure 4.3) at 120 mV.

The following models were developed (Figure 4.4) to understand these findings. Smaller B-form duplexes pass through the latch zone and enter the vestibule, where they slowly unzip within the sterically confined protein cavity. In contrast, the wider A-form duplex cannot pass through the latch zone into the vestibule and unzips outside the protein with fewer steric constraints inhibiting the unzipping process. Apart from the size of the structures, the conformational difference of the phosphate backbone between A- and B-form can change the hydration of the duplex.[58] Several X-ray crystal and MD simulation studies have confirmed that the cations and water molecules are well-ordered and less mobile in A-form compare to B-form duplexes.[58-62] Therefore, we hypothesize that the stable systematic arrangement of solvent in the A-form can also create a barrier to entry into the nanopore.

This model is also consistent with the smaller, less stable B-form duplex causing greater blockage to the open channel current and having the greater unzipping time, while

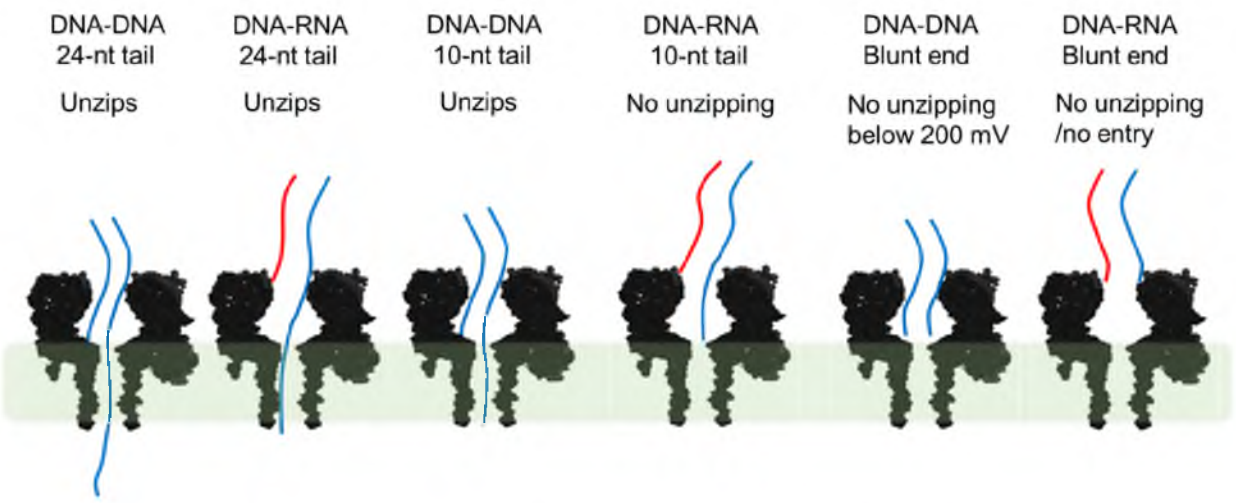

Figure 4.4. Proposed models for trapping and unzipping of DNA-RNA (A-form) and DNA-DNA (B-form) duplexes. The green color region show the highest voltage drop across the pore based on both experiments and molecular dynamics simulations.[54,63,64]

the wider, more stable A-form duplex is less blocking to the open channel current and has the shorter unzipping time because only the single-stranded overhang enters the nanopore.

This size-dependent model was previously proposed in studies performed in our laboratories, in which we identified fishhook hairpins to unzip slower than an internal hairpin.[41] The internal hairpin cannot enter the vestibule and unzips outside the vestibule giving rise to a lower unzipping time (5 – 20 X, depending on the sequence) compared to the fishhook hairpin that can be accommodated in the vestibule, similar to our present model. The following experiments provide additional support for this model.

The vestibule of αHL is ~ 5 nm long[13], and on the basis of previous studies, this spans ~10 nucleotides of ssDNA.[63,65] Therefore, to test if the A-form duplex was unzipping outside the nanopore, the tail length was decreased to 10-nt. The A-form duplex with a 10-nt tail will only lead to shallow current blockages because the tail cannot penetrate the central constriction of αHL. In contrast, a B-form duplex with a 10-nt tail should enter the

vestibule allowing the tail to pass the central constriction and fill the β-barrel leading to deep blockages. The DNA-RNA A-form duplex with a 10-nt tail yielded shallow blockages (Type 1) (%I/I_o ~ 50 ± 5%) and had residence times <100 μs (Figure 4.5A and Figure S4.7). Based on previous reports,[18,21,66,67] the residual current observed indicates the 10-nt overhang enters the vestibule but does not pass the central constriction, and cannot translocate through the pore. Interestingly, the event duration increased with increased voltage (Figure 4.5C and Figure S4.8), and the absence of deep block current level supports the proposal that the A-form duplex is being held on outside of the vestibule by the aid of the overhang before it eventually diffuses back to the bulk solution on the *cis* side.

4.3.2 Unzipping of DNA-DNA versus DNA-RNA Duplexes with 10-nt overhang

On the other hand, the DNA-DNA B-form duplex yielded two event types (Type 2 and 3) based on the *i-t* traces observed (Figure 4.5B and Figure S4.9). The Type 2 events showed deep blockages to the current (%I/I_o = 12 ± 1%), and the event time decreased as the voltage was increased (Figure 4.5C). These observations support the 10-nt tail entering the β-barrel before the duplex unzips.

Type 3 events comprise ~10% of the total events and gave residual currents at %I/I_o = 24 ± 1% with stochastic spikes to %I/I_o = 10 ± 1%. The residual current %I/I_o = 24 ± 1 indicates that the duplex portion of the molecule enters the vestibule but does not occupy the β-barrel.[68] The spikes between 24 ±1 pA and 10 ± 1 pA are due to the terminal nucleotides trying to enter the constriction zone and going back to the vestibule zone before exits from the *cis* side of the nanopore when the polarity of the voltage is reversed. Similar observation

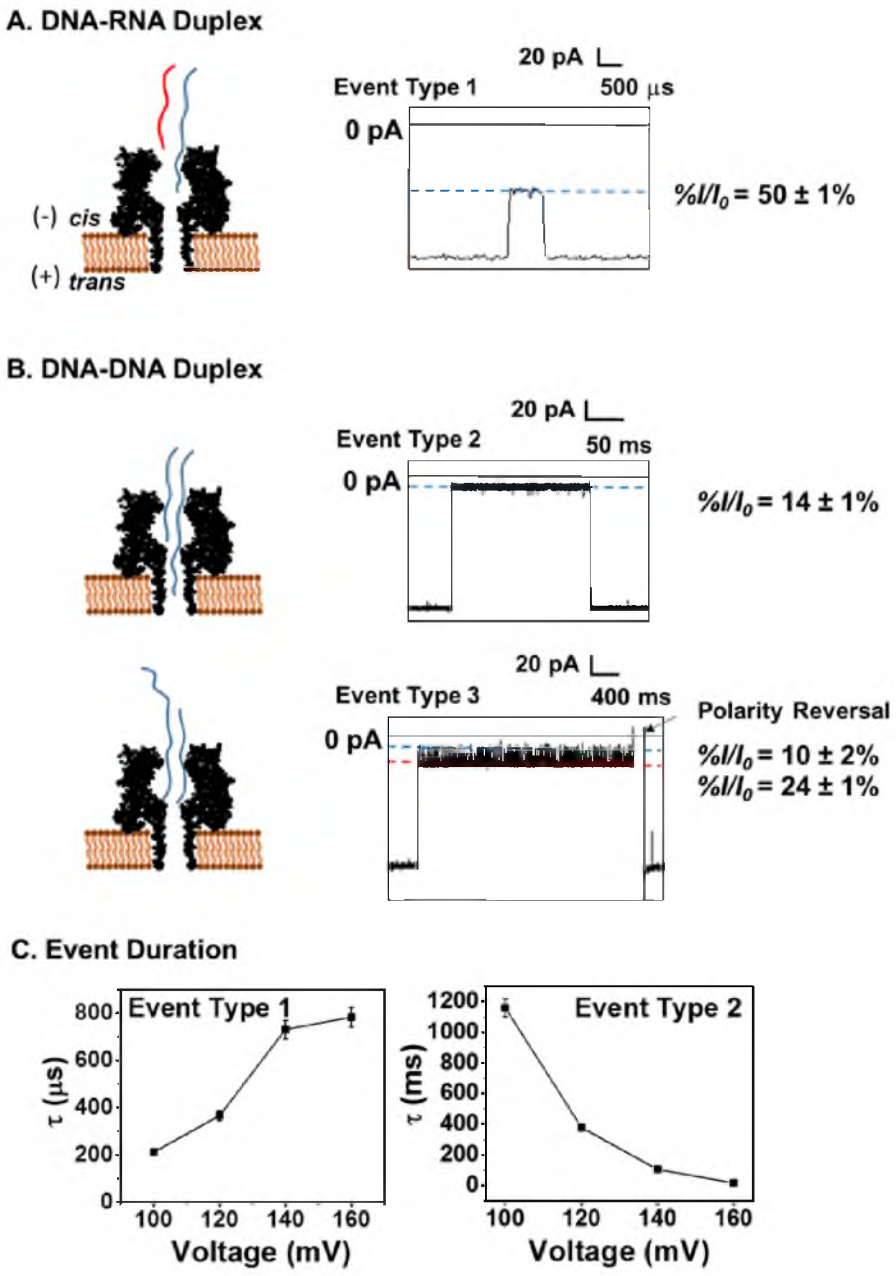

Figure 4.5. Studies for unzipping of A- and B-form duplexes with a shorter 10-nt tail. (A) Unzipping of DNA-RNA (B) DNA-DNA duplexes. All experiments were performed at 120 mV in 1 M KCl (10 mM PBS, pH 7.4) at 20 °C. Event durations for Type 1 (C, left) and Type 2 (C, right) were recorded at voltages from 100 – 160 mV.

has been reported for analysis of blunt-ended B-form duplex interactions with the constriction zone inside the vestibule of αHL.[39,40]

4.3.3 Unzipping of DNA-DNA versus DNA-RNA Duplexes with no Overhang

A second study with all blunt-ended A- and B-form duplexes provided additional support for our model. The DNA-RNA A-form duplex without a tail should not lead to any long-lived events, because they cannot pass the opening of αHL. Studies with this duplex at 80 – 200 mV did not give events with lifetimes > 500 μs (Figure 4.6A and Figure S4.10). This observation supports the absence of the overhang prohibiting entrance of the A-form duplex into the vestibule. The only *i-t* traces observed represented excess single-stranded DNA with event times < 100 μs. This further verifies our model that A-form duplexes cannot enter the vestibule.

The *i-t* traces corresponding to blunt-ended B-form duplexes yielded deep blockage currents with two distinct types of *i-t* patterns termed Type 3a and 3b (Figure 4.6B and Figure S4.11). Both event types were long-lived and did not lead to unzipping events below 200 mV.

The Type 3a events had residual currents of $\%I/I_o = 24 \pm 1\%$ (Figure 4.6B), a value we previously identified as the duplex inside the vestibule held up against the central constriction (Figure 4.5B).[54,68] The Type 3b events gave residual currents of $\%I/I_o = 24 \pm 1\%$ with spikes to lower residual currents of $\%I/I_o = 11 \pm 1\%$. This *i-t* pattern is similar to previous studies,[39,68] in which the deflections to lower currents were ascribed to the terminal base pairs partially opening and interacting with the central constriction zone (Figure 4.6B).

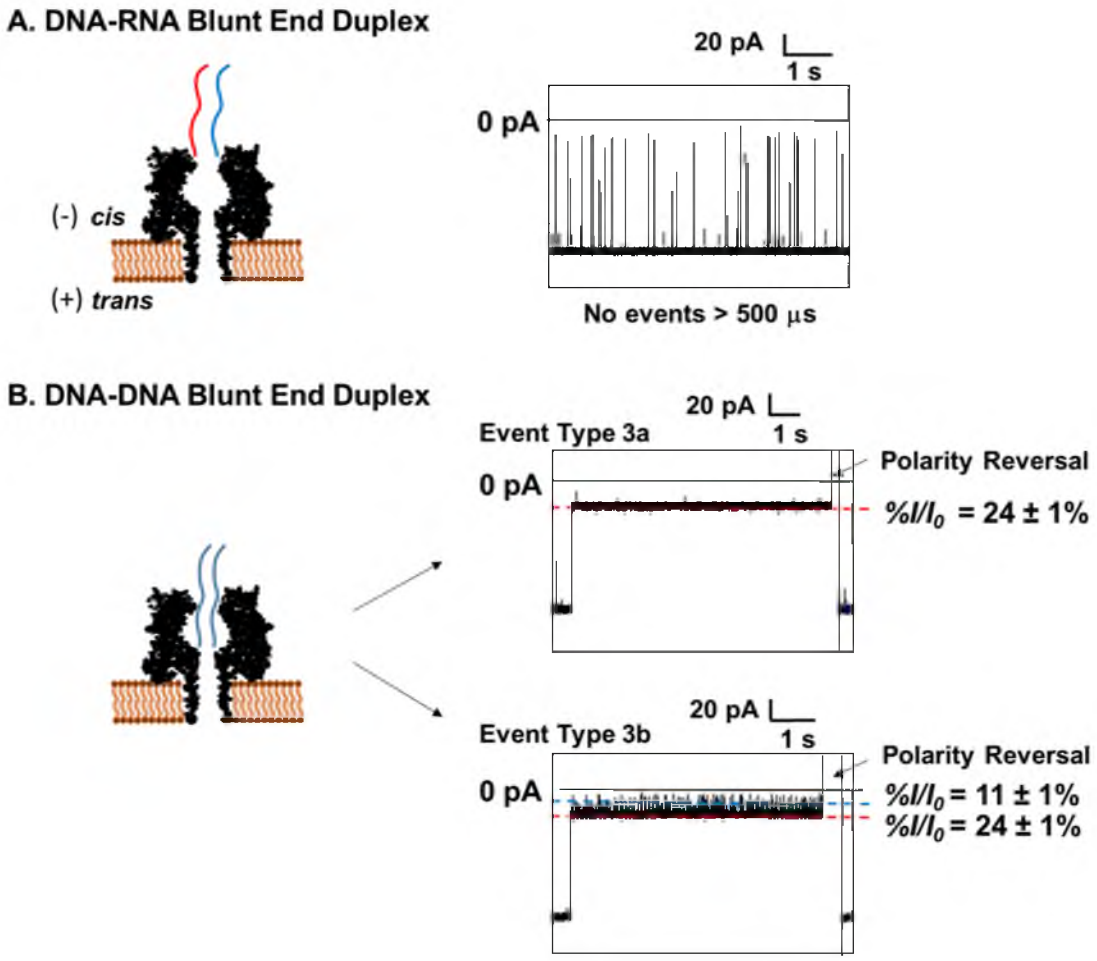

Figure 4.6. Unzipping of A- and B-form duplexes without a single-stranded tail. (A) Unzipping of DNA-RNA blunt-end duplex, (B) DNA-DNA blunt-end duplex. All experiments were performed at 120 mV (*trans* versus *cis*) in 1 M KCl (10 mM PBS, pH 7.4) at 20 °C.

This can be further supported by the voltage dependent frequency of fluctuations between the two current levels (see supplemental material, S4.11 and S4.12). These tail-length dependent studies provide further support to our hypothesis that A-form duplexes are incapable passing through the mouth of the vestibule.

Both experimentally mapped[69] and molecular dynamics simulation results[64] indicate that the voltage drop in the αHL nanopore occurs mainly at the β-barrel (~90%, green highlighted zone in Figure 4.4).[54] Because the DNA-DNA duplex can enter the vestibule, the highlighted region is fully occupied by both DNA-DNA duplexes having 10-nt and 24-nt overhangs (Figure 4.4). Therefore, both duplexes are subjected to nearly the same amount of force (F = Eq, where F = electrophoretic force, E = electric field, and q = charge that is proportional to the length of the overhang occupying the field). The unzipping duration for both molecules are in the same order of magnitude (430 ms and 380 ms at 120 mV, respectively) further supporting the conclusion that both molecules inside the vestibule during unzipping. However, the DNA-RNA duplex does not enter the vestibule and only a duplex with a long overhang will penetrate deep into the pore where the force is great enough to unzip the duplex.

In this study with the A-form duplex, a 24-nt overhang is long enough to occupy the β-barrel ($\%I/I_o = 14 \pm 1$) to experience the electric field and unzip; whereas the 10-nt overhang only occupies the vestibule ($I/I_o = 50 \pm 2$) and is not subject to the greater electric force leading to unzipping, and it eventually diffuses away. The blunt-end DNA-DNA enters the vestibule ($\%I/I_o > 24$) and the DNA–RNA duplex does not enter the vestibule, based on the blockage current, further validating our proposed model (Figure 4.4).

In previous studies, we and others interrogated B-form duplex DNA when it was

trapped inside the vestibule.[23,36,37] On the basis of these results, similar experiments cannot be performed with A-form duplexes. We next asked if other biopolymers that form A-form helices also unzip outside the αHL pore. DNA-PNA duplexes also adopt an A-form helix[70] and are more stable compare to the B-form. Therefore, we analyzed the behavior of a DNA-PNA duplex with αHL pore. Due to complications of synthesis and low solubility, we used a 10 base-pair long PNA-DNA duplex (sequence is given in Figure S4.13). This is the first time the unzipping behavior of DNA-PNA duplex has been investigated and the *i-t* traces are shown in Figure 4.7. Data collected over 20 s is given in, Figure S4.13 and the voltage dependence of the unzipping time is given in, Figure S4.14.

The unzipping time observed for DNA-PNA duplex is shown in Figure 4.8. The observed unzipping time is in the same order of magnitude to the values observed for A-form. Therefore, the data from this experiment provided the residence times consistent with unzipping outside the vestibule of αHL (Figure 4 8).

Based on the faster unzipping time compare to B-form duplex, this study further supports the proposal that A-form duplexes cannot enter the vestibule and unzipping occurs outside the nanopore. To interrogate the significance of the orientation of the tail in unzipping, we also have performed unzipping experiments with a 5'-poly C tail (24-nt).

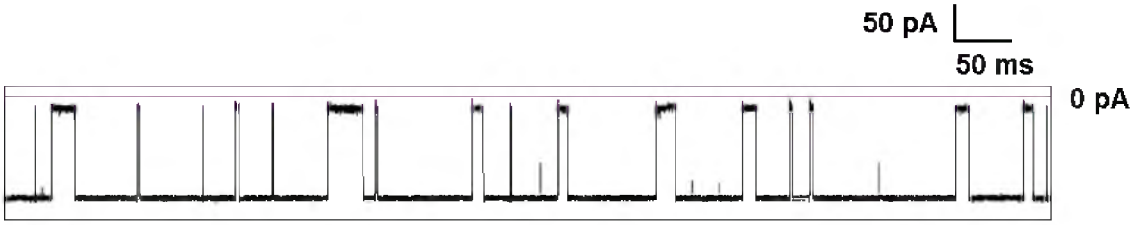

Figure 4.7. A sample *i-t* trace showing uninterrupted data collected at 10 kHz at 120 mV. The mixture contained 8 μM DNA-PNA duplexes in 1 M KCl, 10 mM PBS, pH 7.4 at 20 °C.

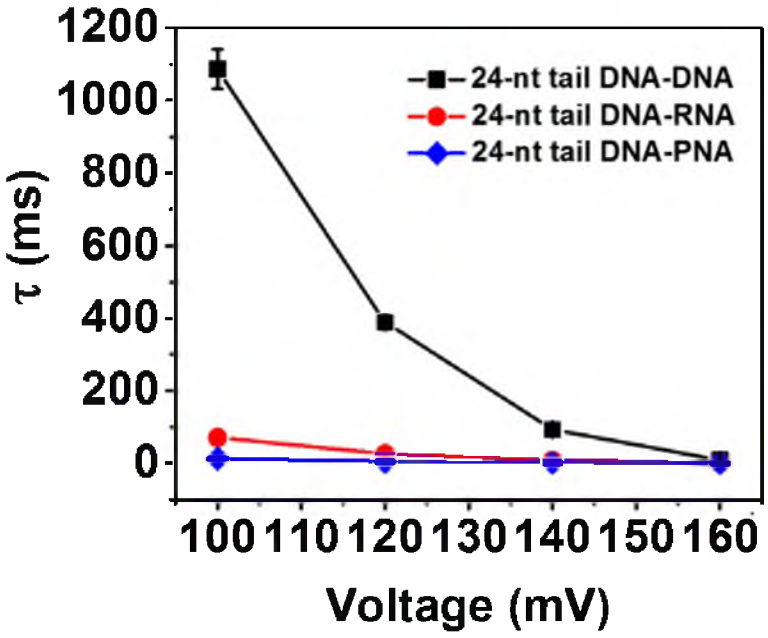

Figure 4.8. Unzipping duration as a function of voltage for DNA-DNA (black), DNA-RNA (red) and DNA-PNA (blue). The data were recorded at 20 °C in 1 M KCl, 10 mM PBS, pH 7.4. The data were fit in to an exponential decay equation to obtain the unzipping time.

The unzipping times did not show any difference (25.8 ms and 30.2 ms for 3' and 5' overhangs, respectively. Details are given in supplemental material, Figure S4.15). Based on our studies, we conclude the orientation of the overhang that enters the nanopore does not change the position of the duplex during the unzipping process. With the help of this systematic study, we demonstrate that the A- form DNA-RNA duplex cannot enter the vestibule as assumed in previous studies performed by Zhang et al.[31] and αHL nanopore can be used as a tool to identify the structural differences between A-and B-form duplexes.

Utilization of a probe-based approach to interrogate DNA and RNA has enormous potential for biotechnology applications.[31-33] For example, DNA probes complementary to microRNAs[31,33] diagnostic of cancer progression were detected and quantified with wild-type αHL. In probing experiments, the A-form DNA-RNA heteroduplexes were

counted when a current deflection to the open channel current was observed; however, the underlying details of the *i-t* traces were not deeply examined. Two recent studies reported by Wang et al.[54,71] have highlighted the importance of understanding the unzipping process of DNA-RNA. Interestingly, none of these studies actually used DNA-RNA duplexes but used DNA-DNA duplexes as a model.

To answer the questions we performed a systematic study to interrogate the current and dwell time differences that lead us to propose a model for unzipping and trapping of the two different forms of the duplexes, A versus B (Figure 4.4). However, these results impose practical limitations if studies are designed to interrogate A-form duplexes inside the vestibule of wild-type αHL. Because a high-resolution structure of this nanopore exists, site-directed mutagenesis may allow engineering of new proteins with larger openings to the vestibule that can accommodate entry of A-form duplexes.

4.4 Conclusions

This study demonstrated the structural differences between A- and B-form duplexes lead to different trapping, unzipping, and escaping processes when interacting with the wild-type αHL nanopore in an electric field (Figure 4.4). Studies that varied the length of the single-stranded overhang on the duplexes were used to probe the unzipping processes. These duplex-dependent differences in unzipping were described by a model in which the A-form duplexes do not enter the vestibule of wild-type αHL, leading to unzipping on the exterior of the nanopore. Characteristics of this unzipping process were a higher residual current and faster unzipping time. In contrast, B-form duplexes can enter the vestibule where they unzip with a deeper block to the current and require a longer time to unzip.

Next, A-form duplex unzipping was regulated by the overhang length that determines unzipping versus escaping from the nanopore. Further, the nature of the A-form duplex, DNA-RNA or DNA-PNA, unzips via the same model. This work identifies key differences between unzipping of A- and B-form duplexes in wild-type αHL that will prove to be critical in the design of any probe-based methods utilizing this protein nanopore.

4.5. References

(1) Deblois, R. W.; Bean, C. P. *Rev. Sci. Instrum.* **1970**, *41*, 909.

(2) Ito, T.; Sun, L.; Crooks, R. M. *Anal. Chem.* **2003**, *75*, 2399.

(3) Saleh, O. A.; Sohn, L. L. *Proc. Natl. Acad. Sci. U.S.A.* **2003**, *100*, 820.

(4) Bezrukov, S. M.; Kasianowicz, J. J. *Phys. Rev. Lett.* **1993**, *70*, 2352.

(5) Braha, O.; Walker, B.; Cheley, S.; Kasianowicz, J. J.; Song, L.; Gouaux, J. E.; Bayley, H. *Chem. Biol.* **1997**, *4*, 497.

(6) Bezrukov, S. M.; Vodyanoy, I.; Parsegian, V. A. *Nature* **1994**, *370*, 279.

(7) Siwy, Z.; Dobrev, D.; Neumann, R.; Trautmann, C.; Voss, K. *Appl. Phys. A.* **2003**, *76*, 781.

(8) Song, L.; Hobaugh, M. R.; Shustak, C.; Cheley, S.; Bayley, H.; Gouaux, J. E. *Science* **1996**, *274*, 1859.

(9) Yamashita, K.; Kawai, Y.; Tanaka, Y.; Hirano, N.; Kaneko, J.; Tomita, N.; Ohta, M.; Kamio, Y.; Yao, M.; Tanaka, I. *Proc. Natl. Acad. Sci. U. S. A.* **2011**, *108*, 17314.

(10) Gu, L. Q.; Braha, O.; Conlan, S.; Cheley, S.; Bayley, H. *Nature* **1999**, *398*, 686.

(11) Kasianowicz, J. J.; Burden, D. L.; Han, L. C.; Cheley, S.; Bayley, H. *Biophys. J.* **1999**, *76*, 837.

(12) Menestrina, G. *J. Membr. Biol.* **1986**, *90*, 177.

(13) Song, L.; Hobaugh, M. R.; Shustak, C.; Cheley, S.; Bayley, H.; Gouaux, J. E. *Science.* **1996**, *274*, 1859.

(14) Movileanu, L.; Schmittschmitt, J. P.; Scholtz, J. M.; Bayley, H. *Biophys. J.* **2005**, *89*, 1030.

(15) Nivala, J.; Marks, D. B.; Akeson, M. *Nat. Biotechnol.* **2013**, *31*, 247.

(16) Kullman, L.; Winterhalter, M.; Bezrukov, S. M. *Biophys. J.* **2002**, *82*, 803.

(17) Kasianowicz, J. J.; Brandin, E.; Branton, D.; Deamer, D. W. *Proc. Natl. Acad. Sci. U.S.A.* **1996**, *93*, 13770.

(18) Akeson, M.; Branton, D.; Kasianowicz, J. J.; Brandin, E.; Deamer, D. W. *Biophys. J.* **1999**, *77*, 3227.

(19) Wanunu, M.; Dadosh, T.; Ray, V.; Jin, J.; McReynolds, L.; Drndic, M. *Nat. Nanotechnol.* **2010**, *5*, 807.

(20) Henrickson, S. E.; Misakian, M.; Robertson, B.; Kasianowicz, J. J. *Phys. Rev. Lett.* **2000**, *85*, 3057.

(21) Vercoutere, W.; Winters-Hilt, S.; Olsen, H.; Deamer, D.; Haussler, D.; Akeson, M. *Nat. Biotechnol.* **2001**, *19*, 248.

(22) Meller, A.; Nivon, L.; Branton, D. *Phys. Rev. Lett.* **2001**, *86*, 3435.

(23) Jin, Q.; Fleming, A. M.; Johnson, R. P.; Ding, Y.; Burrows, C. J.; White, H. S. *J. Am. Chem. Soc.* **2013**, *135*, 19347.

(24) Shim, J. W.; Tan, Q.; Gu, L. Q. *Nucleic Acids Res.* **2009**, *37*, 972.

(25) Ding, Y.; Fleming, A. M.; He, L.; Burrows, C. J. *J. Am. Chem. Soc.* **2015**, *137* 9053.

(26) An, N.; Fleming, A. M.; White, H. S.; Burrows, C. J. *ACS Nano* **2015**, *9*, 4296.

(27) An, N.; Fleming, A. M.; Middleton, E. G.; Burrows, C. J. *Proc. Natl. Acad. Sci. U.S.A.* **2014**, *111*, 14325.

(28) Drew, H. R.; Wing, R. M.; Takano, T.; Broka, C.; Tanaka, S.; Itakura, K.; Dickerson, R. E. *Proc. Natl. Acad. Sci. U S.A.* **1981**, *78*, 2179.

(29) Sauer-Budge, A. F.; Nyamwanda, J. A.; Lubensky, D. K.; Branton, D. *Phys. Rev. Lett.* **2003**, *90*, 238101.

(30) Wang, Y.; Luan, B.-Q.; Yang, Z.; Zhang, X.; Ritzo, B.; Gates, K.; Gu, L.-Q. *Sci. Rep.* **2014**, *4*.

(31) Zhang, X.; Wang, Y.; Fricke, B. L.; Gu, L. Q. *ACS Nano.* **2014**, *8*, 3444.

(32) Tian, K.; He, Z.; Wang, Y.; Chen, S.-J.; Gu, L. Q. *ACS Nano.* **2013**, *7*, 3962.

(33) Wang, Y.; Zheng, D.; Tan, Q.; Wang, M.; Gu, L. Q. *Nat. Nanotechnol.* **2011**, *6*, 668.

(34) Schibel, A. E. P.; Fleming, A. M.; Jin, Q.; An, N.; Liu, J.; Blakemore, C. P.; White, H. S.; Burrows, C. J. *J. Am. Chem. Soc.* **2011**, *133*, 14778.

(35) Sutherland, T. C.; Dinsmore, M. J.; Kraatz, H.-B.; Lee, J. S. *BCB* **2004**, *82*, 407.

(36) Jin, Q.; Fleming, A. M.; Ding, Y.; Burrows, C. J.; White, H. S. *Biochemistry* **2013**, *52*, 7870.

(37) Johnson, R. P.; Fleming, A. M.; Burrows, C. J.; White, H. S. *J. Phys. Chem. Lett.* **2014**, *5*, 3781.

(38) Johnson, R. P.; Fleming, A. M.; Jin, Q.; Burrows, C. J.; White, H. S. *Biophys. J.* **2014**, *107*, 924.

(39) Vercoutere, W. A.; Winters-Hilt, S.; DeGuzman, V. S.; Deamer, D.; Ridino, S. E.; Rodgers, J. T.; Olsen, H. E.; Marziali, A.; Akeson, M. *Nucleic. Acids. Res.* **2003**, *31*, 1311.

(40) Winters-Hilt, S.; Vercoutere, W.; DeGuzman, V. S.; Deamer, D.; Akeson, M.; Haussler, D. *Biophys. J.* **2003**, *84*, 967.

(41) Ding, Y.; Fleming, A. M.; White, H. S.; Burrows, C. J. *J. Phys. Chem. B.* **2014**, *118*, 12873.

(42) Shim, J. W.; Gu, L.-Q. *J. Phy.Chem. B.* **2008**, *112*, 8354.

(43) Gyi, J. I.; Lane, A. N.; Conn, G. L.; Brown, T. *Biochemistry* **1998**, *37*, 73.

(44) Wang, A. H. J.; Fujii, S.; van Boom, J. H.; van der Marel, G. A.; van Boeckel, S. A. A.; Rich, A. *Nature* **1982**, *299*, 601.

(45) Arias-Gonzalez, J. R. *Integr. Biol.* **2014**, *6*, 904.

(46) Lin, J.; Kolomeisky, A.; Meller, A. *Phys. Rev. Lett.* **2010**, *104*, 158101.

(47) Clamer, M.; Höfler, L.; Mikhailova, E.; Viero, G.; Bayley, H. *ACS Nano.* **2014**, *8*, 1364.

(48) Joshi, R.; Jha, D.; Su, W.; Engelmann, J. *J. Pept. Sci.* **2011**, *17*, 8.

(49) De Costa, N. T. S.; Heemstra, J. M. *PLOS ONE* **2013**, *8*, e58670.

(50) Zhang, B.; Galusha, J.; Shiozawa, P. G.; Wang, G.; Bergren, A. J.; Jones, R. M.; White, R. J.; Ervin, E. N.; Cauley, C. C.; White, H. S. *Anal. chem.* **2007**, *79*, 4778.

(51) White, R. J.; Ervin, E. N.; Yang, T.; Chen, X.; Daniel, S.; Cremer, P. S.; White, H. S. *J. Am. Chem. Soc.* **2007**, *129*, 11766.

(52) Jin, Q.; Fleming, A. M.; Burrows, C. J.; White, H. S. *J. Am. Chem. Soc.* **2012**, *134*, 11006.

(53) Nakane, J.; Wiggin, M.; Marziali, A. *Biophys. J.* **2004**, *87*, 615.

(54) Wang, Y.; Tian, K.; Hunter, L. L.; Ritzo, B.; Gu, L. Q. *Nanoscale* **2014**, *6*, 11372.

(55) Dudko, O. K.; Mathé, J.; Szabo, A.; Meller, A.; Hummer, G. *Biophys. J.* **2007**, *92*, 4188.

(56) Casey, J.; Davidson, N. *Nucleic Acids Res.* **1977**, *4*, 1539.

(57) Roberts, R. W.; Crothers, D. M. *Science* **1992**, *258*, 1463.

(58) Hud, N. V.; Polak, M. *Curr. Opin. Struct. Biol.* **2001**, *11*, 293.

(59) Feig, M.; Pettitt, B. M. *Biophys. J.* **1999**, *77*, 1769.

(60) McConnell, K. J.; Beveridge, D. L. *J. Mol. Biol.* **2000**, *304*, 803.

(61) Soler-Lopez, M.; Malinina, L.; Liu, J.; Huynh-Dinh, T.; Subirana, J. A. *Phys. Rev. Lett.* **1999**, *274*, 23683.

(62) Auffinger, P.; Westhof, E. *J. Mol. Biol.* **2001**, *305*, 1057.

(63) Howorka, S.; Bayley, H. *Biophys. J.* **2002**, *83*, 3202.

(64) Aksimentiev, A.; Schulten, K. *Biophys. J.* **2005**, *88*, 3745.

(65) Stoddart, D.; Heron, A. J.; Mikhailova, E.; Maglia, G.; Bayley, H. *Proc. Natl. Acad. Sci. U.S.A* **2009**, *106*, 7702.

(66) Deamer, D. W.; Branton, D. *Acc. Chem. Res.* **2002**, *35*, 817.

(67) Mathé, J.; Aksimentiev, A.; Nelson, D. R.; Schulten, K.; Meller, A. *Proc. Natl. Acad. Sci. U.S.A.* **2005**, *102*, 12377.

(68) Liu, A.; Zhao, Q.; Krishantha, D. M.; Guan, X. *J. Phys. Chem. Lett.* **2011**, *2*, 1372.

(69) Howorka, S.; Bayley, H. *Biophysical Journal* **2002**, *83*, 3202.

(70) Wittung, P.; Nielsen, P. E.; Buchardt, O.; Egholm, M.; Norden, B. *Nature* **1994**, *368*, 561.

(71) Wang, X.; Li, Y.; Li, T.; Liu, L.; Wu, H.-C. *Sci. China Chem.* **2015**, 1.

S4.6 Supplemental Material

S4.6.1 Sample *i-t* trace of a mixture containing B-form duplex.

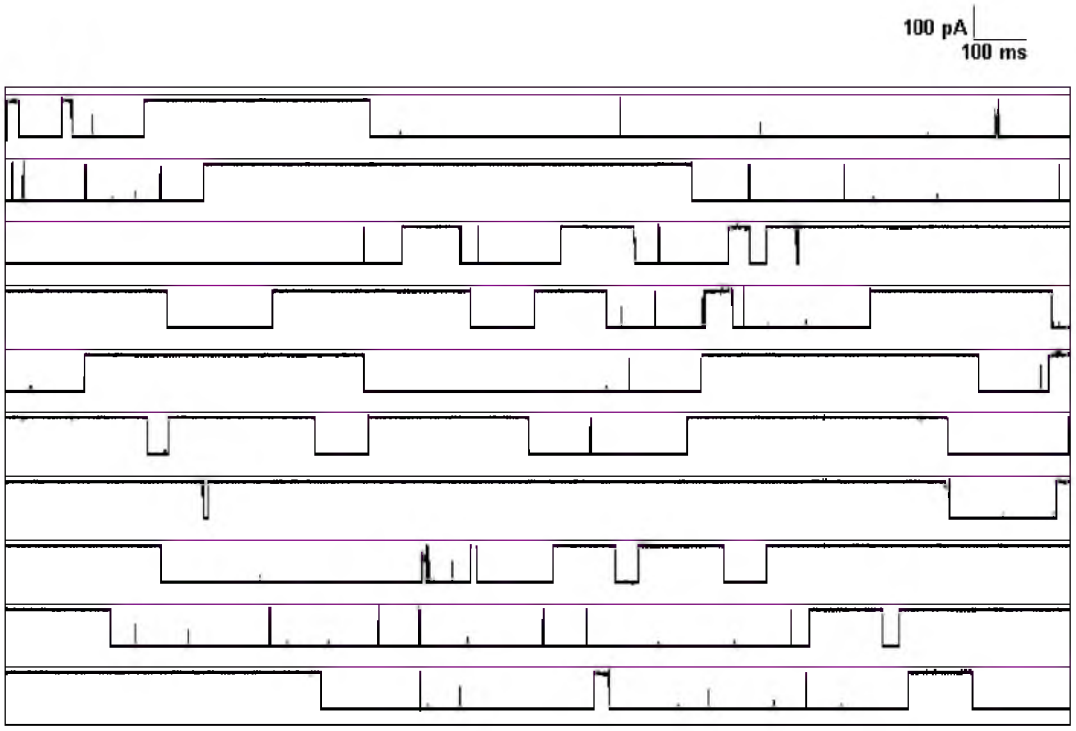

Figure S4.1. A sample *i-t* trace showing uninterrupted data collected at 10 kHz for 20 s at 120 mV. The mixture contained 8 μM B-form duplex in 1 M KCl, 10 mM PBS, pH 7.4 at 20 °C.

S4.6.2 Sample *i-t* trace of a mixture containing A-form duplex.

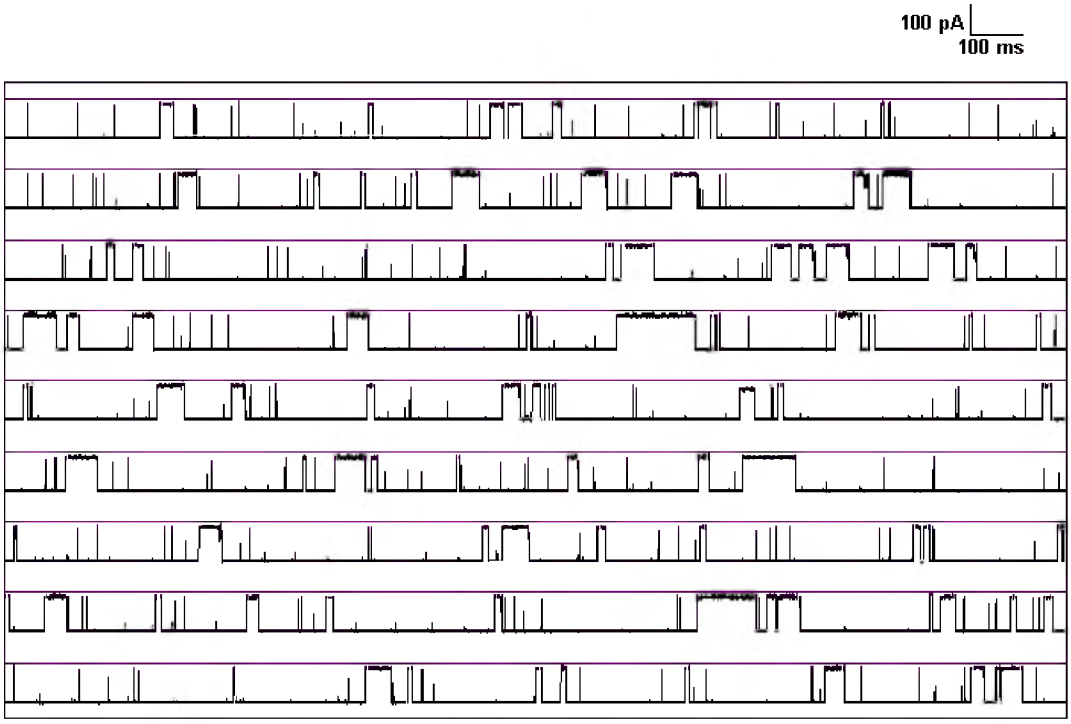

Figure S4.2. A sample *i-t* trace showing uninterrupted data collected at 10 kHz for 20 s at 120 mV. The mixture contained 8 μM A-form duplex in 1 M KCl, 10 mM PBS, pH 7.4 at 20 °C.

S4.6.3 Sample *i-t* trace of a mixture containing both A- and B-form.

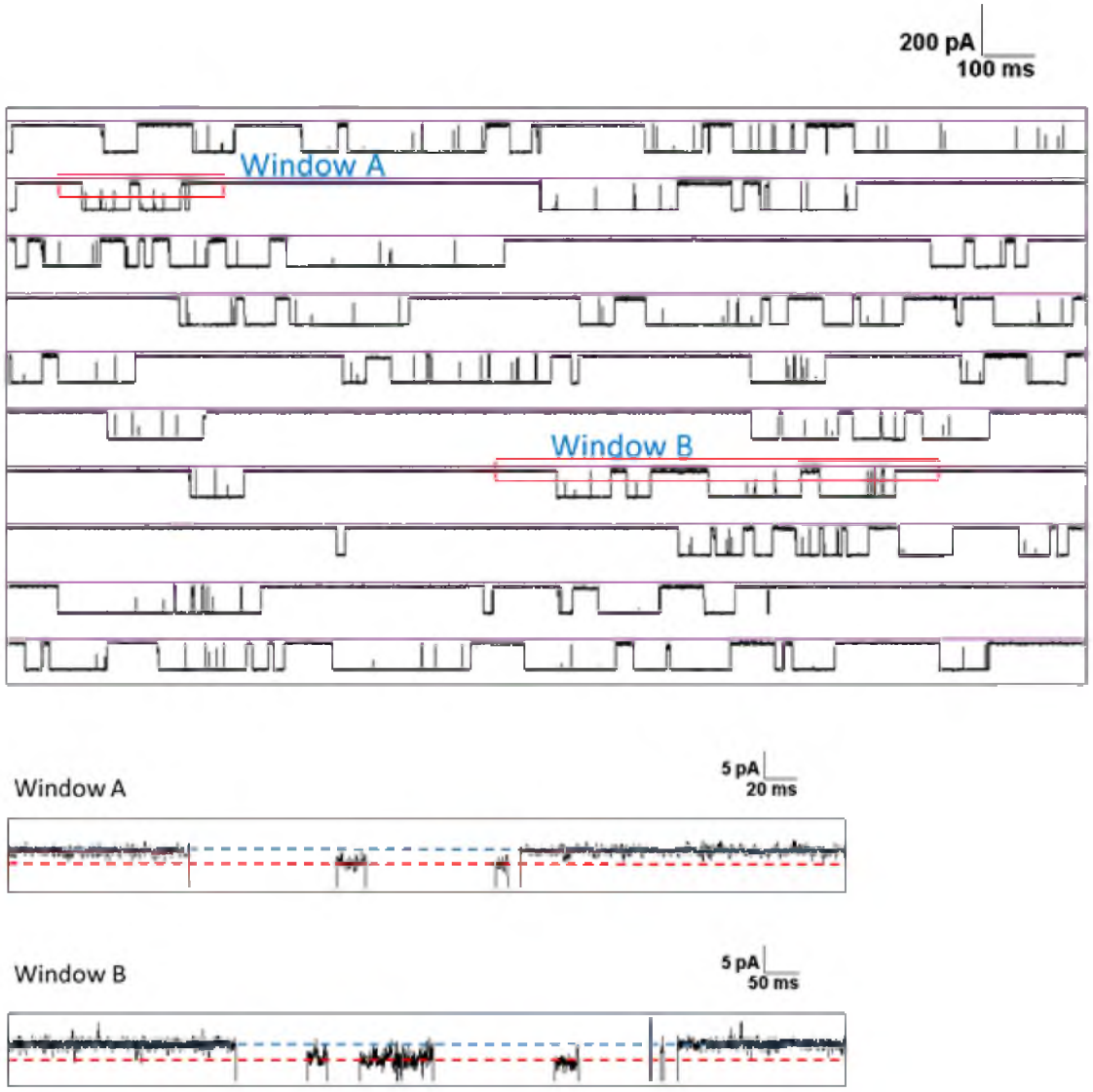

Figure S4.3. A sample *i-t* trace showing uninterrupted data collected at 10 kHz for 20 s at 120 mV. The mixture contained 8 μM A- and B-form duplexes in 1 M KCl, 10 mM PBS, pH 7.4 at 20 °C. The two expanded windows, A and B, show the deep block current differences between A- and B-form duplexes. The expanded area is filtered to 1 kHz for presentation purpose.

S4.6.4 Voltage dependence of unzipping times for DNA-RNA and DNA-DNA duplexes.

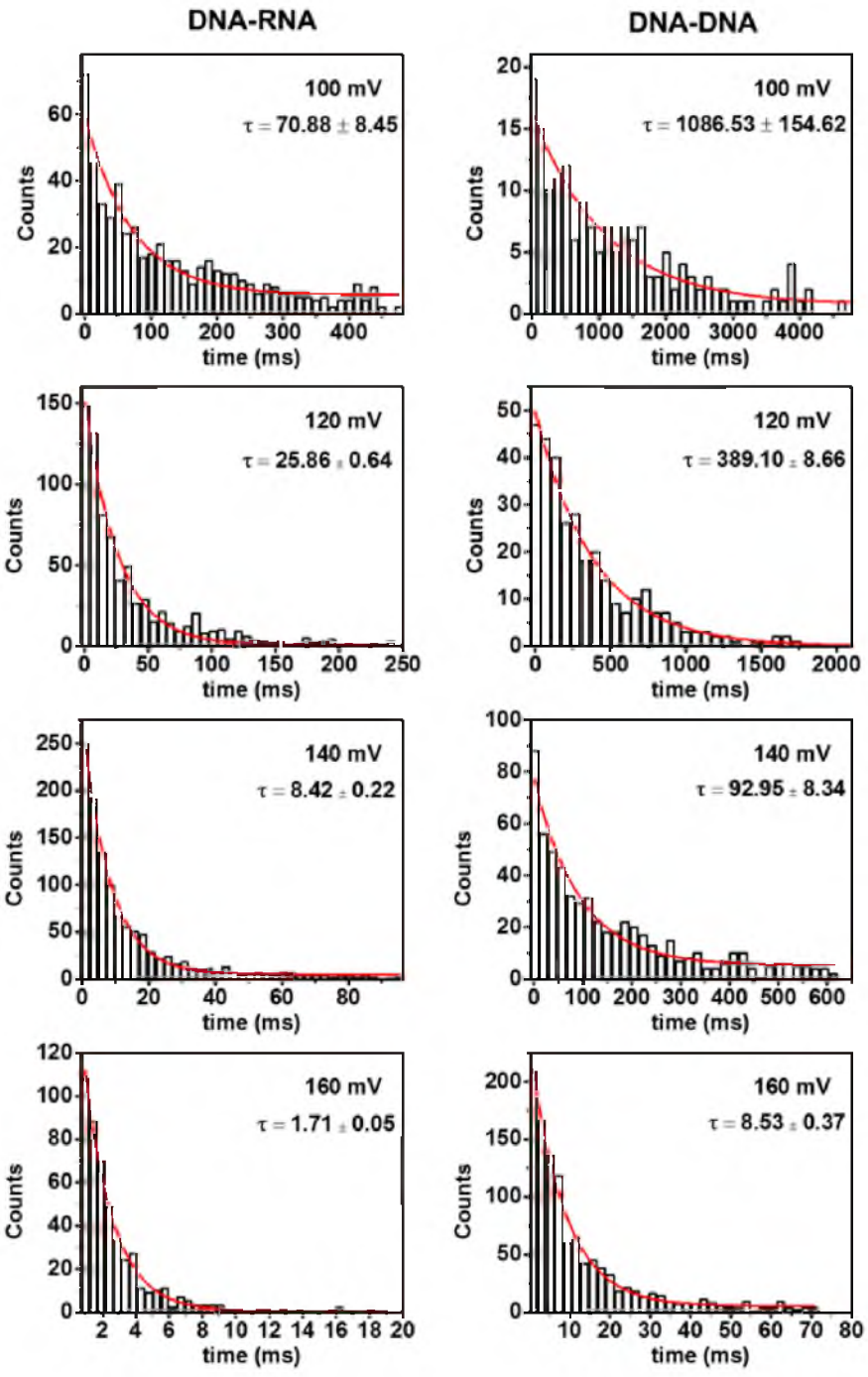

Figure S4.4. Unzipping duration histograms as a function of voltage for DNA-RNA (left) and DNA-DNA (right) duplexes. The data were recorded at 20 °C in 1 M KCl, 10 mM PBS, pH 7.4. An exponential decay was fit to the data to obtain the unzipping time.

S4.6.5 Unzipping of DNA-RNA duplex with 40-nt overhang.

Sequence of DNA-RNA duplex with 40–nt overhang.

DNA-RNA 5`-TCA TCA GTA GAA CTC AGA AAC $TCC_n$-3` n = 40

3`-AGU AGU CAU CUU GAG UCU UUG AG-5`

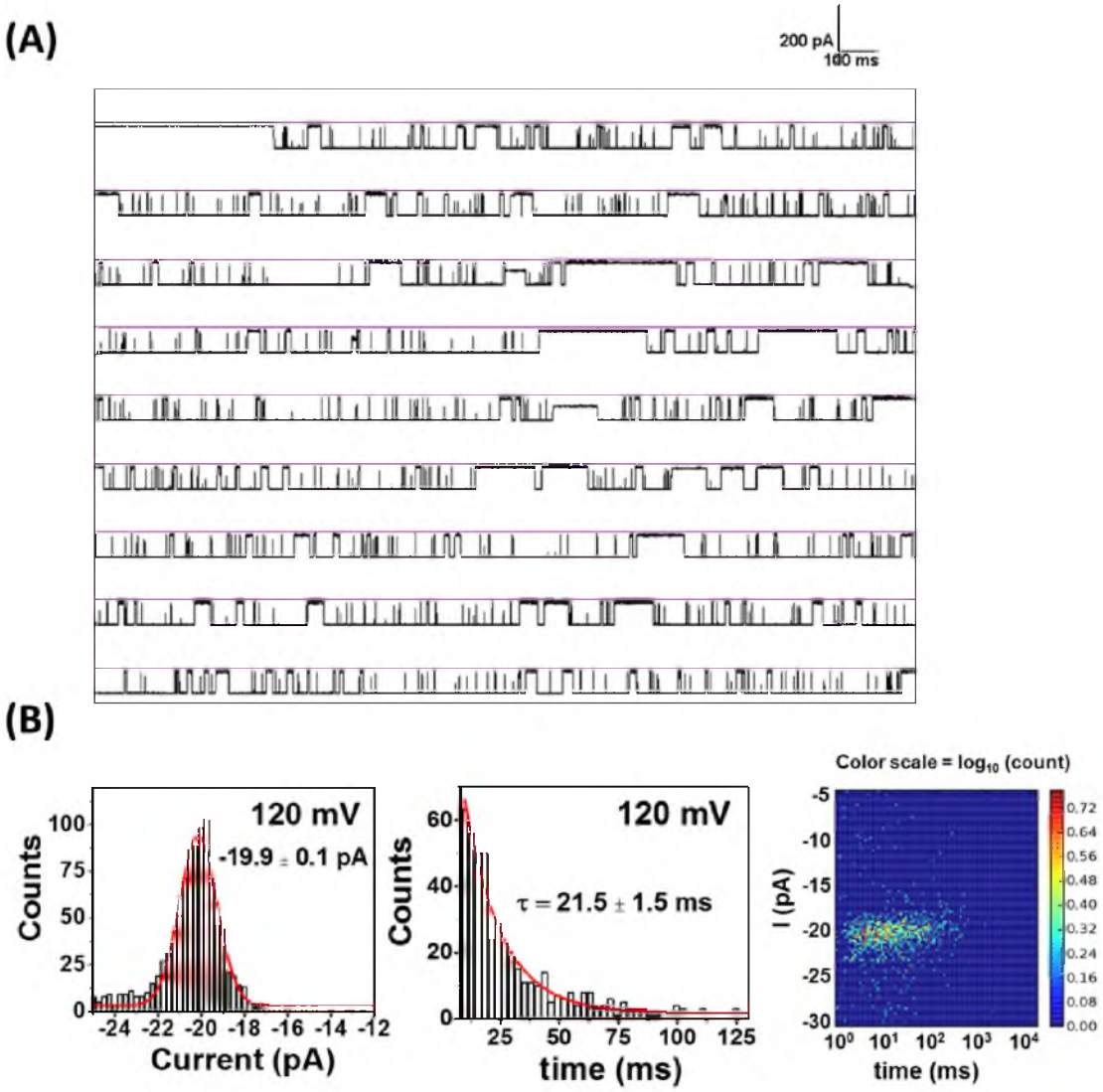

Figure S4.5. (A) A sample *i-t* trace showing uninterrupted data collected at 10 kHz for 20 s at 120 mV. The mixture contained 10 µM DNA-RNA duplex with 40-nt overhang in 1 M KCl, 10 mM PBS, pH 7.4 at 20 °C. (B) Current blockage, unzipping time duration, and *i-t* density plots for DNA-RNA duplex with 40–nt overhang.

S4.6.6 Thermal melting analysis of A-and B-form duplexes.

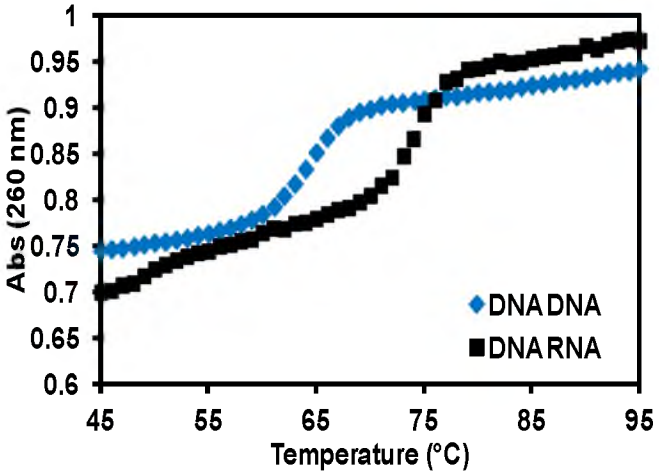

Sequences
DNA-DNA Duplex 5`-TCA TCA GTA GAA CTC AGA AAC TC-3` 3`-AGT AGT CAT CTT GAG TCT TTG AG-5`
DNA-RNA Duplex 5`-TCA TCA GTA GAA CTC AGA AAC TC-3` 3'-AGU AGU CAU CUU GAG UCU UUG AG-5`

Figure S4.6. Thermal melting analysis of the DNA-DNA and DNA-RNA duplexes. All measurements were performed in 10 mM PBS, pH 7.4. The absorbance at 260 nm, $Abs_{260\ nm}$, was monitored as the temperature was increased from 20 °C to 100 °C at a ramp rate of 1 °C/min. At each time interval, the temperature was equilibrated for 30 s prior to making each absorbance measurement. Each experiment was conducted in triplicate.

S4.6.7 Continuous *i-t* trace of DNA-RNA duplex with 10-nt overhang at 160 mV.

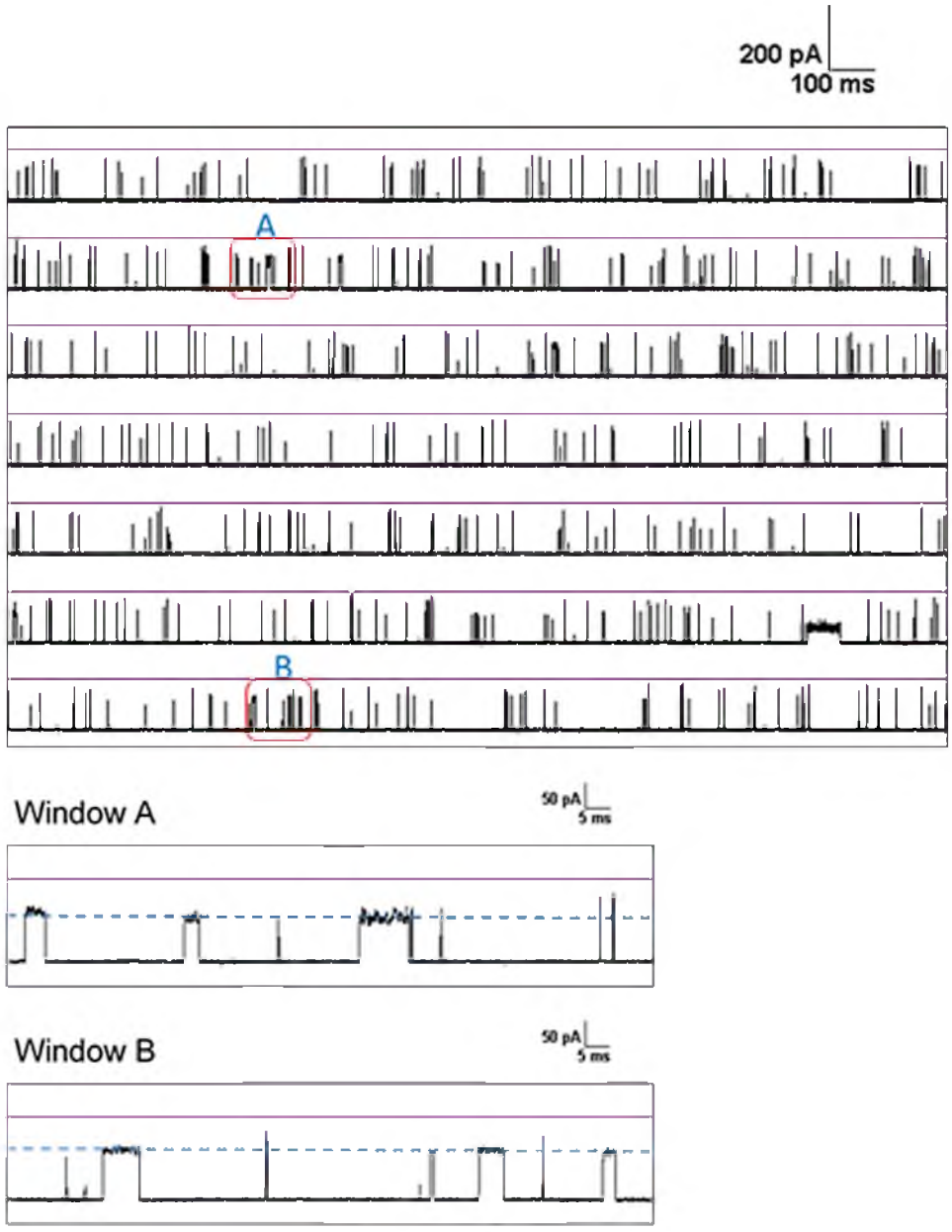

Figure S4.7. A sample *i-t* trace showing uninterrupted data collection at 10 kHz for 20 s at 120 mV. The mixture contained 8 μM of DNA-RNA duplex with 10-nt overhang in 1 M KCl, 10 mM PBS, pH 7.4 at 20 °C. The two expanded windows (A and B) show the blockage due to occupation of the 10-nt overhang in the vestibule.

S4.6.8 Voltage dependent trapping time of the DNA-RNA duplex.
with 10-nt overhang.

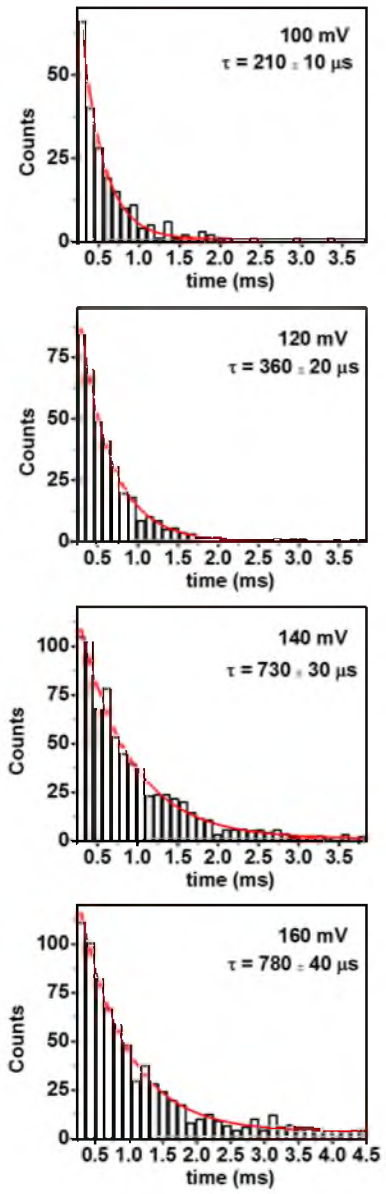

Figure S4.8. Trapping time duration histograms as a function of voltage for DNA-RNA duplex with a 10-nt overhang. Only the events with $\%I/I_o$ between 20 and 80 and $\tau > 200$ μs were analyzed as duplex unzipping events (single strand translocation is much faster). Data were recorded at 20 °C in 1 M KCl, 10 mM PBS, pH 7.4. An exponential decay was fit to the data to obtain the unzipping time.

S4.6.9 Sample *i-t* trace of DNA-DNA duplex with 10-nt overhang at 160 mV.

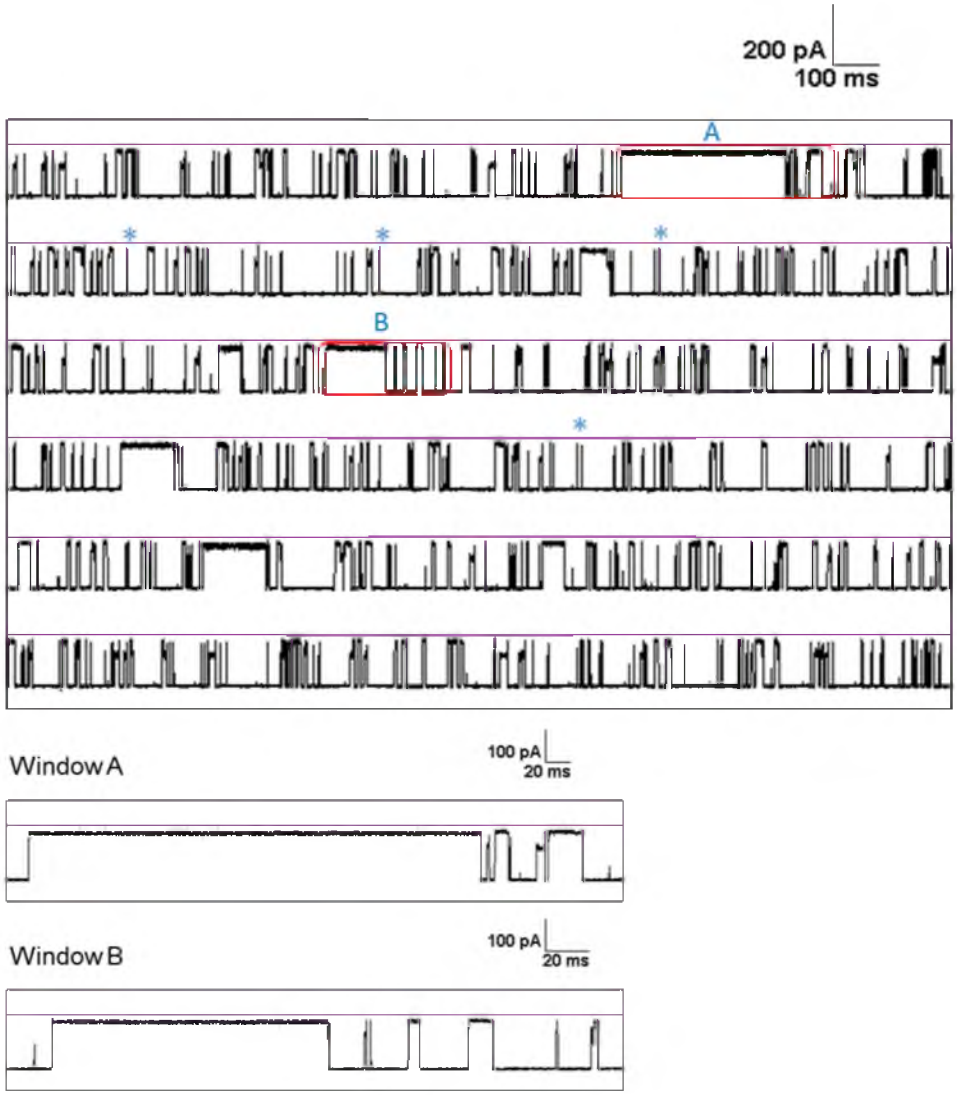

Figure S4.9. A sample *i-t* trace showing uninterrupted data collection at 10 kHz for 20 s at 160 mV. The mixture contained 8 μM of the DNA-DNA duplex with 10-nt overhang in 1 M KCl, 10 mM PBS, pH 7.4 at 20 °C. The two expanded windows (A and B) show long-current blocks are due to unzipping of the duplex and the shorter blocks (less than 1 ms denoted by asterisks) are from translocation of the excess ssDNA.

S4.6.10 Sample *i-t* trace of DNA-RNA duplex with no overhang.

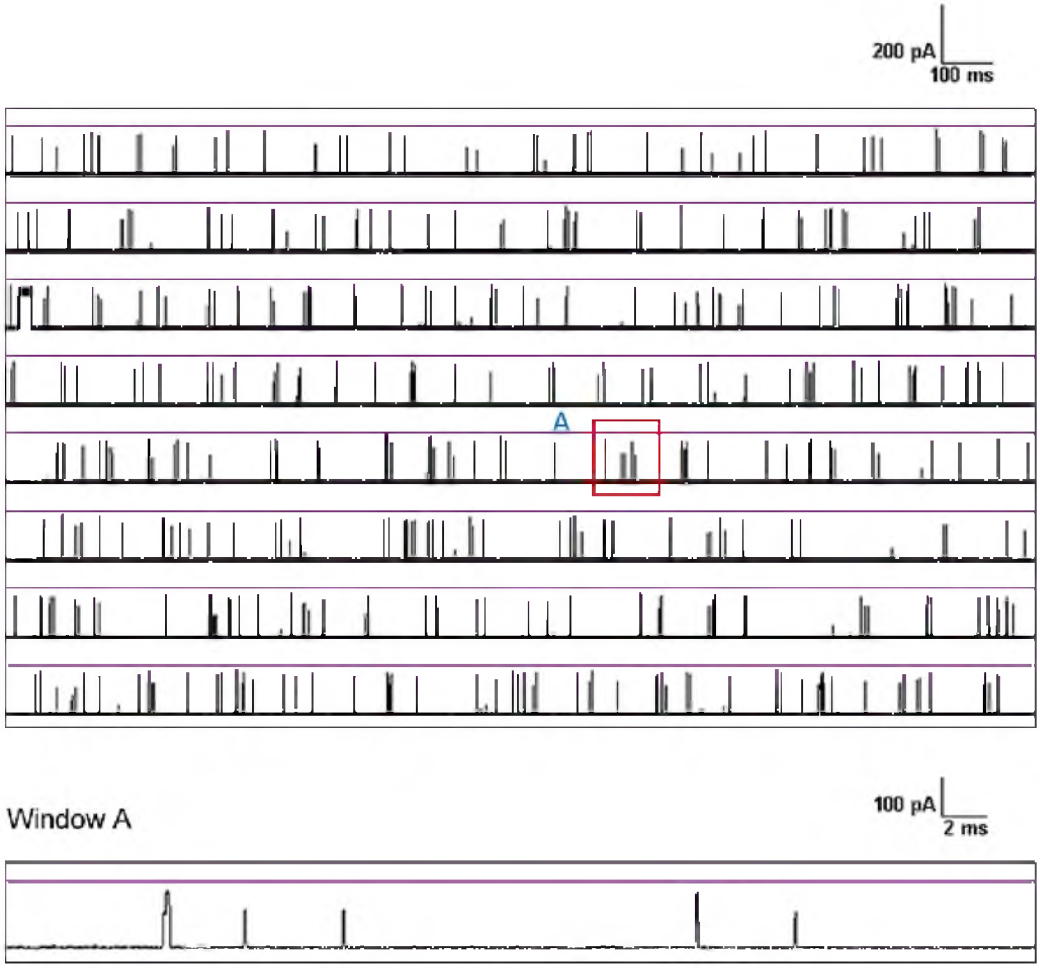

Figure S4.10. A continuous *i-t* trace showing uninterrupted data collection at 10 kHz for 20 s at 160 mV. The mixture contained 8 μM DNA-RNA blunt end duplex in 1 M KCl, 10 mM PBS, pH 7.4 at 20 °C. The expanded window A shows short translocation events (less than 500 μs) that are due to excess single strands present in the mixture.

S4.6.11 Sample *i-t* trace of DNA-DNA duplex with no overhang.

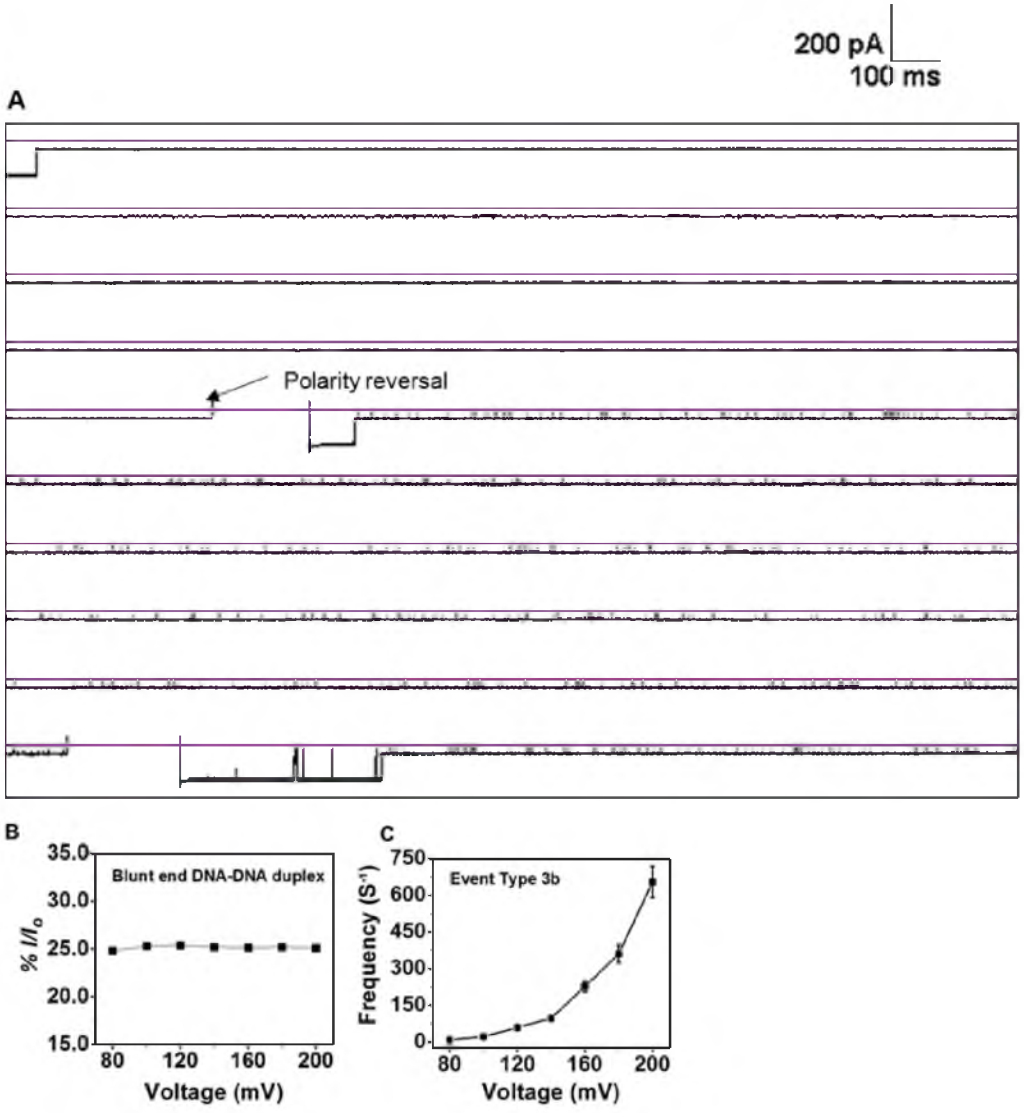

Figure S4.11. (A) A continuous *i-t* trace showing uninterrupted data collection at 10 kHz for 10 s at 120 mV. The *cis* side contained 8 μM DNA-DNA blunt end duplex in 1 M KCl, 10 mM PBS, pH 7.4 at 20 °C. Long-current blockages show the duplex occupying the vestibule and the short events (less than 1 ms) are due to translocation of excess single strands. Interruption of the current blockage was due to the polarity reversal of the channel to remove the duplex in the nanopore. (B) Residual current when a blunt end duplex is inside the vestibule as a function of voltage. (C) Frequency of the events between two current levels shown in Event Type 3b in the main text Figure 4.5B.

S4.6.12 Sample *i-t* trace of DNA-DNA duplex with no overhang at 200 mV.

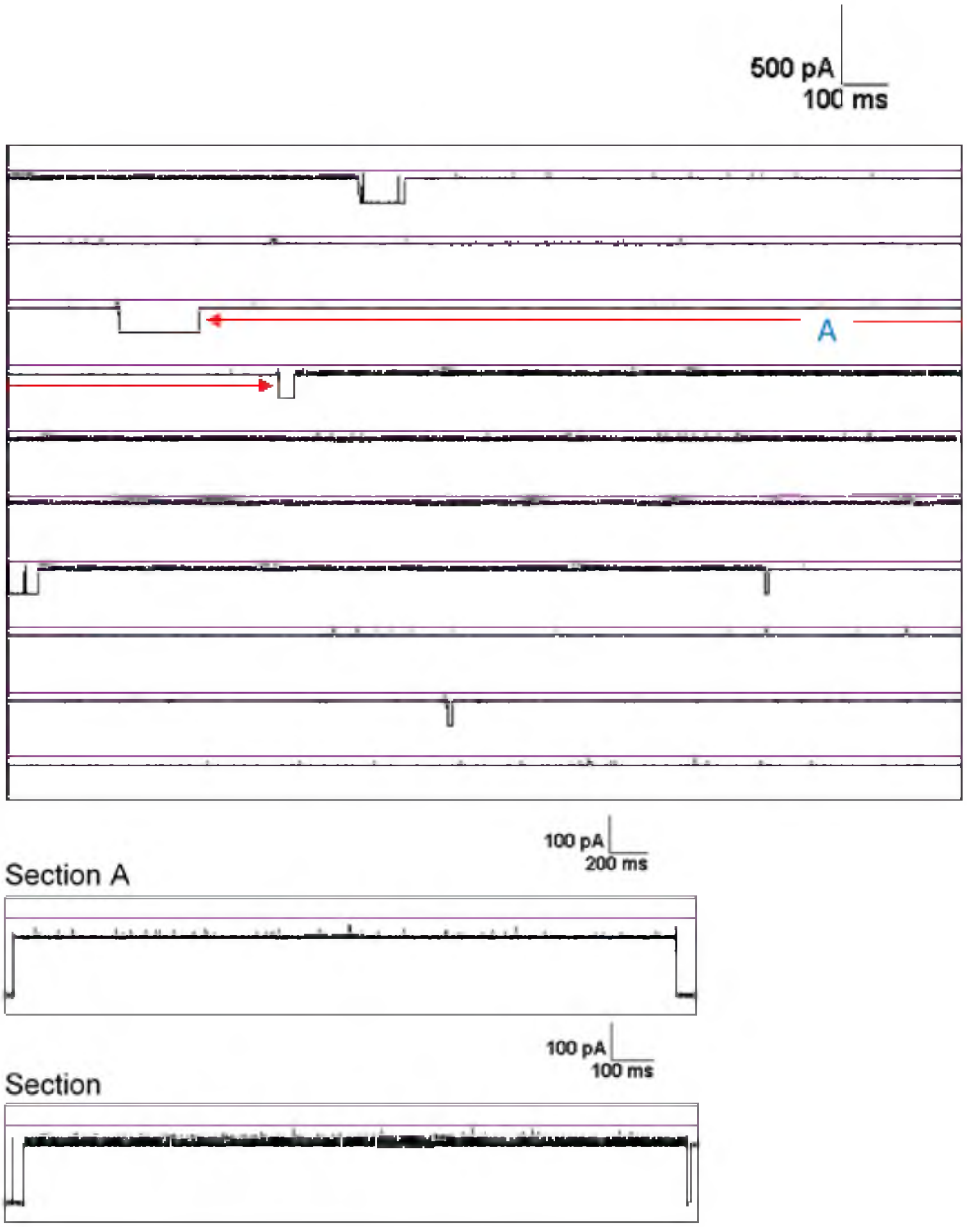

Figure S4.12. A sample *i-t* trace showing uninterrupted data collection at 10 kHz for 20 s at 200 mV. The blunt end duplex unzips at 200 mV but not at 120 mV (see preceding section). The mixture contained 8 μM of the DNA-DNA duplex with 10-nt overhang in 1 M KCl, 10 mM PBS, pH 7.4 at 20 °C. The two expanded sections (A and B) shows long-current blocks are due to unzipping of the duplex.

S4.6.13. Sample *i-t* trace of a mixture containing DNA-PNA duplex.

Sequence of DNA-PNA duplex

DNA-PNA 5`-N GTA GAT CAC T-Lys -3`

3`-CAT CTA GTG $A_{24}$-5`

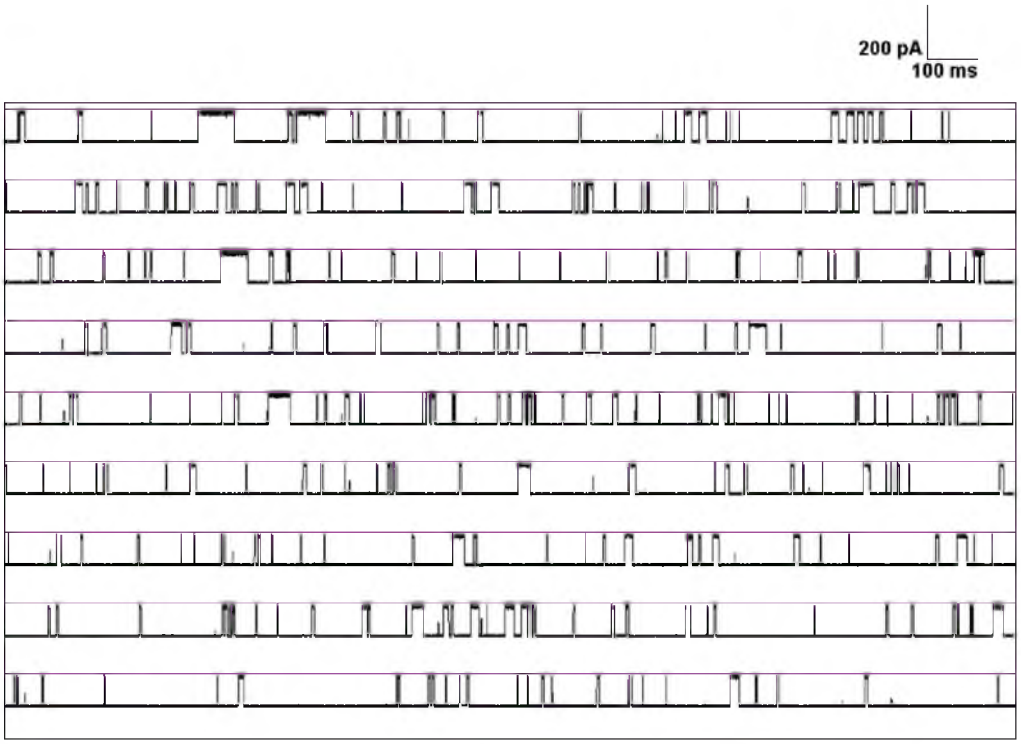

Figure S4.13. A sample *i-t* trace showing uninterrupted data collected at 10 kHz for 20 s at 120 mV. The mixture contained 8 μM DNA-PNA duplex in 1 M KCl, 10 mM PBS, pH 7.4 at 20 °C.

S4.6.14 Unzipping time and voltage dependent unzipping for DNA-PNA duplexes.

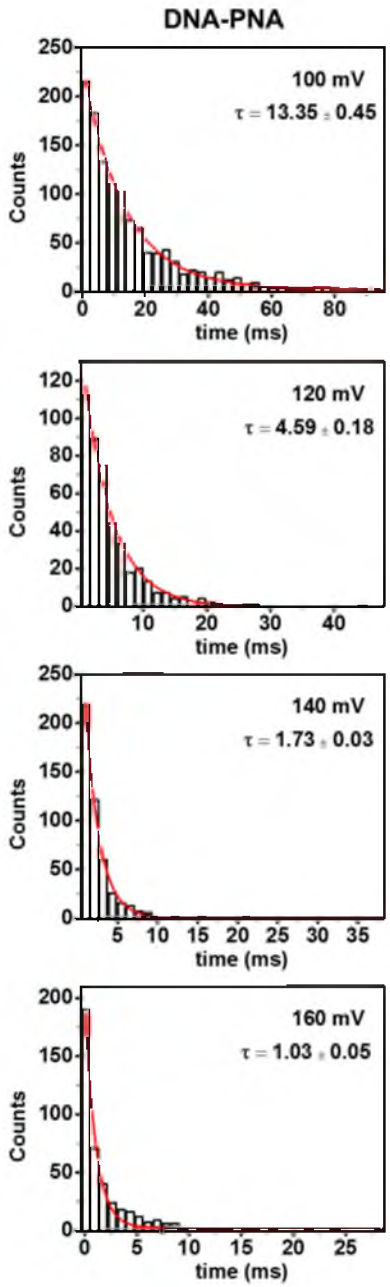

Figure S4.14. Unzipping duration histograms as a function of voltage for the DNA-PNA duplexes. Data were recorded at 20 °C in 1 M KCl, 10 mM PBS, pH 7.4. An exponential decay was fit to the data to obtain the unzipping time. The *cis* side of the protein channel contained 8 μM of DNA-PNA sample.

S4.6.15 Comparison of unzipping times of DNA-RNA duplexes
With 3' and 5' overhangs.

In order to investigate if the orientation of the overhang influences the unzipping mechanism, we performed unzipping experiments using 5'-end poly C (24-nt) to compare with the 3'-end poly C (24-nt) and shown in Figure S4.15. The sequence used is given below.

DNA-RNA 5`-TCA TCA GTA GAA CTC AGA AAC $TCC_n$-3` n = 24

3`-AGU AGU CAU CUU GAG UCU UUG AG-5`

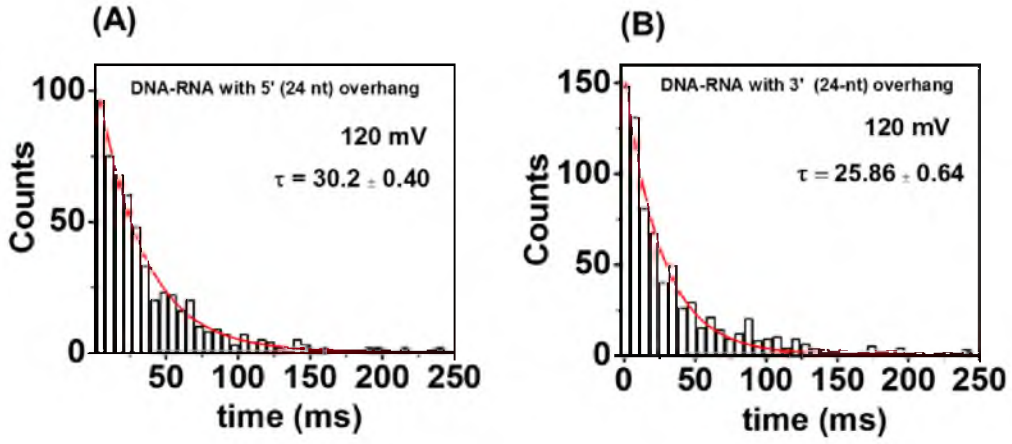

Figure S4.15. Comparison of the unzipping duration histograms for the DNA-RNA duplexes. (A) 5' poly C overhang. (B) 3' poly C overhang. Data were recorded at 20 °C in 1 M KCl, 10 mM PBS, pH 7.4. An exponential decay was fit to the data to obtain the unzipping times. The *cis* side of the protein channel contained 8 μM of DNA-RNA in each case.

CHAPTER 5

CONCLUSIONS

In this dissertation, Chapter 2 describes the use of solid state glass nanopores to study fundamentals of ion transport in a confined geometry. Chapter 3 and 4 describe the use of the biological nanopore, αHL to detect DNA cancer biomarkers and structural differences between different forms of nucleic acid duplexes.

We used the E_A of ion transport as a parameter to study the effect of temperature on ion transport at the nanoscale. The E_A was measured as a function of pore size, electrolyte concentration, and applied voltage as presented in Chapter 2. As indicated by the results, higher temperatures result in a greater entropic relaxation of the ions within the double-layer, altering the potential profile within the pore. The result also suggests that the thermal energy can overcome the electrostatic forces at higher temperatures that could alter the ion transport behavior observed at relatively lower temperatures. The insights gained from the results presented in Chapter 2 are of greater importance to understand the ion transport behavior in confined geometries. Ion transport in nanoscale pores directly determines the performances of porous electrodes, thin film batteries, and supercapacitors. If the devices are operated at higher temperatures during practical applications, the desired outcome could be altered. Moreover, the knowledge of temperature dependence on ion transport will also be useful for the researchers who develop devices that use nanochannels

for nanofluidic electronics,[1,2] electrokinetic energy conversion/storage [3,4] and water purification applications.[5,6]

Chapter 3 has discussed applications of the biological nanopore αHL for the monitoring, quantification, and sequencing of mutagenic compounds. The studies also suggests that the nanopore can be used to detect other lesions, with the additional advantage of providing information on sequence contexts. These results also provide the groundwork for future studies that aim to detect, quantify, and eventually sequence this lesion from cellular DNA sources. However, to extend this method to use in medical applications, the current work should be further improved to test cellular DNA samples. The main challenge to test biomarkers extracted from cells, using nanopore sensors is the lack material concentration for efficient detection. Combining a preconcentration device,[7,8] for an example, microfluidic designs that uses ICP[7,9] with the nanopore sensor device would be a good way to solve these challenges. More work should be focused on integrating nanofluidic devices with nanopore sensors to provide truly single molecular level detection.

Beyond translocation of ssDNA through αHL, dsDNA can be designed to detect lesions based on unzipping experiments. A long ssDNA can be used to probe a short DNA or RNA strand of interest. Utilization of DNA probes to interrogate DNA and RNA has enormous potential for biotechnology applications. In Chapter 4, we have analyzed the unzipping behavior of dsDNA, DNA-RNA, and DNA-PNA duplexes that would allow us to design molecular probes to detect damages and mutations in DNA and RNA. In these studies, we have demonstrated the unzipping of DNA-PNA duplexes for the first time. After carefully analyzing the unzipping behavior of A- and B-forms, we showed A- form

duplexes could not enter the vestibule. We also built a physical model for the interaction of the DNA duplexes with the nanopore, which was tested by changing the length of the ssDNA overhang. This work provides a useful insight on the interaction between dsDNA, DNA-RNA, DNA-PNA molecules, and the αHL nanopore. In particular, it is useful to know that DNA-RNA hybrids do not enter the vestibule of the nanopore, as several probes have been designed to recognize, for example, siRNA in biological samples. These findings, therefore, allow a better design of such probes. Using the insights gained from this study, we can extend our studies to use the advances of site directed mutagenesis to use a protein channels with a wider opening that allows DNA-RNA duplex to sit inside the vestibule. Furthermore, γ HL,[10] which has a wider opening would also be a good choice and further investigation is required to optimize the experiments to detect of damages in RNA a success.

5.1 References

(1) Schoch, R. B.; Han, J.; Renaud, P. *Rev. Mod. Phys.* **2008**, *80*, 839.

(2) Luo, L.; Holden, D. A.; Lan, W.-J.; White, H. S. *ACS Nano* **2012**, *6*, 6507.

(3) Daiguji, H.; Yang, P.; Szeri, A. J.; Majumdar, A. *Nano Lett.* **2004**, *4*, 2315.

(4) Kim, D.-K.; Duan, C.; Chen, Y.-F.; Majumdar, A. *Microfluid. Nanofluid.* **2010**, *9*, 1215.

(5) Kim, S. J.; Ko, S. H.; Kang, K. H.; Han, J. *Nat. Nanotechnol.* **2010**, *5*, 297.

(6) Moghaddam, S.; Pengwang, E.; Jiang, Y. B.; Garcia, A. R.; Burnett, D. J.; Brinker, C. J.; Masel, R. I.; Shannon, M. A. *Nat. Nanotechnol.* **2010**, *5*, 230.

(7) Wang, Y. C.; Stevens, A. L.; Han, J. *Anal. Chem.* **2005**, *77*, 4293.

(8) Khandurina, J.; Jacobson, S. C.; Waters, L. C.; Foote, R. S.; Ramsey, J. M. *Anal. Chem.* **1999**, *71*, 1815.

(9) Kim, S. J.; Song, Y. A.; Han, J. *Chem. Soc. Rev.* **2010**, *39*, 912.

(10) Menestrina, G.; Dalla Serra, M.; Comai, M.; Coraiola, M.; Viero, G.; Werner, S.; Colin, D. A.; Monteil, H.; Prevost, G. *FEBS Lett.* **2003**, *552*, 54.